

2014

Dynamics of non-muscle myosin II organization into contractile networks and fibers at medial cell cortex

Wei Nie
Lehigh University

Follow this and additional works at: <http://preserve.lehigh.edu/etd>



Part of the [Physics Commons](#)

Recommended Citation

Nie, Wei, "Dynamics of non-muscle myosin II organization into contractile networks and fibers at medial cell cortex" (2014). *Theses and Dissertations*. Paper 1573.

This Dissertation is brought to you for free and open access by Lehigh Preserve. It has been accepted for inclusion in Theses and Dissertations by an authorized administrator of Lehigh Preserve. For more information, please contact preserve@lehigh.edu.

**Dynamics of myosin II organization into contractile
networks and fibers at the medial cell cortex**

by

Wei Nie

A Dissertation

Presented to the Graduate and Research Committee

of Lehigh University

in Candidacy for the Degree of

Doctor of Philosophy

in

Department of Physics

Lehigh University

May 19, 2014

© 2014Copyright
Wei Nie

Approved and recommended for acceptance as a dissertation in partial fulfillment of the requirements for the degree of Doctor of Philosophy

Wei Nie

Dynamics of non-muscle myosin II organization into contractile networks and fibers at medial cell cortex

Defense Date

Approved Date

Dissertation Director
Prof. Dimitrios Vavylonis

Prof. Ivan Biaggio

Prof. Daniel Ou-Yang

Prof. Volkmar Dierolf

Prof. Yujie Ding

ACKNOWLEDGMENTS

I would like to express my sincere gratitude to Professor Dimitrios Vavylonis for his guidance and insightful suggestions throughout the course of my Ph.D research. I must remember how much time and effort he has spent in helping me with my research and correcting my posters and paper. I would like to thank Professor Daniel Ou-Yang, Professor Ivan Biaggio, and Professor Sabrina Jedlicka for their expert advices and providing the materials and lab for cell culture, staining, substrate fabrication and microscopy. I would also like to thank Dr. K. Kamijo for providing the cell line.

I would like to thank all current and former members of Professor Vavylonis' group, Laura McMillen, Haosu Tang, Dr. Tyler Drake, Dr. Matthew Smith, Dr. Nikola Ojkic, and Prof. Gillian Ryan for their and help and suggestions. Many thanks for Steven Ming-Tzo Wei for the help in experiments and useful discussions.

I would like to take this opportunity to express my heartfelt appreciation for my parents for their support.

This work is supported by NIH grant 1R01GM098430 and Lehigh University.

TABLE OF CONTENTS

LIST OF FIGURES	VII
LIST OF TABLES	IX
ABSTRACT	1
CHAPTER 1	2
INTRODUCTION	
1.1 Introduction to the cellular cytoskeletal filaments.	2
1.2 Cytoskeleton related proteins and molecular motors	5
1.3 Mechanical properties of cytoskeleton network	8
1.4 Modeling cytoskeletal network	11
1.5 Objective and organization of this dissertation	11
CHAPTER 2	13
NONLINEAR MICROSCOPY ON CYTOSKELETAL NETWORK	
2.1 Introduction to nonlinear microscopy	13
2.2 Second harmonic generation microscopy	16
2.3 Third harmonic generation (THG) microscopy	21
2.4 SHG/THG microscope system setup	22
2.5 Results and discussion	28
2.6 Future work	35
CHAPTER 3	40
MATERIALS AND METHODS	
3.1 HeLa cell culture and treatment	39
3.2 Staining actin filaments and focal adhesions	39
3.3 Microscopy and image process	40
3.4 Preparation of polyacrylamide substrates	41
CHAPTER 4	47
FLUORESCENCE MICROSCOPY OF MEDIAL CORTEX IN	
HELA CELLS AND IMAGE ANALYSIS	
4.1 Introduction	47
4.2 The activity of myosin II is important to the actomyosin network in live HeLa cells	48 48
4.3 Dynamics of medial cortical myosin in adhered HeLa cells.	56

4.4 Spatial-temporal image correlation spectroscopy (STICS) analysis of cortical MRLC-GFP in adhered HeLa cells	58
4.5 STICS analysis of cortical MRLC-GFP in adhered HeLa cells in blebbistatin	61
4.6 Summary and discussion	66
CHAPTER 5	68
MECHANISMS OF MODEL AND SIMULATIONS	
5.1 2D mechanical model: introduction	67
5.2 Model of myosin minifilament turnover and alignment	67
5.3 Simulation results	73
5.4 Discussion and further work	81
CHAPTER 6	83
CONCLUSIONS AND DISCUSSION	
6.1 Summary and conclusions	84
6.2 Discussion and future work	86
REFERENCE	84
CURRICULUM VITAE	98

LIST OF FIGURES

Figure 1.1 Confocal fluorescence images of microtubules, actin filaments, and intermediate filaments in cells.	6
Figure 1.2 Focal adhesions and stress fibers in HeLa cells.	10
Figure 2.1 Diagram of the processes of two-photon excitation microscopy.	15
Figure 2.2 Myosin bipolar filaments and actin thin filaments compose of sarcomeres in muscle tissue.	18
Figure 2.3 Second Harmonic Generation microscopy on muscle tissue.	19
Figure 2.4 Transmission and reflection setup for SHG/THG microscopy.	27
Figure 2.5 Bright field and SHG/THG microscopic image of KNbO_3 crystals.	30
Figure 2.6 Nonlinear microscopic studies of starch granules.	33
Figure 2.7 Absorption coefficient of water for wide range of wavelength.	34
Figure 2.8 Photo damage to HeLa cells by highly focused pulse laser.	37
Figure 2.9 It is necessary to synchronize the pulse laser with the scanning system of the microscope.	38
Figure 3.1 Measurement of focal adhesions from a confocal fluorescence image of a HeLa cell	43
Figure 3.2 Images of HeLa cells expressing MRLC-GFP cultivated on polyacrylamide substrates with Young's modulus of stiffness ranging from 140 Pa TO 60 kPa.	46
Figure 4.1 .Actomyosin fibers and networks in HeLa cells adhered to glass slides.	51
Figure 4.2 .Images of HeLa cells expressing MRLC-GFP (green) stained with vinculin (red) after treatment with blebbistatin.	52
Figure 4.3 The MRLC-GFP intensity of adhered part of cortex in Type I, II and III HeLa cells.	54
Figure 4.4 Images of same cells before and after blebbistatin treatment or before/after blebbistatin washout.	55
Figure 4.5 Time-lapse fluorescence microscopy images of HeLa cells expressing MRLC-GFP reveal a dynamic cortical network.	58
Figure 4.6 STICS analysis of MRLC-GFP dynamics in control cells at a single confocal slice at cell bottom.	61
Figure 4.7 STICS analysis of MRLC-GFP dynamics of cells treated with 100 μM blebbistatin for 60 minutes at a single confocal slice at cell bottom.	64
Figure 4.8 STICS analysis of MRLC-GFP dynamics of cells recovering from blebbistatin at a single confocal slice at cell bottom.	65
Figure 4.9 Comparison of analysis of cell images of control, blebbistatin-treated cells, and cells recovering from blebbistatin in regions of 100 by 100 pixels as in Fig. 4.6, 4.7 and 4.8.	66
Figure 5.1 Cartoon of coarse-grained model of myosin minifilament interaction.	71
Figure 5.2 Simulation of Type I cells with ICS analysis of the simulation results.	75

Figure 5.3 Simulation of Type II cells with ICS analysis of the simulation results.	76
Figure 5.4 Simulation of Type III cells with ICS analysis of the simulation results.	77
Figure 5.5 2D simulation of actomyosin network in Type II and Type III cells.	80

LIST OF TABLES

Table 2.1 An estimation of the power of SHG excited by different lasers.	25
Table 3.1 Preparation of 1ml Polyarylamide Gel Solutions for Given Elastic Modulus.	45
Table 5.1 Parameter values used in simulations.	71
Table 4.2 Comparison of simulation results.	79

ABSTRACT

The cellular morphology of adhered cells depends crucially on the formation of a contractile meshwork of parallel and cross-linked stress fibers along the contacting surface. The motor activity and mini-filament assembly of non-muscle myosin II is an important component of cell-level cytoskeletal remodeling during mechanosensing. To monitor the dynamics of non-muscle myosin II, we used confocal microscopy to image cultured HeLa cells that stably express myosin regulatory light chain tagged with GFP (MRLC-GFP). MRLC-GFP was monitored in time-lapse movies at steady state and during the response of cells to varying concentrations of blebbistatin (which disrupts actomyosin stress fibers). Using image correlation spectroscopy analysis, we quantified the kinetics of disassembly and reassembly of actomyosin networks and compared to studies by other groups. This analysis suggested the following processes: myosin minifilament assembly and disassembly; aligning and contraction; myosin filament stabilization upon increasing contractile tension. Numerical simulations that include those processes capture some of the main features observed in the experiments. This study provides a framework to help interpret how different cortical myosin remodeling kinetics may contribute to different cell shape and rigidity depending on substrate stiffness. We discuss methods to monitor myosin reorganization using non-linear imaging methods.

Chapter 1

Introduction

1.1 Introduction to the cellular cytoskeletal filaments.

The cytoskeleton is very important to cells by regulating cell migration, proliferation, maintaining biochemical and mechanical stability, and transporting biochemical materials within cells. There are three types of filaments in the cytoskeleton: actin filaments, microtubules and intermediate filaments [1].

Actin filaments are polymer filaments assembled by actin monomers [2]. The actin filament has two strands that rotate around each other to form a helical structure. In each strand, each actin monomer binds with two other monomers on either side. The monomers bind ATP or ADP. The actin filament end with the ATP/ADP binding site exposed is referred as the pointed end, while the opposite end is referred as the barbed end. In cells, actin filaments are very dynamic, with the barbed ends growing by actin monomer addition while the older parts of the filament sever and depolymerize. This actin filament polymerization and depolymerization process is coupled with ATP hydrolysis, which includes the following steps: unpolymerized actin monomers (G-actin) binding with ATP; G-actin with bound ATP polymerization to form actin filaments (F-actin); F-actin hydrolyzing ATP to ADP+P_i and releasing P_i; F-actin with bound ADP depolymerization to G-actin with bound ADP; G-actin releasing ADP and binding ATP [2, 3]. The actin subunits with bound ADP dissociate from the pointed end slowly but ADP-actin disassembly is catalyzed by actin binding proteins (e.g. cofilin [4]).

Actin filaments are involved in contractile processes in muscle and non-muscle cells. In muscle cells, actin filaments, which are also called thin filaments, together with myosin II bipolar thick filaments, crosslinkers (e.g. α -actinin) and actin decorating proteins (e.g. tropomyosin), form a permanent sarcomeric structure. Contraction occurs when myosin thick filaments pull towards the barbed ends of actin filaments [1]. In non-muscle cells, actin filaments and myosin form more disorganized and dynamic contractile networks related to the cell migration [5, 6], the assembly of contractile ring in eukaryotic cells [7, 8], and maintaining the cellular morphological stability. The importance of myosin activity to the formation of

contractile cytoskeletal networks is the focus of this dissertation. This will be investigated in details in Chapter 4 and 5.

There are numerous proteins that control the dynamics of actin filaments to realize a variety of functions in vivo. For example, N-WASP helps actin filaments polymerize by promoting actin filament nucleation through the activation of the Arp2/3 complex [9, 10]. Actin capping proteins [11, 12], bind to the growing end (barbed end) of the actin filament and prevent the actin from polymerizing. Also, actin filaments can be disassembled by severing proteins, such as gelsolin and cofilin [13-16]. Opposite to the severing proteins, there are crosslinker proteins, such as α -actinin and FilaminA [17, 18], which help actin filaments to form bundles and networks with different architectures [19, 20].

Microtubules, found in all eukaryotic cells, are tube shaped filaments assembled by tubulin dimers with a diameter of 25 nm [1, 21]. The microtubule has 13 protofilaments that bind to each other laterally to form a single tube. Each protofilament is composed by α and β tubulin dimers connected end to end where α -subunit of tubulin dimer connects to β -subunit of tubulin dimer. Therefore in a protofilament, if one end is exposed as α -subunit, the other end is exposed as β -subunit. In a microtubule, all the protofilaments bind to each other with the same polarity, so the microtubule has an α -subunit end and a β -subunit end, which is called plus (+) and minus (-) end, respectively. When a microtubule elongates in cells, new tubulin dimers are mostly polymerized at the (+) end. The assembly and disassembly rate of microtubule varies under different conditions. The microtubule polymerizes when the GTP-tubulin caps the (+) end of microtubule. This GTP- β -tubulin quickly undergoes hydrolysis into GDP- β -tubulin, which is unstable and will fall off the microtubule end. The switch of microtubule from growth to rapid depolymerization is called catastrophe [22, 23]. The catastrophe is stopped when GTP-tubulin binds on the (+) end of the microtubule, which starts to grow again, a process referred to as rescue [24, 25]. The processes of microtubule growth, catastrophe, and rescue depend on temperature, pH, and the concentrations of tubulin and GTP, and Mg^{2+} . Although these processes are observed in vitro without the involvement of other proteins, the dynamics of microtubules in vivo is regulated by microtubule associated proteins (MAPs). MAPs play an important role in the formation of microtubule networks, the function of microtubules in neurons, cargo transportation along microtubules, and cell division [26, 27]. Several drugs have been discovered to be able to bind with tubulin and interfere with the dynamics of microtubule assembly/disassembly. For example, taxol [28]

stabilizes the GDP- β -tubulin at the tip of microtubules and stops their depolymerization, thus inhibiting cell mitosis and division. Nocodazole is another drug that prevents microtubule from polymerization. Cells treated with nocodazole can enter mitosis, however, because the microtubules do not polymerize, they cannot anchor on the kinetochores to initiate cell division, thus cells are arrested in metaphase [29]. The above evidence demonstrates that the dynamics of microtubules is crucial to the growth and proliferation of cells.

The third major component of cytoskeletal network is intermediate filaments (IF) [1]. The name “intermediate filaments” was given because their diameter is about 10 nm, which is between the diameter of actin filaments (~7 nm) and microtubules (~25 nm). There are five major types of intermediate filaments based on the protein that forms the IF, which are (i) keratin filaments in epithelial cells; (ii) vimentin filaments in the interstitial cells (iii) desmin filaments in muscle cells; (iv) neurofilaments in neurons; and (v) neuroglial filaments in nerve cells. The intermediate filaments in a cell appear in different forms. Some intermediate filaments interconnect to each other to form a network. Some intermediate filaments form thick bundles, and some others are dispersed in the cytoskeleton. Intermediate filaments form a scaffold in the cytoplasm to determine the location of cell nucleus and maintain the mechanical stability of the cytoskeletal network [30, 31]. They are also found to be important in embryo development and epidermal cells differentiation [32]. Some diseases have been found to be related to abnormalities of neurofilaments, particularly amyotrophic lateral sclerosis (ALS) has been discovered to be the result of the accumulation and abnormal assembly of neurofilaments [33]. Intermediate filaments, in crosstalk with actin filaments and microtubules, are crucial to cell function, such as regulating the structural organization and dynamics of the cytoskeletal network, and controlling the cell cycle and signal transduction.

The properties of cell cytoskeletal filaments are important in the research of biomaterials on the microscopic scale (ten to a few hundreds of microns in length). The study of cytoskeletal network assembly can inform methods for the synthesis of polymeric organic materials, the design of new pathways for drug delivery in organs, and understanding the function and physiology of cellular behavior.

1.2 Introduction to molecular motors

Another important component of the cytoskeleton is molecular motors [1]. Molecular motors act as crosslinkers in the cytoskeletal network, but also have more tasks, such as walking along filaments to transport cargos, or generating and maintaining the tension around the cytoskeleton. Different molecular motors bind and walk on different filaments in different directions, for example, kinesins move in the (+) direction along microtubules, and dyneins move in the (-) direction [34]. Molecular motors work together with passive crosslinkers to affect the assembly and properties of cytoskeletal networks. Networks containing molecular motors and passive cross-linkers can form a connected structure under tension; these stable networks are capable to deal with external forces and a varying mechanical environment. Depending on how molecular motors and passive cross-linkers bind to filaments, they can connect them in parallel or antiparallel orientations to form bundles (such as filopodial actin filaments cross-linked by fascin) or along multiple directions to form loose networks (such as actin networks cross-linked by α -actinin).

In this thesis we will discuss myosin molecular motors that can bind and pull on actin filaments. Myosin motors have a long tail that can be (1) attached with vesicles in the cytoplasm to deliver cargos to different regions in the cytoskeletal network in the cell; (2) tangled with other myosin to form a bigger complex and act collectively in cells. Myosin II can form minifilaments that assemble in stress fibers or myofibril fibers in muscle (see Fig. 2.2A). When myosin heads on the opposite side of the minifilament bind with different actin filaments, they can slide the actin filaments toward each other and produce contraction in the network [1, 35].

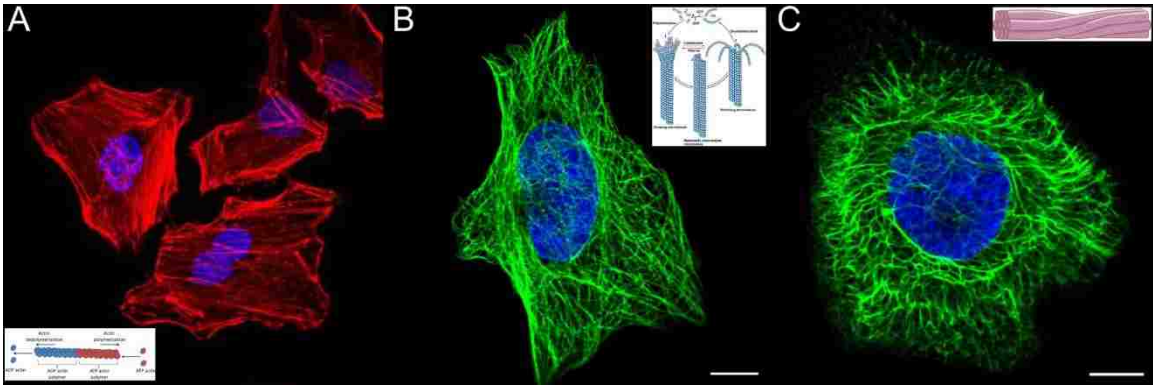


Figure 1.1. Confocal fluorescence images of microtubules, actin filaments, and intermediate filaments in cells. (A) Actin filaments with rhodamine phalloidin (red) in HeLa cells. Insert cartoon shows the actin filament polymerization and depolymerization (modified from [36]). (B) Immunofluorescence staining image of microtubules in U2OS cell [37]. Insert cartoon shows the polymerization/depolymerization, catastrophe and rescue process of a microtubule [38]. (C) Immunofluorescent staining of intermediate filaments have a twisted, rope-like structure that supports the cell structural stability, which are partly located close to the nucleus, but may stretch throughout the cell [37]. Insert cartoon shows the intermediate filament is a strand of many polymer filaments [39]. Scale bar=10 μ m.

1.3 Focal adhesions and the cell cortex

Another important subcellular structure, which is referred as focal adhesions (FA), is important to the cortical fibers and network formation and organization [40]. FA is a macromolecular assembly that links the cytoskeletal network to the extracellular matrix (ECM) and serves for mechanosensing and biochemical signal transduction for the cell that regulates the dynamics of cytoskeletal network. The major components of focal adhesions include integrin-linked kinase (ILK), focal adhesion kinase (FAK), talin, vinculin, α -actinin, and paxillin. Vinculin is an important focal adhesion protein that links the integrin to the actin filaments of the cytoskeleton. Vinculin stained by fluorescent antibody is often used in microscopy to visualize the focal adhesions of cells (see Materials and methods in Chapter 3, and Fig.1.2). Focal adhesion assembly and disassembly is important to cell migration. In the leading edge and lamellar regions of a migrating cell, small focal adhesions (referred to as focal complexes) are continuously assembled and disassembled. Some focal complexes stabilize and mature eventually and become the anchors of the cell and pull the cell forwards. In the trailing edge, focal adhesions are disassembled by various mechanisms [41-43]. In non-migrating cells that adhere to the extracellular matrix (ECM), the focal adhesions act as mechanosensors that inform the cells of the ECM conditions, and help the cytoskeleton maintain the mechanical stability.

When cells adhere to substrates through focal adhesions, they also form cortical networks underneath the cell plasma membrane, which is mainly composed by actomyosin filaments, crosslinkers and membrane binding proteins. 3D fluorescence images of HeLa cells expressing MRLC-GFP show that actomyosin fibers are assembled and anchored in the cortical network over the membrane that adherent to the coverglass (see Fig. 1.2F and [44]). The cortical actomyosin network acts as a scaffold to maintain the shape and stability of cell membrane. The dynamics of the cortical network are closely related to the cell migration, division. Time lapse fluorescence imaging of cortical network shows that the medial cortical network in HeLa cells is very dynamic. As we will see in Chapter 4, we observed directed motion of myosin foci and foci turnover. Medial fibers form through this process of myosin foci assembly and disassembly, which will be investigated by image analysis and simulations in Chapters 4 and 5.

1.4 Mechanical properties of cytoskeleton network

In this section we will provide a brief overview of experimental techniques used to measure the mechanical properties of cytoskeletal networks in cells. Cell mechanical properties are directly determined by the cytoskeleton, where not only the mechanics of the filaments themselves, but also the filament binding proteins and interaction between them play important roles. A number of techniques, such as microrheology [45, 46] and atomic force microscopy (AFM)[47], traction force microscopy (TFM), have been applied to study the mechanical properties of the cytoskeleton.

In microrheology, polystyrene beads with diameter about $1\mu\text{m}$ are imbedded in cells for imaging. There are two types of microrheology: passive and active microrheology. In passive microrheology, the motion of the beads is driven thermally; in active microrheology, the motion of beads is driven by external forces, such as optical tweezers and magnetic field. By analyzing the trajectory of the beads over time, one can find the elastic and viscous properties of the cytoskeleton network or cytoplasm from the mean-square displacement of the particle motion using the generalized Stokes–Einstein relation. In a medium without the activity of molecular motors, the passive and active microrheology show similar viscoelasticity of the network at low strains. However, in a network with active myosin II, active microrheology experimental data show that network under high strain has non-linear viscoelastic behavior [48, 49]. This microrheology method, combined with high resolution confocal fluorescence microscopy, has become a widely used tool in studying the cytoskeletal network and molecular motor dynamics.

AFM is often used to measure the mechanical properties of cells by pressing a cell with a cantilever, the Young's modulus of the cell can be derived from the deflection of the cantilever [50, 51]. Microrheology and AFM are usually used to measure the local mechanical properties in cells. The micropipette aspiration method [52] can be used to access the global mechanical properties of cells. In the practice of micropipette aspiration, part of a cell or the whole cell is pulled into a micropipette with a diameter generally smaller than the cell [52]. One can obtain the mechanical properties of the cell cortex by comparing the applied suction pressure in the micropipette to the distance of the cell protrusion inside the micropipette.

Another widely used method to obtain mechanical information is cellular traction force microscopy (TFM). The mechanism of cell-ECM and cell-cell interaction is very complicated to be measured directly. However, these interactions are very important in organizing the cytoskeletal network, cell migration, wound healing and embryonic morphogenesis [53, 54]. The traction force microscopy uses elastic substrates, such as polyacrylamide (PAA) (see Chapter 3, materials and methods) or polydimethylsiloxane (PDMS) gel coated with ligands that cells can attach on (e.g. fibronectin or collagen) and imbedded with micro-sized fluorescence beads. When cells attach and spread on the substrates, or migrate on the substrates, the fluorescent beads undergo a displacement because of the traction force that cells exert on the substrates. With the information of Young's modulus and shear modulus of the gel, and the position and displacements of the beads, one can extract the global and local information of cell-ECM interaction, such as magnitude and direction with time resolution. In recent years, more advanced computational algorithm and experimental methods, such as Fourier-transform traction cytometry, and traction reconstruction with point forces, were developed to achieve a spatial resolution of traction force as high as $\sim 1\mu\text{m}$ [55].

Many other techniques, such as protein separation and purification methods, protein structure measurement methods X-ray crystallography and NMR spectroscopy [56], fluorescence resonance energy transfer (FRET) [57], electron microscopy (EM) [58] and super resolution microscopy [59] have been developed to push the study of the cytoskeleton to individual molecular/protein level. Particularly, the discovery of green fluorescence protein (GFP) opened a door for new methods to study the dynamics and function of cytoskeletal networks in live cells. In Chapter 3 and 4, we will present the application of confocal fluorescence microscopy in study the dynamics of actomyosin network *in vivo*, and the analysis of confocal fluorescence images.

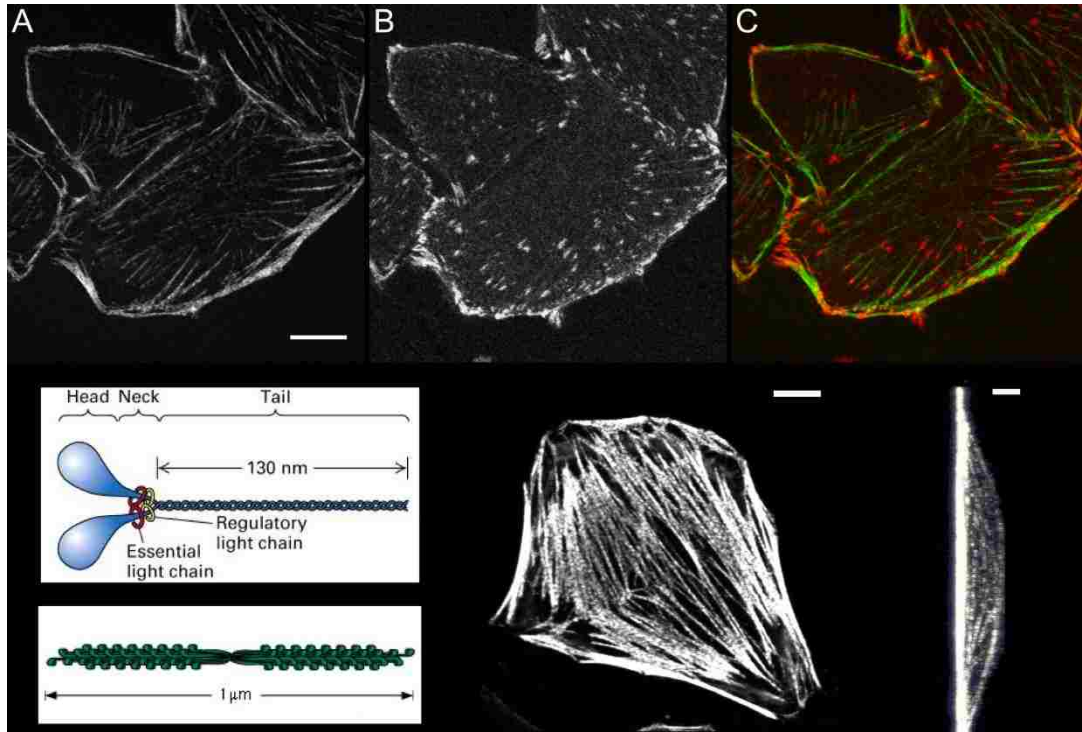


Figure 1.2 Focal adhesions and stress fibers in HeLa cells. (A-C) Confocal images of HeLa cells expressing MRLC-GFP (A), focal adhesions stained by vinculin antibody (B), and merged (A) and (B) into (C), respectively, where red indicates focal adhesions and green indicates myosin II in (C). (D) Structure of a myosin II molecule is composed of two heads, two regulatory light chains (RLC), two essential light chains (ELC), and a coiled-coil tail. A myosin bipolar minifilament contains 10-20 myosin II molecules on each side, with the length of $\sim 1 \mu\text{m}$ [35]. (E) The MRLC-GFP image of a HeLa cell with stress fibers in the middle. (F) Side view of (E) Shows that the cortical actomyosin fibers anchored in the cortical network over the membrane that adherent to the coverglass. Scale bar: $10 \mu\text{m}$.

1.5 Modeling cytoskeletal networks

A number of mathematical and computational models have been developed to describe cytoskeletal filament growth and network assembly for both in vivo and in vitro experiments [60-62]. Many methods and techniques have been used, such as ordinary/partial differential equations (ODE/PDE) and Monte-Carlo simulation. Some models address the dynamical process of stress fiber assembly [63, 64] and polarity structural feature of stress fibers [65]. Some models describe the reorganization of stress fibers in mechanosensing through interaction between focal adhesions and substrates [60, 66]. Some models study the mechanical properties of cytoskeletal networks regulated by crosslinkers and molecular motors [67-69]. Simulations based on coarse grained models have shown that molecular motors, working with crosslinker proteins, drive the filaments to form different patterns, such as bundles, stars, waves and networks [47, 70-73]. These models help us further understand the mechanisms of cytoskeleton reorganization and the formation of cellular functional structures such as stress fibers [63], contractile rings [74], and mitotic spindles [75, 76].

In this thesis, we proposed a simple 2D mechanical model to understand the dynamical properties of medial stress fiber assembly. The model and simulation results will be discussed in Chapter 4.

1.6 Motivation and organization of this dissertation

As discussed above, the assembly of actomyosin fibers and networks at the cell cortex is closely related to the activity of myosin II, molecular motors that crosslink the actin filaments and generate contraction throughout the actomyosin networks. Contractile actomyosin networks have been reconstructed by purified actin and myosin in vitro, which helps to understand the formation of actomyosin networks [20, 77-79]. However, the actomyosin networks in cells are more complicated than in vitro systems. There are still many open questions concerning the mechanisms of medial fiber and network assembly by molecular motors and proteins in vivo [77, 80].

This work focuses on the dynamical features of cortical actomyosin networks in live cells. Chapter 2 introduces nonlinear microscopy and SHG/THG microscopic system applied on biomaterials, which might be useful in future studies of the structural and dynamical feature of fibers and actomyosin networks

under tension as they undergo reorganization in cells. Chapter 3 describes the materials and protocol of preparing culture medium for HeLa cells, fixing and staining the actin filaments and focal adhesions, and making polyacrylamide substrates. We also introduce the methods of quantifying the MRLC-GFP and focal adhesions in fixed HeLa cells. In Chapter 4, we present the experiments that demonstrate how the activity of myosin II in cells determines the actomyosin network assembly and STICS analysis of the time-lapse MRLC-GFP images at the cortex adherent to the coverglass. In Chapter 5, we use 2D mechanical model and Monte-Carlo simulations to capture the dynamical feature of medial cortical fiber assembly and disassembly. Chapter 6 is the conclusion and discussion of this thesis.

Chapter 2

Nonlinear microscopy on cytoskeletal network

2.1 Introduction to nonlinear microscopy

Nonlinear microscopy, including second/third harmonic generation (SHG/THG) microscopy, coherent anti-Stokes Raman scattering (CARS) microscopy, and two-photon excitation microscopy (TPEM), has become an important imaging modality in optics and biology. TPEM is a method using two photons from high intensity infrared laser to excite one molecule of fluorophore. TPEM has the advantage of less photobleaching and higher probing depth into the biological tissue [81-83]. However, it still requires staining the target molecules with fluorophores or tagging the cells with fluorescent genes. SHG is generated due the non-centrosymmetric structure of the organic materials, such as stress fibers and microtubules, and THG is generated because of the inhomogeneity of the biological tissue (index of refraction), such as the cellular membrane and nucleus. Therefore, SHG/THG microscopy does not require staining the cells with fluorophores, and it requires a similar system setup as the TPEM [82-85], although some modification to the TPEM system is necessary to efficiently acquire the SHG/THG photons in the SHG/THG microscopy. Comparing with confocal fluorescence microscopy, SHG/THG microscopy has the following advantages: (1) SHG microscopy has deeper probe ability into the bio-tissue; (2) It does not require exogenous staining (e.g., green fluorescent proteins (GFP)), so there will not be photobleaching happening during the imaging process, and (3) SHG/THG microscopy shares similar optical setup as TPEM, so it is convenient to couple these two non-linear microscopy techniques to study the biological system. During the SHG/THG process, two photons with same frequency are converted into one and emitted out of the sample. So, there is zero photonic energy transferred into the cells, and the damage to the biological sample is minimized. However, in practice, we found that the sample could be damaged by the heat due to the absorption of infrared laser if the sample was overexposed under the highly focused laser. We will discuss the photon damage to the live cells further in section 2.6.

SHG/THG microscopy has been applied in biomedicine to help diagnosing defects in tissues due to illness, gene defect or aging [86-88]. For example, the SHG/THG images of collagen tissue show the weakness and

defects due to the arthritis [89-91]. SHG image of human cornea shows the status of cataract [92-96]. And SHG images of rat cardiac muscle reveal the abnormal development of heart due to the gene defect [97-99]. In recent years, SHG/THG has been used to study the development of embryo cells by generating SHG signal from the spindles and microtubules and THG signal from cell membranes [100-103]. At present, the challenge to the SHG/THG microscopy is to obtain SHG/THG images of live cells in real time. According to the calculation and the fact that thick filaments in muscle tissue produce detectable SHG signal, it is possible to acquire SHG images of stress fibers or a contractile ring in vivo. In the following sections, we will firstly introduce the theory of SHG/THG microscopy (section 2.2) and its system setup (section 2.3), then we will use our home-made microscope system to obtain SHG/THG images of potassium niobate (KNbO_3) microcrystals and starch granules (section 2.4). In the last section (section 2.5), we will discuss the limitation of our microscope system that has to be modified to meet the requirement to obtain the SHG/THG image in live cells.

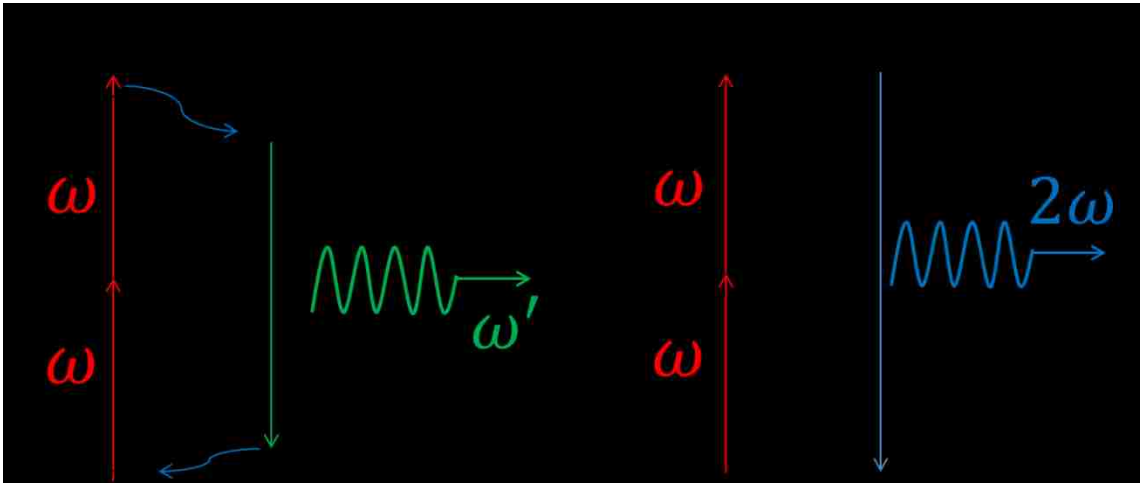


Figure 2.1 Diagram of the processes of two-photon excitation microscopy. (A) and SHG microscopy (B). For the process of two-photon excitation microscopy, a fluorophore absorbed two infrared photons simultaneously and emitted one photon with shorter wavelength as fluorescence. For SHG process, the dipole in the medium interacted with the incident laser and turned two input photons into one with double frequency and the emitted double frequency photon was acquired through the confocal microscopic system.

2.2 Second harmonic generation microscopy

SHG is generated from the interaction between atoms in noncentrosymmetric structures and electric field in the optical medium. It was first demonstrated by P.A. Franken etc., in 1961 that the frequency of an intense pulse laser with the wavelength of 694nm could be doubled crystalline quartz [104, 105]. In 1962, the SHG process was described by N. Bloembergen and P. S. Pershan based on Maxwell equations for electromagnetic field propagating in the medium with nonlinear electric susceptibility [106].

Let's assume the electric field of incident laser is $\vec{E} = E_i \hat{i} + E_j \hat{j} + E_k \hat{k}$. If the medium has a nonlinear electric susceptibility, the electric polarization in the medium is:

$$P_k = \varepsilon_0 \left(\chi_{ik}^{(1)} E_i + \chi_{ijk}^{(2)} E_i E_j + \chi_{ijkl}^{(3)} E_i E_j E_l + \dots \right) \quad (2.1)$$

If we consider the second order term and calculate the nonlinear polarization $P_k(NL) = \chi_{ijk}^{(2)} E_i E_j$, the electric field of the incident laser can be written as:

$$E_i = \frac{1}{2} \varepsilon_i \exp(-i\omega t) + c.c. \quad (2.2)$$

Where ω is the frequency so $E_i = \text{Re}[\varepsilon_i e^{-i\omega t}]$. The average power of the incident wave is:

$I_0^{(\omega)} = \frac{1}{2} \varepsilon_i^2$. The nonlinear term of the polarization is:

$$P_k(NL) = \frac{1}{4} \chi_{ijk}^{(2)} \left(\varepsilon_i \varepsilon_j \exp(-i2\omega t) + \varepsilon_i^* \varepsilon_j^* \exp(i2\omega t) + \varepsilon_i \varepsilon_j^* + \varepsilon_i^* \varepsilon_j \right) \quad (2.3)$$

The first two terms in the nonlinear polarization (Eq.2.3) show that the polarized dipoles in the medium radiate the electric field with double frequency of the incident laser. In most of the optical materials, the second order susceptibility $\chi^{(2)}$ is zero at macroscopic scale because of their centrosymmetric crystalline structures.

However, there are also many nonlinear optical crystals such as potassium niobate (KNbO₃) that are noncentrosymmetric structures. For a biological object, such as stress fibers, it is convenient to neglect the

interactions between molecules to obtain the macroscopic susceptibility $\chi^{(2)}$ by assuming that each molecule (protein) assembled into the stress fiber has a non-zero molecular hyperpolarizability β_{zzz} . We use an ‘‘Oriented gas model’’ [107] for a 2D crystal assembled by one dimensional molecule with molecular hyperpolarizability β_{zzz} to illustrate how to calculate the components of tensor $\chi^{(2)}$ in the bulk.

$$\chi_{ijk}^{(2)} = N f_i^{2\omega} f_j^\omega f_k^\omega \cos \theta_{iz} \cos \theta_{jz} \cos \theta_{kz} \beta_{zzz} \quad (2.4)$$

where N is the number density of molecules (myosin II S1 heads that binding on the actin thin filaments) with molecular hyperpolarizability β_{zzz} , f_i^ω ($f_i^{2\omega}$) is a local field correction factor. f_i^ω is often calculated through the Lorentz model $f_i^\omega = \frac{(n^\omega)^2 + 2}{3}$. θ_{iz} is the angle between the direction of molecular polarization (x, y, z) and the dielectric axis (i, j, k).

From Eq. (2.2) and (2.3), the intensity of SHG signal generated by a biological sample is:

$$I^{(2\omega)} \propto (\chi^{(2)})^2 (I_0^{(\omega)})^2 \quad (2.5)$$

$I^{(2\omega)}$ is determined by the second order susceptibility $\chi_{ijk}^{(2)}$ so that the intensity of $I^{(2\omega)}$ relative to the polarization of input laser reveals microstructure of the optical media. We will use two examples, myosin thick filament and myofibrils, to show how the techniques of SHG microscopy have been applied to study the microstructure of the biological tissues during recent years.

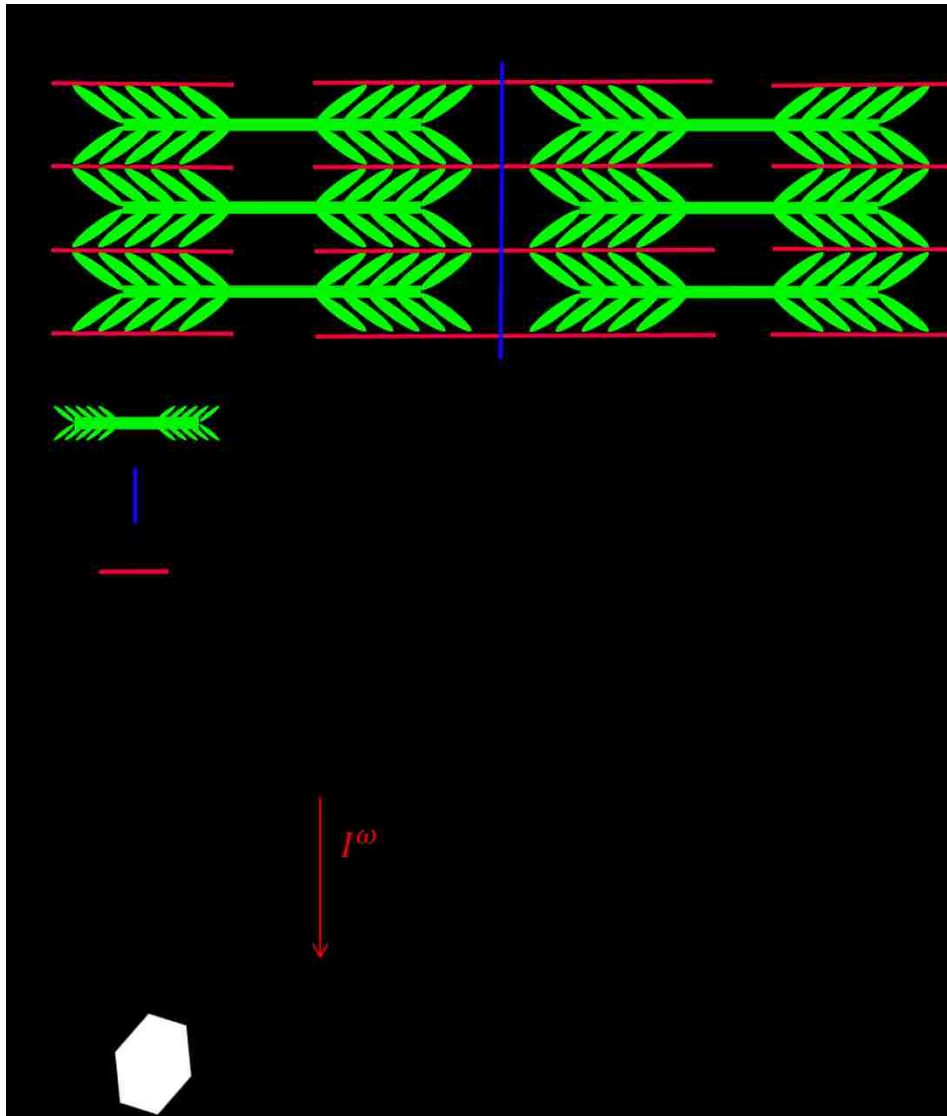


Figure 2.2 Myosin bipolar filaments and actin thin filaments compose of sarcomeres in muscle tissue, an example of noncentrosymmetric assembly of one dimensional molecules with molecular hyperpolarizability β_{zzz} , (A) and the hexagonal model of myofibril filament that has nonzero components of macroscopic second order susceptibility tensor $\chi^{(2)}$ (B).

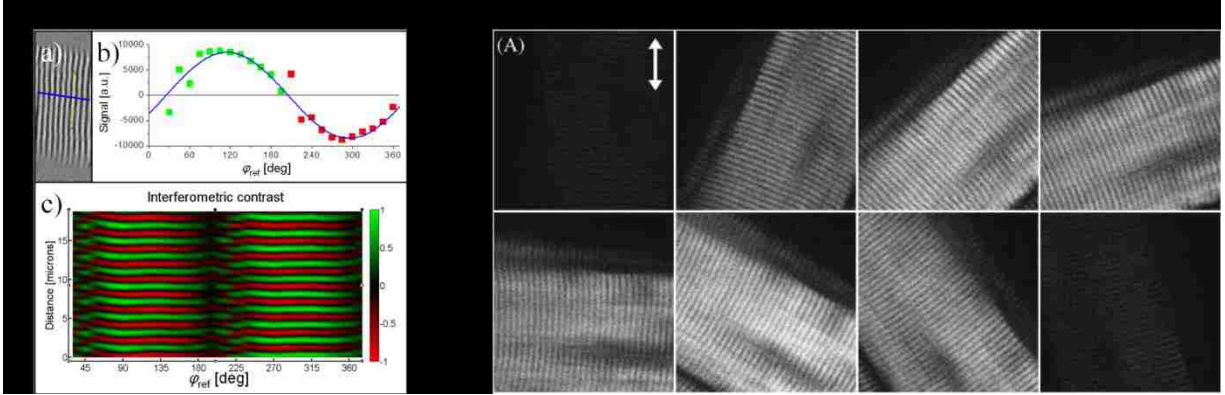


Figure 2.3 (A) Interferometric Second Harmonic Generation (ISHG) microscopy on muscle tissue demonstrates that myosin II molecules assemble into bipolar filaments and form sarcomere structure in muscle tissue [108]. (B) SHG intensity of myofibrils changes as a function of angle α between the fundamental polarization and myosin/actin

filaments. $\frac{\chi_{333}^{(2)}}{\chi_{113}^{(2)}}$ and $\frac{\chi_{311}^{(2)}}{\chi_{113}^{(2)}}$ for myofibril can be determined by fitting the intensity to function in Eq. 2.6 [109].

The first example, as shown in figure 2.2A, is a sarcomere structure in muscle tissue. The components of its second order susceptibility $\chi_{111}^{(2)}$, $\chi_{133}^{(2)}$, $\chi_{331}^{(2)}$, and $\chi_{313}^{(2)}$ are vanished because the assembly of molecules is symmetric in the \hat{x} direction ($x = 1$) so that the sum of the second order polarization was cancelled through the cosines components. The only non-zero components of $\chi^{(2)}$ are $\chi_{311}^{(2)}$, $\chi_{113}^{(2)}$, $\chi_{131}^{(2)}$, and $\chi_{333}^{(2)}$. Although as far as we know, the components of $\chi^{(2)}$ have not been determined experimentally, this bipolar filament model for myosin thick filament in muscle tissue was confirmed by Interferometric Second Harmonic Generation (ISHG) microscopy [108] by determining that the phase difference between the SHG from two opposite sides of the myosin filaments is π (see figure 2.3A).

The second example of biological materials with nonzero $\chi^{(2)}$ is myofibril, which is made of densely packed actin and myosin filaments. Myofibril is often modelled as a bundle of tube with a hexagonal symmetry on the cross section plane with its cylindrical symmetric axis along \hat{z} direction (figure 2.2B). The only nonvanishing components of $\chi^{(2)}$ are $\chi_{311}^{(2)}$, $\chi_{333}^{(2)}$, and $\chi_{113}^{(2)}$. The second harmonic generation could be written as [109-114]:

$$P_{SHG}^{(2\omega)} = \chi_{113}^{(2)} \sin(2\alpha) E^2 \bar{x} + [\chi_{333}^{(2)} \cos^2 \alpha + \chi_{311}^{(2)} \sin^2 \alpha] E^2 \bar{z} \quad (2.6)$$

where the intensity of SHG depends on α (figure 2.2B), which is the angle between the incident light's polarization and the z-axis. With the SHG microscope system configured as figure 2.4 shows, the intensity of SHG emitted by the myofibril would be:

$$I_{SHG}^{(2\omega)} \propto \left\{ \left(\chi_{113}^{(2)} \sin(2\alpha) \right)^2 + \left[\chi_{333}^{(2)} \cos^2 \alpha + \chi_{311}^{(2)} \sin^2 \alpha \right]^2 \right\} E^4 \quad (2.7)$$

By fitting the intensity of $I_{SHG}^{(2\omega)}$ vs. α , which is the angle between the polarization of input laser and the

symmetry \hat{z} axis of myofibril, one can obtain the ratio of $\frac{\chi_{333}^{(2)}}{\chi_{113}^{(2)}}$ and $\frac{\chi_{311}^{(2)}}{\chi_{113}^{(2)}}$. According to the Kleinman's

symmetry, $\frac{\chi_{311}^{(2)}}{\chi_{113}^{(2)}}$ should equal to 1. The experimental data of $\frac{\chi_{333}^{(2)}}{\chi_{113}^{(2)}} \approx 0.09$ and $\frac{\chi_{311}^{(2)}}{\chi_{113}^{(2)}} \approx 1.15$

demonstrated that (i) $\chi_{333}^{(2)}$ is small, which means that the myofibril is largely symmetry along its symmetric

axis. (ii) the non-vanishing $\chi_{311}^{(2)}$ and $\chi_{113}^{(2)}$ indicate the chirality of the filaments along \hat{z} axis, and this

chirality might cause the $\hat{z} \rightarrow -\hat{z}$ asymmetry if the myofibril is symmetric along \hat{z} axis. (iii) $\frac{\chi_{311}^{(2)}}{\chi_{113}^{(2)}}$

deviates from 1 might be caused by resonance because the SHG frequency in experiment was not far from the resonant frequency of muscle (see figure 2.3B for SHG images of myofibrils) [109].

From these two examples we can see that SHG microscopy provides a novel method to image a biological system without staining it with fluorescence dye. Furthermore, SHG signal reveals the information of the microscopic structure of the proteins (molecules) of interest in the biological system. It

is also capable of deeper probing into the tissue and less out of focal plane photo damage to the sample comparing with conventional confocal microscopy. Therefore, it's of interest to apply this technique to study the process of stress fiber assembly and contractile ring during cytokinesis of cells with high spatiotemporal resolution.

2.3 Third harmonic generation (THG) microscopy

The application of SHG microscopy has been limited to a few biological objects because most biological samples do not exhibit SHG. In contrast, third harmonic generation occurs in all materials so that it is widely used as a microscopy method with resolution comparable to standard confocal fluorescence microscopy. From Eq. (2.2), the third order of the electric polarization is:

$$P_k^{(3)} = \chi_{ijk}^{(3)} E_i E_j E_l = \frac{1}{8} \epsilon_0 \chi_{ijk}^{(3)} (\epsilon_i^3 e^{-i3\omega t} + 3\epsilon_i \epsilon_i^* e^{-i\omega t} + c.c.) \quad (2.8)$$

The intensity of THG is expressed as:

$$I^{(3\omega)} \propto (\chi^{(3)})^2 (I_0^{(\omega)})^3 \quad (2.9)$$

Unlike the two-photon or three-photon excitation fluorescence microscopy, the intensity of THG is not only determined by the number density of molecules in the sample, but also determined by the third order susceptibility and enhanced by the effect of interfaces of different materials in the sample. THG is very sensitive to the local inhomogeneity of the optical susceptibility and molecular density in the sample at the scale of micrometer that comparable to the focused beam. THG signal from a sample is strong when the

condition of phase-matching is satisfied. In the homogeneous medium in biological tissue, THG before and after the focal point is destructive to each other by interference [115-117], so THG image of a biological tissue reflects the inhomogeneity of the medium or the interface of two medium in a sample. For example, THG image of cells indicates the nuclear and cellular membrane and cell-cell junctions [102]. Comparing with the DIC or phase-contrast microscopy, THG signal is determined by the third order susceptibility of medium rather than its index of refraction, so it is more suitable to be used to take image of transparent samples [116].

2.4 SHG/THG microscope system setup

It requires a few modifications to the confocal fluorescence microscope system in Physics Laser Spectroscopy Lab, (Department of Physics, Lehigh University) to be able to take SHG/THG images of a biological sample.

Figure 2.4 shows the diagrams of our SHG/THG microscopy system. The system has the following work modes:

- (1) Transmission setup by using CCD (EMCCD) camera to acquire SHG/THG images.
- (2) Transmission setup by using Olympus FV1000 scanning system to obtain SHG/THG images.
- (3) Reflection setup by import laser from the IR port of Olympus IX81 microscope and obtain SHG/THG images through Olympus FV1000 scanning system.

Compared to the reported SHG/THG imaging system, our system has the following features: (see Table 2.1). Firstly, we have Ti-Sa pulse laser and pulse laser as the excitation laser source. The former is the typical laser source that people use to obtain SHG/THG imaging, the latter has very low repetition rate (1 kHz), which not only provides very high peak intensity that favors the SHG and THG, but also reduced the possibility of photodamage to live cells [118].

Equation (2.7) shows that the intensity of the second harmonic generation is proportional to the square of the incident laser's intensity, and the intensity of the third harmonic generation is proportional to the cube of the incident laser's intensity. The average power illuminated on the cells are 5 mW with transmission set-up (see Fig 2.4A), and 5 mW for Ti-Sa laser with reflection set-up (see Fig 2.4B). The Ti-Sa laser was

conducted into the IR port of FV1000 system (see fig2.4B), but the microscope system has not yet been modified for IR laser and a large portion of power was lost when it goes through the dichroic mirrors (fig 2.4B).

The average output power of our pulse laser was about 45mW. With low repetition rate (1kHz) and the pulse width is 1 ps, the peak laser power would be as high as 4.5×10^7 W, which makes it possible to produce strong SHG signal through transmission setup (see fig2.4A) if the laser was highly focused on the material that has non-zero second order susceptibility. The laser was focused on the sample with beam waist as $0.65 \mu\text{m}$ by microscope lens. So the peak intensity of focused laser is 3.4×10^7 W/ μm^2 . It is necessary to compare the average power of SHG signal in different microscopic systems.

The average power of SHG produced in our system could be 4 orders larger than the SHG generated by Ti:Sapphire laser commonly used in SHG microscopy [119-122] according to the calculation. This is an estimation of SHG power obtained from biological tissues. From Eq. (2.5), the power of SHG can be expressed as:

$$P_{2\omega} = A(\chi^{(2)})^2 P_{\omega}^2 \quad (2.10)$$

where A is a constant determined by the sample and microscopic system, and P_{ω} is the power of incident laser. From the comparison in Table 2.1, we can see that when the average power of Ti:Sapphire laser with high repetition rate (80 MHz) is the same as the pulse laser with low repetition rate (1 kHz) in our lab, the peak intensity of our pulse laser is 10^4 times larger than the Ti:Sapphire laser. Because of the nonlinear relation between input laser power and the output laser power (see Eq. 2.5 and 2.10), the peak power of SHG produced by our laser is 10^8 times larger than by Ti:Sapphire laser. Although the longer pulse length and lower repetition rate of our laser leads to a factor of 10^4 loss of average power of SHG compared to the Ti:Sapphire laser, the average power of SHG signal generate from our system is still 1.2×10^4 times larger than the system using Ti:Sapphire laser (see table 2.1).

However, we found that there must be a threshold value for the peak intensity of input laser, which is much smaller than the peak intensity produced by the pulse laser, to avoid photodamage. Figure 2.8 shows that highly focused laser beam destroyed the cells in one second (IR absorption and photodamage to biomaterials will be discussed in the next section). Therefore we have to use the input laser with the

peaking intensity lower than $3.4 \times 10^7 \text{ W}/\mu\text{m}^2$. We didn't measure the threshold peak intensity of laser that damages the cells, but we measured the power of input laser that damages the cells to be $\sim 5 \text{ mW}$ before focused by microscope objective. Even if the input power of our laser is reduced to 1 mW , the average power of SHG signal is calculated to be $4.1 \times 10^{-7} \text{ W}$, which is still larger than the power of SHG produced by Ti:Sapphire laser shown in table 2.1. We will then take samples of KNbO_3 (Potassium Niobate) crystals, starch granules, fixed and live cells for nonlinear microscopy in our system.

Table 2.1. An estimation of the power of SHG excited by different lasers.

Excitation lasers	Ti-Sa laser [†]	Pulse laser (Lab)
Average power	45 mW (880nm)	45mW (1200nm)
Pulse duration	150 fs	1 ps
Repetition rate	80 MHz	1 kHz
Peak power (W)	3.75×10^3	4.5×10^7
Beam diameter(μm)	1.3	1.3
Peak intensity ($\text{W}/\mu\text{m}^2$)	2.8×10^3	3.4×10^7
Avg. Power of SHG (W)	$A(\chi^{(2)})^2 P_\omega^2$ *	$A(\chi^{(2)})^2 P_\omega^2 \times (1.2 \times 10^4)$

[†] V.Nucciotti, et al. PNAS, Vol 107, 7763-7768 (2010).

* P_ω is the peak power of Ti-Sapphire laser. A is an constant determined by sample
(see Eq. (2.10))

In the transmission setup type (1) (figure 2.4A), pulse laser was conduct into the upper side port, reflected by silver mirror and focused on the sample through a 10x (or 100x) condenser. We took SHG/THG images of Potassium Niobate (KNbO_3) crystal powder to test our transmission setup (1), because it is the material that has large nonlinear coefficients for wavelength conversions. To avoid the synchronizing issue we discussed in section 2.3, we used CCD camera as the detecting instrument. The images of bright view, the second harmonic generation and the third harmonic generation are shown in figure 2.5. The SHG/THG images of KNbO_3 show that our pulse laser with wavelength of 1200nm-1500nm is strong enough to generate bright SHG/THG images from nonlinear optical crystals. In fact, the intensity of laser projected on the KNbO_3 crystal is so strong that we could defocus the laser beam to make the illumination area larger than $10 \times 10 \mu\text{m}^2$. Also, because the SHG/THG signals were strong, the image acquiring time could be as short as 200 ms per frame. These images demonstrate that our system is technically viable, and it is promising to use this system to obtain SHG/THG image of live cells.

More efficient way to achieve SHG/THG imaging is to import IR pulse laser from the IR port of the IX 81 confocal microscope, and synchronize the scanning/detecting system with the input laser. This scheme is illustrated in figure 2.4B. In this type (3) setup, one could make use of the scanning system built in the microscope to take both SHG/THG images and TPEF images of the cells. In order to do so, we have to make a few modifications to the microscope system. One issue is that the dichroic mirror in the FV1000 system (see figure 2.4B) is not for IR laser. If we use the reflection setup, we will loss more than 80 percent of laser intensity by reflection because currently the dichromatic mirror in the system is not for IR laser, so that we will not be able to collect enough laser intensity on the cells to obtain detectable SHG or THG signal. Another problem is how to synchronize the pulse laser with the scanning unit inside the FV1000 system. A TTL signal from laser will be used to trigger data acquisition of the scanning in FV1000 system. The detailed plan will be discussed in section 2.6.

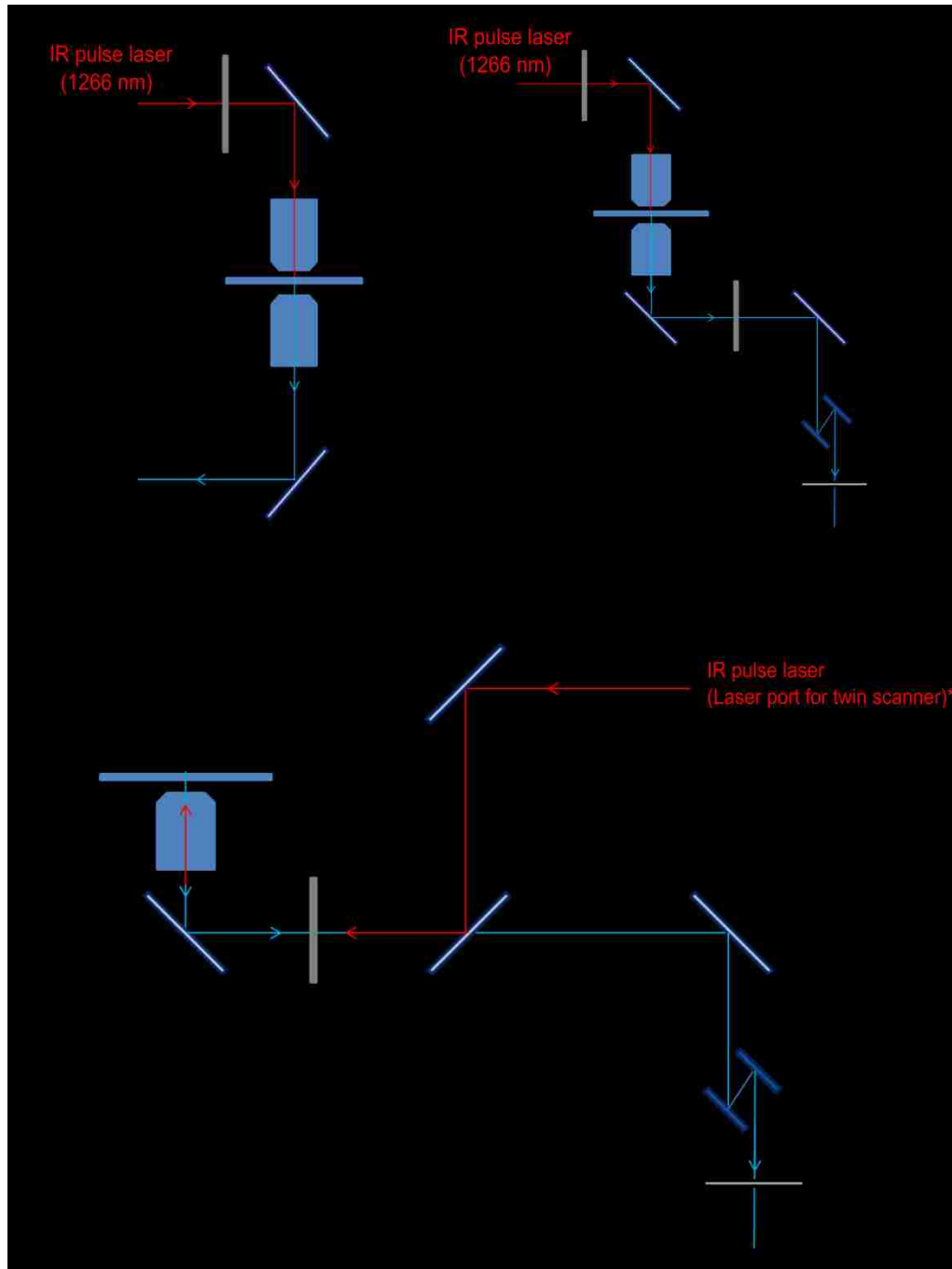


Figure 2.4 Transmission and reflection setup for SHG/THG microscopy. The excitation laser can be conducted into microscope from the top left port for transmission setup(A,B), and from the laser port in the scanning unit (upper right) for reflection setup (C). CCD (or EMCCD) camera was used in type I transmission setup (A), and PMT was used in type II transmission setup (B) and reflection setup (C) to acquire images.

2.5 Results and discussion

There are many biological objects in cells that can generate SHG/THG signal, such as myofibrils, stress fibers, microtubules and cell membrane. It was suggested that the SHG signals from HeLa cells are obtained from myosin-actin filaments. Recent studies demonstrated that in myosin-actin filaments, the main source of intrinsic SHG signal comes from the myosin heads [123, 124]. Myosin is a motor protein that plays an important role in the cells mitotic process. Myosin consists of two heavy chains, two heads and two light chains. The structure of heavy chains and heads in myosin II has large hyperpolarizability β_{zzz} . When the myosin II molecules are assembled into a bipolar thick filament, the local structure of the myosin thick filament is noncentrosymmetric (see figure 2.1), therefore the myosin thick filament is a good object for second harmonic imaging microscopy (SHIM) in live cells and biological tissues, such as stress fibers and muscle tissues.]. In epithelial cells and fibroblast cells, the myosin thick filaments and actin filaments together with crosslinker proteins compose of contractile actomyosin bundles called stress fibers [125]. Studying the assembly of stress fibers in these cells through SHIM provides insight view of the mechanism of the cellular cytoskeletal formation. During the cytokinesis stage in eukaryotic cells, actin and myosin are assembled into filaments and form a contractile ring around the cells equator. A model was developed to describe the self-assembly process [126-128]. Applying SHIM on the assembly of contractile ring would help to better understand this important and interesting phenomena during cytokinesis.

The third harmonic imaging microscopy (THIM) from HeLa cells give the information of cell's heterogeneity, especially the cell's lipids of membrane and nucleus. THIM is often used in studying embryotic development [101, 103], biological tissue synthesis and growth [129-134], biomedical diagnosis [135, 136].

Considering the features of SHIM and THIM, we will use these techniques to study: (1) the mechanisms that regulate actomyosin filament assembly in vivo, and (2) how the cells adjust their cytoskeletal network in response to the stiffness of substrates.

Firstly, we use the transmission setup (figure 2.3A) to take image of SHG and THG from KNbO_3 crystal powders. Figure 2.4A shows the bright field image of KNbO_3 powder immersed in oil. Each granule

consists of many single crystals with diameter less than $1\ \mu\text{m}$. Figure 2.4 (B) and (C) are the SHG and THG image of the same KNbO_3 crystals. Because each single crystal in the granule has different orientation of crystalline plane, each single crystal generates SHG with different intensity detected by CCD camera.

Then we change the KNbO_3 sample to starch powder sample, which is immersed in oil as well. SHIM of starch granules has been studied to distinguish starch from different species (rice, corn, potato, etc.) [137, 138]. We found our CCD camera was not sensitive enough to detect the SHG signal. So we used EMCCD camera as image acquiring instrument. With the same system as in figure 2.3A (using EMCCD camera), we obtained a SHG image of single starch granule. In order to obtain a SHG image, we have to focus the input laser beam to a smaller beam size (diameter $\sim 5\ \mu\text{m}$), so we could only obtain a SHG image of one starch granule each time. The SHG intensity profile along the red dotted line and green contour (figure 2.6B) indicate that the granule of starch has crystalline structure on the outer layer, which agrees with previous studies [138, 139].

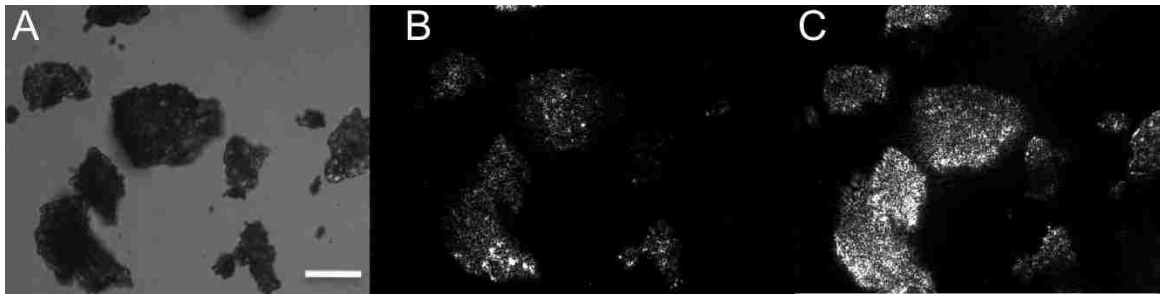


Figure 2.5 (A) Bright field image of KNbO_3 crystals. (B) SHG image collected by CCD camera with the excitation wavelength=1264nm. (C) THG image collected by CCD camera with the excitation wavelength=1500nm. Scale bar: 5 μm .

However, damage caused by the IR pulse laser is severe. As the starch granule was exposed under focused laser beam for a long time, we lost the SHG signal from the starch granule. Live cells are easily to be damaged by high intensity laser as well (see figure 2.9).

Calculation shows the intensity of laser we used (see table 2.1) was $3.4 \times 10^7 \text{ W}/\mu\text{m}^2$, under such a high intensity, the photodamage to the biological samples caused by linear and nonlinear effects are significant [37]. One major issue we need to concern is the water absorption of IR laser. See figure 2.7A, the absorption of laser by water has two peaks at the wavelength of $\sim 1460\text{nm}$ and 1940nm [140-142]. The absorption coefficient increases 20 times from 810nm to 980nm (from $\mu_a = 1.96$ to $\mu_a = 44.9$) and reaches the peak at $\lambda = 1460\text{nm}$ ($\mu_a = 3.15 \times 10^3 \text{ m}^{-1}$). The best choice for us is to avoid using the input laser with wavelength between 1400nm to 1500nm , to reduce the heat damage to live cells and biological tissue. The culture medium also contains many other ingredients that have different optical absorption coefficients. We observed that the focused laser beam ($\lambda = 1200\text{nm}$) heated up the culture medium and created a bubble by vaporizing the medium when the power of IR laser was 5 mW , which is also reported by earlier studies [143]. When pulse laser beam were focused on HeLa cells adhered on coverglass, damage to the cellular cytoskeleton occurred within a few seconds (see figure 2.8). The optical absorption by cells in culture medium is complex, therefore the wavelength of input laser should be carefully chosen in SHG/THG microscopy to minimize the photodamage to the sample. There have been some studies conducted to explore relation between the photodamage threshold intensity and the features of pulse laser, such as pulse duration and repetition rate [119, 144]. Figure 2.7B shows the threshold energy of laser damage (for fused silica and calcium fluoride) decreases with decreasing pulse duration. However, the threshold energy is not sensitive for pulse duration less than 1ps (on the left side of the red line). K. König, et al. have shown that the photodamage threshold intensity to cells with 150-fs is $8.5 \times 10^3 \text{ W}/\mu\text{m}^2$ ($\sim 7\text{mW}$ with the repetition rate of 80-MHz) [145]. Chu et al found that with repetition rate of 2GHz Ti:Sapphire laser (pulse duration: 130 fs), one could increase the incident

laser's average power after objective to $\sim 200\text{mW}$ while keeping the peak intensity to be $3 \times 10^3 \text{ W}/\mu\text{m}^2$, which increases the SHG signal by 2 orders without damaging the sample (muscle fibers) [119]. If we have to limit the power of input laser to $\sim 7\text{mW}$, then the power of SHG would be $1.5 \times 10^{-5} \text{ W}$, which is 3 orders larger than the power of SHG generated by Ti:Sapphire laser shown in table 2.1 ($7.2 \times 10^{-8} \text{ W}$).

In our lab, we have three types of lasers available, in which the repetition rates are 80MHz, 20kHz, and 1kHz specifically. It is interesting to investigate the SHG microscopy on biological tissues or cells with these lasers.

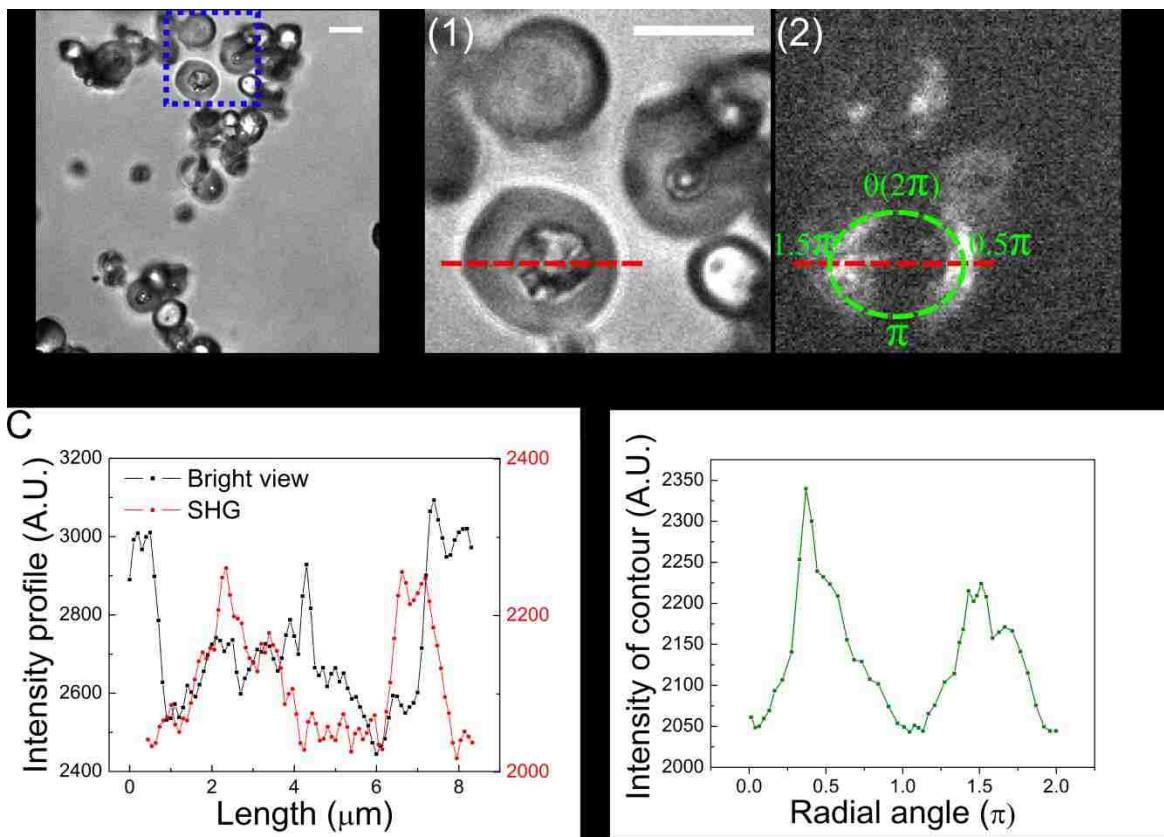


Figure 2.6 (A) Bright field image of starch granules. (B) Zoom in bright view(1) and SHG(2) image collected by EMCCD camera with the excitation wavelength=1264nm. (C) Intensity profile along the red dot line in (B). (D) Intensity profile along green dot line in (B) Scale bar: 5 μm .

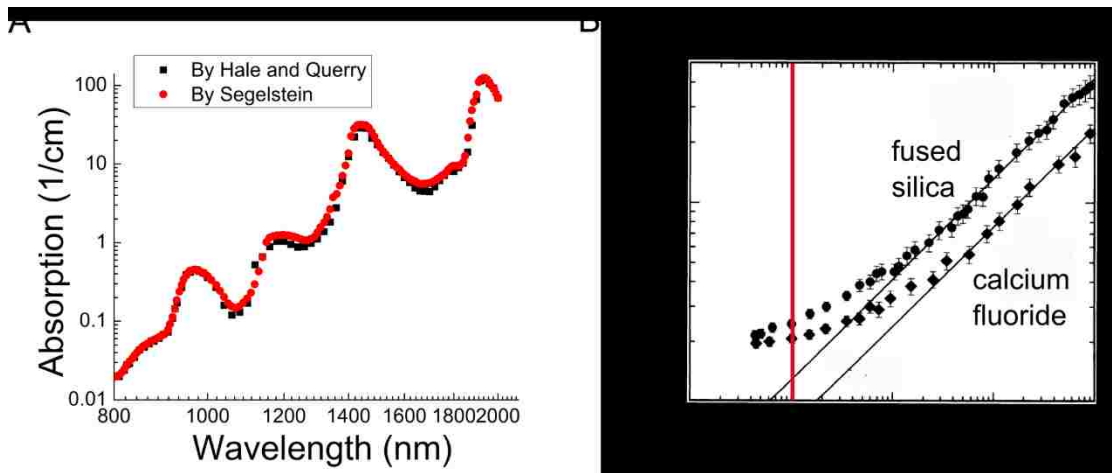


Figure 2.7.(A) The absorption coefficient of water for wavelength ranging from 800nm to 2000nm, reproduced from [146, 147]. (B) The photodamage threshold intensity to fused silica and calcium fluoride with laser pulse duration from 100 fs to 1 ns [129-130].

2.6 Future work

The SHG microscopy provides a novel method to imaging a biological system without staining it with fluorescence dye. It also provides information about microscopic structures of the biological system. As the process of SHG only happens within the focal plane, it enables higher resolution along vertical direction than confocal microscopy. Meanwhile, because it use IR pulse laser as excitation laser and there is no energy transferred into cells by SHG process, it reduces photobleaching and photodamage to the cells comparing with the confocal microscopy that uses blue/violet light as excitation laser. IR pulse laser also has a longer penetration distance than the blue light, so SHG/TPEM has a deeper detection range than confocal microscopy.

However, in practice, we found that the damage to cells by IR pulse laser was serious when we focused the laser on the sample. Studies suggest that under the input laser with same wavelength and mean intensity, biological sample can sustain integrity under pulse laser with high repetition rate. Comparing with the Ti:Sapphire laser that commonly used in SHG microscopy (45mW, 80MHz, 100-150 fs), our laser has the same mean power (45mW), but much lower repetition rate (1kHz) and longer pulse duration (1ps), resulting in the peak intensity several orders higher than Ti:Sapphire laser (see table 2.1). Further investigation of photodamage to biological tissue or live cells is necessary to help to choose proper laser (such as power and peak intensity, wavelength, pulse duration and repetition rate, etc.) in SHG/THG microscopy.

Another problem is the input laser was not synchronized with the scanning system in confocal microscope. The repetition rate of our Clark pulse laser is 1kHz, while the slowest scanning speed of our microscope is 200 μ s per pixel, so ideally, the scanning system misses 4 out of 5 pixels for each scanning. From figure 2.9B we can see that even when we project 300 scanning images into one image, we still can see the stripes in the image, which indicates that the PMT still missed a lot of pixels when it was scanning over the selected region. At present, we can tune the scanning speed through Fluoviewer (Olympus, Inc.), but synchronizing the pulse laser with the FV1000 scanning system in Olympus IX81 microscope is still necessary to obtain SHG/THG images of live cells. In order to do so, we need to use TTL signal from pulse laser to synchronize the scanner with the 1kHz pulse laser. In addition, we'd like to access the PMT signal

and choose the proper termination resistor for the PMT so that we can use a gated integrator to process the PMT signal before transmitting it further to the scanning unit. In order to use the reflection setup (Type 3), the dichromatic mirrors (#2) in figure 2.3C has to be changed to work for IR laser by reflecting IR light and let blue-green light pass through. For the next step, we will take SHG/THG image of muscle tissue, then we can monitor the stress fiber assembly in vivo by nonlinear microscopy.

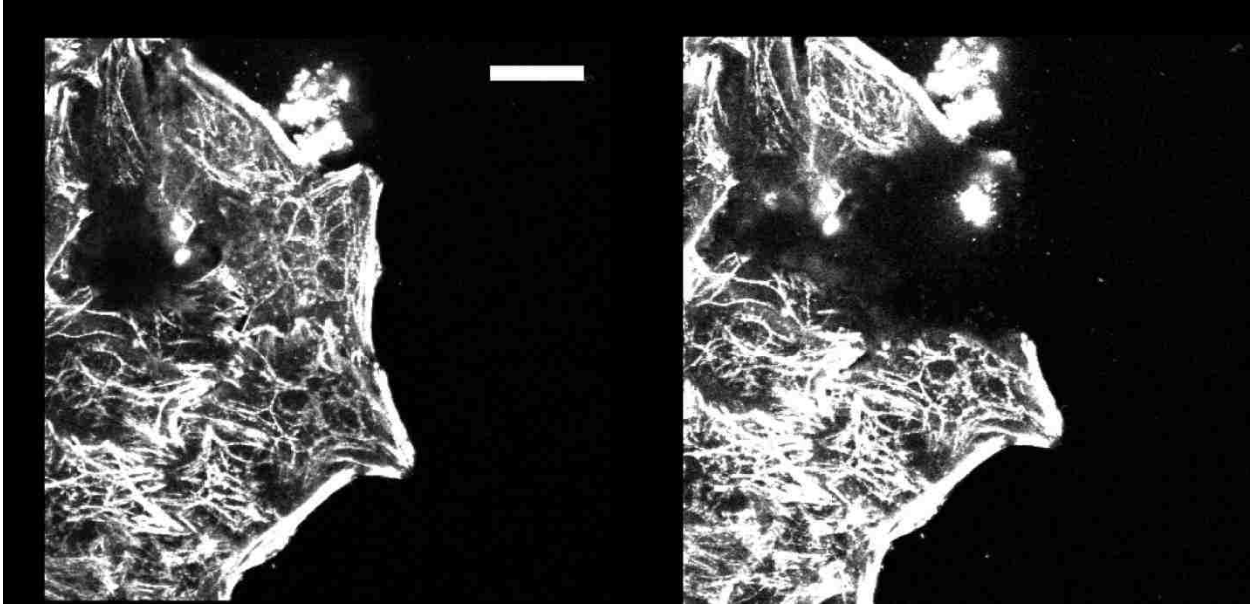


Figure 2.8 The photodamage caused by pulse laser. Comparison of MRLC-GFP image of HeLa cells before (A) and after (B) exposing the cells under focused laser beam. Scale bar: 5 μm

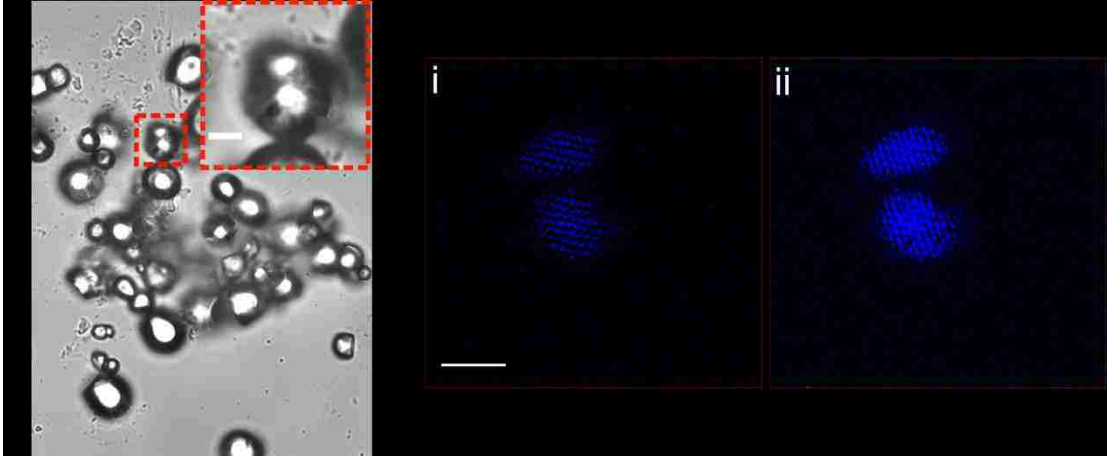


Figure 2.9 Image acquiring by PMT is not efficient without synchronizing the input pulse laser and the scanning system of the microscope. (A) Bright view of starch granules with zoom in image at the upper right corner in red box. (B) SHG image of starch granules in (A) obtained by PMT built-in Olympus FV1000 scanning unit. The images in (B) are a sum of images by scanning for 100 times and 300 times (ii).

Chapter 3

Materials and methods

3.1 HeLa cell culture and treatment

HeLa cells stably expressing GFP-tagged myosin regulatory light chain (GFP-MRLC) were obtained from Dr. K. Kamijo [148]. The culture medium was prepared with the following ingredients: 500 mL Dulbecco's Modified Eagle Medium DMEM with high glucose (4.5%) (Invitrogen #11960-044); 6 mL Glutamine (200 mM) (Invitrogen #25030-081); 5 mL sodium bicarbonate (7.5%) (Sigma #S8761); 50 mL fetal bovine serum (10%, heat activated in 56°C for 30 minutes) (Invitrogen #10082-147); 5 mL penicillin-streptomycin antibiotic solution (10,000 U/mL) (Invitrogen #15140-122).

Live HeLa cells were cultured in a flask in a NuAire CO₂ incubator (5% CO₂ at 37°C) in 5 mL DMEM and split every 3 days with the addition of 40 µL antibiotic G418 sulfate (Invitrogen #10131-035). For live imaging, cells were cultivated on 1 inch culture dishes with thin cover glass bottom for at least 48 hours before imaging or treatment with blebbistatin.

Blebbistatin (powder, Sigma #B0560) was dissolved in DMSO (Sigma #C6295) to make 100 mM solution and stored at -20°C. For blebbistatin treatment, 3 µL blebbistatin solution (100 mM) was mixed with 3 mL regular DMEM medium to make 100 µM blebbistatin medium. HeLa cells were incubated in blebbistatin medium for 60 minutes before staining for focal adhesions or actin filaments. To wash out blebbistatin we used regular DMEM medium (5mL each time) to wash the cell buffer 3 times. Washed-out cells were incubated in 5mL DMEM medium for 60 minutes before staining focal adhesions or actin filaments.

3.2 Staining actin filaments and focal adhesions

We cultured cells on coverglass for 2 days to let them fully spread before staining them. The procedure of staining actin filaments and focal adhesions in HeLa cells is as the following steps [64, 149-151]:

1. Cell fixation: cells were treated with 10% formalin solution (3.7% formaldehyde in PBS) for 15 minutes. 500 μ L of solution were added to ensure the glass cover slips are totally covered with the formalin.
2. PBS saline solution was used to rinse 3 times, for 2 min each time.
3. Permeabilization: 0.1% Triton X-100 was used for 15 min.
4. Blocking: 1% BSA was used for 30 min. BSA was stored in a -20°C freezer.
5. Rhodamine phalloidin was used to label actin filaments and vinculin primary antibody to label focal adhesions. The dye and antibody were used at 1:100 in PBS (500 μ L on each coverglass). The antibody and dye solution was allowed to react for at least 1 hour at 37°C . For imaging at a different day the sample was covered in aluminum foil stored at 4°C .
6. PBS solution was used to rinse 3 times (2 minutes each time).
7. Nuclei were also stained with Hoechst dye (0.002 mg/ml in aqueous solution) for 2-5 min (using 500 μ L).
8. dH_2O was used to rinse off the unbound dyes 3 times (2 minutes each time). The sample was then washed and stored in PBS solution.

3.3 Microscopy and image process

We used an Olympus FV1000 confocal microscope to take time-lapse images of HeLa cells. The lens we used was an Olympus UPLAN 100X oil immerse objective (NA=1.3). We focused on the adhered part of the cells above the glass slide. Multi-channel excitation allowed us to obtain images of MRLC-GFP, actin filaments, focal adhesions and nuclei of cells after staining them with different fluorescence dyes. To achieve the best S/N and minimum photo-bleaching, and obtain the comparable images of HeLa cells with different treatments, we used the following settings for the microscopy consistently,

1. Scanning speed: 2 μ s/pixel.
2. Image resolution in x-y plane: 1024x1024 pixel, 62nm/pixel.
3. Z-step size when taking 3-D image: step size=0.5 μ m.
4. When taking time lapse images, the speed is 10 sec/slice for short movies, and 1min/slice for long movies.

5. Other parameters: 10% of maximum power of excitation laser, HV=640V, offset=10 to achieve the best S/N and minimum photo-bleaching effect for the images.

Photobleaching correction was performed as follows. Firstly, we subtracted the out-of-cell background separately at each frame. We then calculated total intensity of each slice vs. time. Next, we fit this curve with a single exponential decay $I(t) = I_0 \exp(-t/t_0)$ to obtain I_0 and t_0 . Finally, we multiplied each frame with $\exp(t/t_0)$.

The cell boundary was manually selected in ImageJ. The MRLC-GFP intensity within the selected region (ROI) was measured on the photobleached corrected images. The cell spread area was measured by fitting an active contour to the cell boundary using JFilament2D [152]. To measure the number of focal adhesions in vinculin-stained cells we binarized the images, applied a band-pass filter and used the analyze particles function in ImageJ, see Fig. 3.1 and [153].

3.4 Preparation of polyacrylamide substrates

Polyacrylamide substrates are widely used to study how cells respond to their environment mechanically and physiologically. The Young's modulus of the polyacrylamide substrate is tunable by tuning the volume concentration of crosslinker N-methylene-bis-acrylamide (BIS) in the gel [154, 155], ranging from 400Pa to 60kPa.

Making polyacrylamide thin gels consists of the following steps.

1. A 22mm² is put under flame and is then let cool down.
2. A cotton swab is used to evenly and thoroughly coat the coverslip with sterile filtered 0.1% NaOH. The coverslip is dried in air until a filmly coat appears.
3. A p100 pipette tip is used to spread an even but thin coat of silane onto the surface of The coverslip (30μL). The silane coating is allowed to dry (at room temperature, 5-10 minutes). The coated coverslips are places with the silane side up in a Petri dish.
4. The coverslips are washed thoroughly with ddH₂O (3 times, 10 minutes each), tapping the dish vigorously to remove excess liquid.

5. The coverslips are incubated in 70% glutaraldehyde (1:140 in (volume) in PBS) at room temperature for 30 minutes. (1.2mL 25% solution in 60mL PBS).
6. The coverslips are washed thoroughly with ddH₂O (3 times, 5-10 minutes each).
7. The coverslips are placed face up to dry.
8. After fully drying, the activated coverslips were used immediately or stored for several weeks in a dry environment (under tissue paper).
9. In a microcentrifuge tube, the solutions required for gel preparation are mixed with 0.5M HEPES, PH 4.22: 5.95g in 50 mL H₂O, PH to 4.22 (see table 3.1 for procedure).
10. The gel solution is degassed using a vacuum flask or chamber for at least 30 minutes.
11. While the solutions are being degassed, an additional set of equivalent-sized coverslips (18mm round) are evenly coated with Rain-X. The Rain-X coating is allowed to dry at room temperature for 5-10 minutes, before gently buffing the coverslip using a Kimwipe.
12. The activated coverslips are placed face-up on a secured piece of paraffin.
13. 5 μ L of freshly made 10% ammonium persulphate (w:v in ddH₂O) are added per 1 mL of fully degassed acrylamide solution, mix well, and quickly dispense 20 μ L of solution onto each activated coverslip. The Rain-X treated coverslip was carefully placed on top without trapping air bubbles and allow the gel solution to polymerize at room temperature for 25-60 minutes (usually 45 minutes).

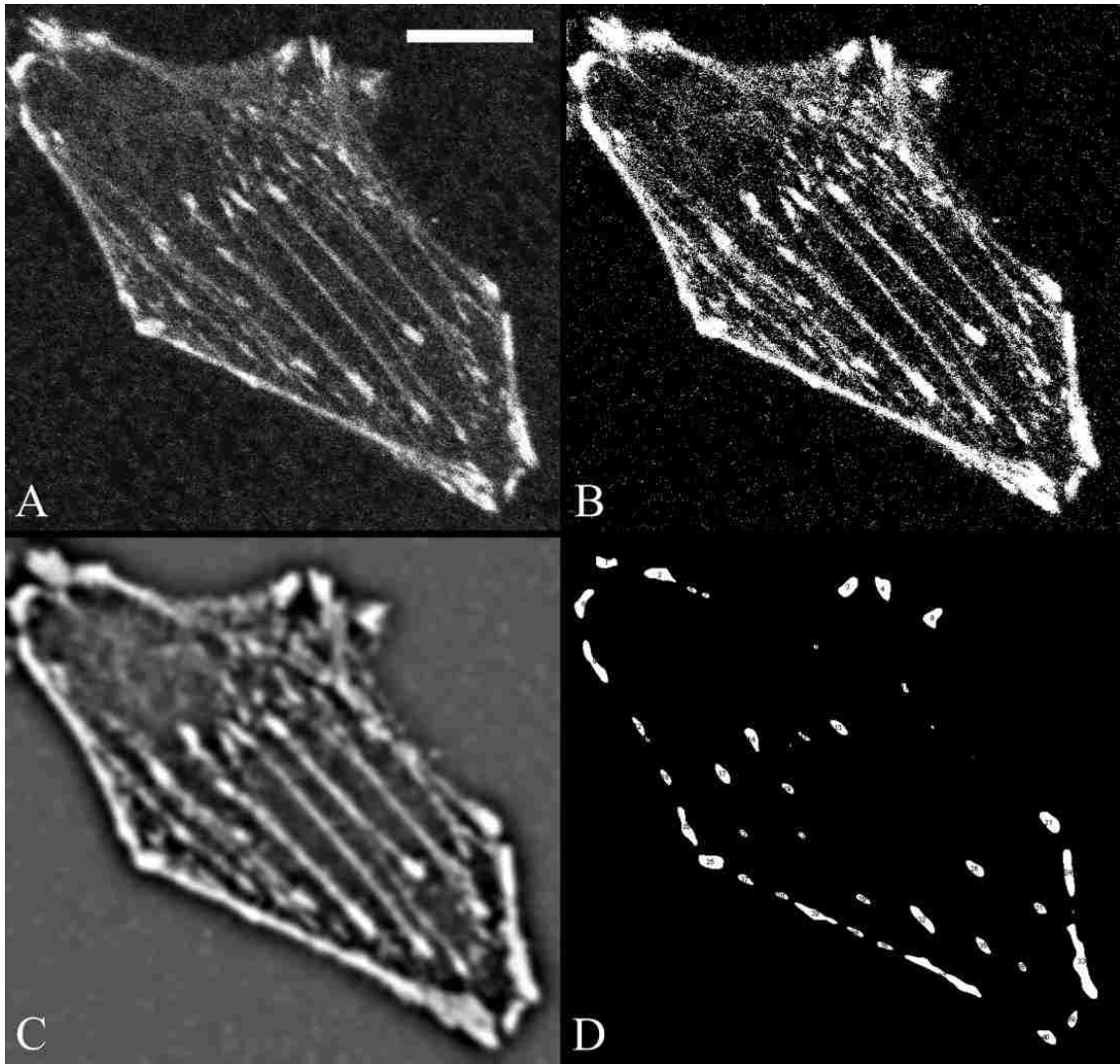


Figure 3.1. Measurement of focal adhesions from a confocal fluorescence image of a HeLa cell [153]. (A) The original confocal fluorescence image of a HeLa cell stained with vinculin antibody. (B) Image of panel (A) converted into a binary image with proper threshold. (C) Bandpass filter is used to select spots that have the size of focal adhesions. (D) The particle analyze function of ImageJ is used with proper threshold (of intensity and size) to obtain the information of focal adhesions. (scale bar=5 μm)

.Functionalization of Polyacrylamide thin gels:

1. The following items are prepared:
 - Sulfo-SANPAH (note: must turn off lights when in use): 0.5mg.
 - DMSO: 5 μ L
 - 50mM HEPES (PH 8): 1mL.
2. DMSO is added first, then slowly the HEPES is added to the Sulfo-SANPAH while vortexing.
3. 100 μ L of above solution is placed onto polymerized polyacrylamide, making sure it is well spread.
4. The sample is incubated under UV light for 15 minutes.
5. The pink liquid is aspirated off.
6. Each plate with 50 mM HEPES is washed twice and then put on shaker with HEPES for 10 min.
7. The secondary substrate is then placed onto the activated polyacrylamide and incubated for 4 hours under UV at room temperature (collagen I: 0.2 mg/ml, Fibronectin: 5-30 μ g/ml).

The thickness of the polyacrylamide film was controlled by the volume of the gel deposited on the circular coverglass. We dropped 100 μ L gel on the coverglass first, then put on 1mm circular coverglass on the top of the gel to press the gel into a thin round film with fixed area and fixed thickness (~150 μ m).

The Young's modulus of the polyacrylamide substrate could be measured by using atomic force microscopy (AFM) by using the probe tip of AFM to press beads on the gel and measure the force-displacement relationship [156].

Table 3.1 Preparation of 1ml Polyarylamide Gel Solutions for Given Elastic Modulus (Yeung et al., 2005)

Elastic modulus (Pa)	140	400	1050	5000	60,000
Acrylamide (%)	3	3	3	5.5	10
Bis-acrylamide (%)	0.04	0.05	0.1	0.15	0.5
40% Acrylamide(μ L)	75	75	75	137.5	250
2% Bis-acrylamide(μ L)	20	25	50	75	250
0.5M HEPES. PH 4..22 (μ L)	100	100	100	100	100
TEMED (μ L)	0.5	0.5	0.5	0.5	0.5
ddH ₂ O (μ L)	648.9	643.9	618.9	541.4	243.9

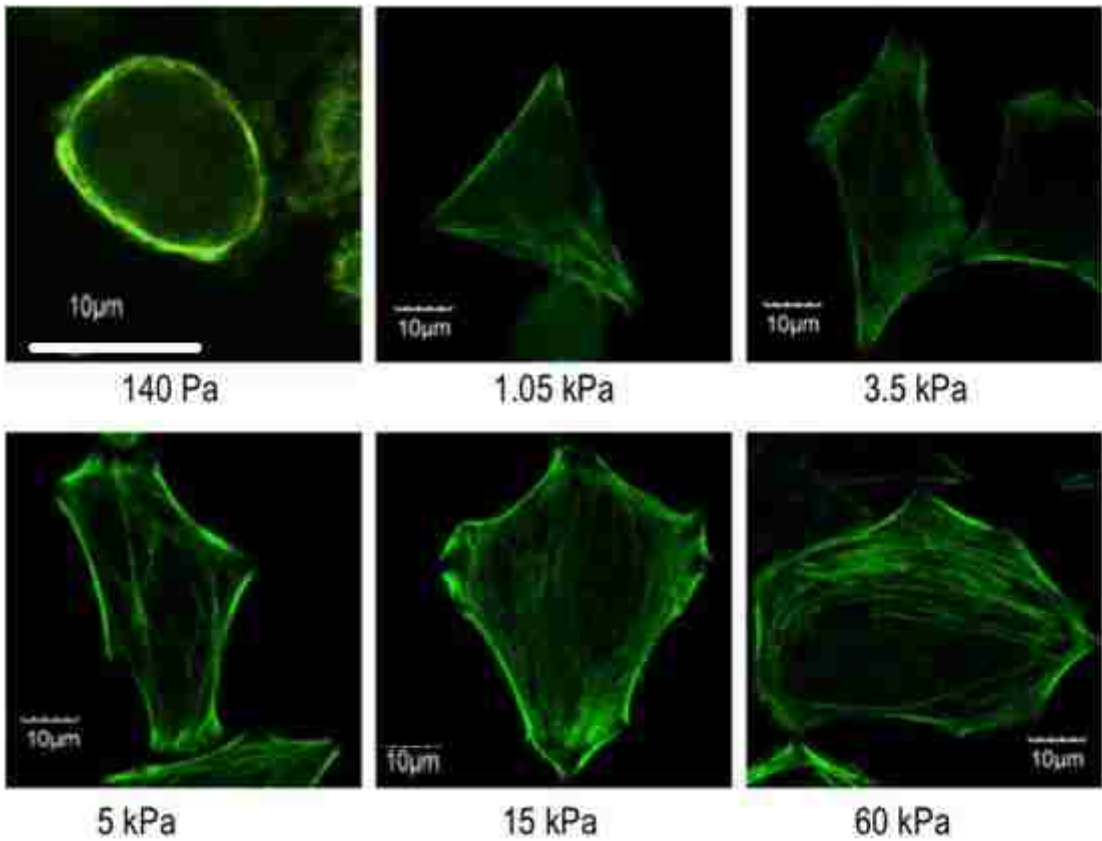


Figure 3.2. Images of HeLa cells expressing MRLC-GFP cultivated on polyacrylamide substrates with Young's modulus of stiffness ranging from 140 Pa TO 60 kPa. The adherent area of the cells increases from about $400 \mu\text{m}^2$ on 140 Pa substrates to $900 \mu\text{m}^2$ on 60 kPa. With the increasing stiffness of the substrates, cells are shown to be more polarized in morphology with more actomyosin bundles in the medial cortex.

Chapter 4

Fluorescence microscopy of medial cortex in HeLa cells and image analysis

4.1 Introduction

The ability of cells to adhere and exert forces on substrates of different chemical and mechanical composition relies on their ability to form adhesions and transmit signals to the cytoskeleton [157]. The actin filaments and myosin motors in the cell cortex connect to focal adhesions (FAs) and adjust to form networks below the plasma membrane that maintain tension and traction, which in turn determines cell shape and cell mechanical rigidity [158-160]. Bundled actomyosin structures, such as stress fibers anchor at focal adhesions and at the cell nucleus, are important subcellular structures for generating cell traction and adhesion [77]. Stress fibers are bundles of actin filaments containing myosin-II motors and α -actinin cross-linker proteins. They can form from different pathways and can have different orientation with respect to the cell axis as well as varying distribution of actin filament polarity [64, 161, 162].

Stress fibers can form from actin filaments polymerized at cell protrusions: in motile cells, actin filaments nucleated at lamellipodia and filopodia undergo retrograde flow and are pulled together into bundles as transverse actin-arcs and dorsal stress fibers [64, 161]. Cortical actomyosin fibers can also form at the cell cortex away from leading edge protrusions (or away from the contractile back for the case of cells using bleb-based motility). It was recently shown that the cortex of adhered cells consists of dynamic formin, actin and myosin-II foci that contract and coalesce into clumps when actin filaments are depolymerized with Latrunculin A [163]. Constant turnover of the foci was found to be necessary for the observed patterns [163]. This ability of the animal cell cortex to reorganize into a different dynamic steady states upon a perturbation reflects its inherent plasticity and is reminiscent of the morphological changes seen in simpler organisms such as fission yeast where, depending on the concentration of cross-linker proteins, the mitotic medial actin network can organize into different morphologies such as clumps, contractile rings, and extended meshworks. In vitro experiments reconstituting actomyosin structures from

a set of purified components demonstrate cytoskeletal plasticity and hold promise for a systematic understanding of the dynamical phase diagram of actomyosin systems [20, 77-79].

In this Chapter we study live cells and present experiments that further explore the idea that the cell cortex exists in a dynamic state that allows it to readily change morphology in response to a perturbation. For the case of adherent cells this perturbation is the linking of the cytoskeleton to a substrate through focal adhesions. In addition to the kinetics of turnover and contraction mentioned above, we anticipate an important role of mechanical forces and tension: the cortical actin and myosin concentrations respond to both external and internal forces: myosin-II and cross-linkers accumulate at sites of micropipette aspiration in a manner that depends on actin filament cross-linker concentration [155, 164].

The precise kinetics of cortical cytoskeletal dynamics depend on many proteins and signaling pathways [161]. Here we do not attempt to address the precise molecular regulation but instead look at the collective behavior of myosin-II distribution. Using statistical analysis of our data we outline the basic mechanisms that should combine to generate the observed patterns. We also do not try to describe the full pathway leading to stress fiber formation, which may involve a cascade of stabilization processes [165], but rather describe the mechanisms that provide the initial geometric and mechanical properties necessary to stabilize an aligned actomyosin structure. To address this question experimentally we used confocal microscopy to study HeLa cells stably expressing MRLC-GFP (that binds to myosin-II) adhered to a glass slide. We chose this system for its simplicity and for allowing imaging the medial cell cortex. Numerical simulations presented in Chapter 5 based on our measurements provide support for our proposed underlying mechanisms.

4.2 The activity of myosin II is important for the assembly of a medial actomyosin network in HeLa cells

We cultured HeLa cells tagged with MRLC-GFP on cover glass for two days before experiments. On the third day, we prepared the cells on coverglass in 3 ways. 1) Cells cultured in regular DMEM medium were taken as control cells. 2) Cells treated by 100uM blebbistatin for 60 minutes were taken as myosin II inhibited cells. 3) Cells firstly treated by 100uM blebbistatin for 60 minutes, then washout

blebbistatin and cultured in regular DMEM medium for 60 minutes were considered as myosin II reactivated cells. After all the treatment and preparation, cells were fixed and stained for F-actin and focal adhesions following the procedure and protocol in section 3.2.

Figure 4.1 shows the MRLC-GFP images of HeLa cells in control state. Based on the morphology of the actomyosin network in the central region on the basal plane of the cells, we defined 3 types of actomyosin networks of HeLa cells. In Type I cells, there are long filament bundles with a number of mature FAs in the middle of the cells. In Type II cells, there are short fibers or meshwork with a few FAs in the middle of the cells. In Type III cells, there is neither visible filament nor meshwork, with very small amount of FAs (usually less than 5 per cell) in the middle of the cells. There is no significant difference for the mean MRLC-GFP intensity of Type I, II and III cells, however, when comparing the MRLC-GFP intensity in the middle of the cells (without cell boundary), the MRLC-GFP intensity in Type II and III cells is about $\frac{1}{2}$ of the intensity in Type I cells (see figure 4.1). For control cells, the number of FAs is 80 ± 23 , 60 ± 25 and 44 ± 21 per cell in Type I, II and III cells, while the spreading area has no significant difference in three different cell types (1000 ± 400 , 870 ± 290 , $950 \pm 400 \mu\text{m}^2$ respectively).

The standard deviation for the number of FAs is large because it is difficult to isolate and distinguish the FAs on the boundary of the cell (see Chapter 3 for methods of quantifying FAs by ImageJ). It is interesting to notice that the number of FAs in the middle of Type II cells is larger than that in Type I cells (23 ± 11 vs. 11 ± 7), which is opposite to the MRLC-GFP intensity in the middle of Type I (470 ± 230) and II (180 ± 90) cells. The density of FAs in the middle of Type I and II cells are 1.4 ± 1.1 and 3.9 ± 2.4 per $100 \mu\text{m}^2$ individually. Type III cells are very different from Type I and II cells as there are virtually no actomyosin network or FAs (2.3 ± 0.6) except myosin II minifilaments and foci in the middle of these cells, although Type III cells have similar spreading area as Type I and II cells do. Because of the smaller density of myosin II minifilaments and FAs in Type III cells, it is probably difficult for these cells to form a stable filament bundle or network in their middle as in Type I or Type II cells. From the analysis above, we conclude that a certain level of density of myosin II minifilament and FAs is important for a cell to be able to assemble an actomyosin network in the middle. With decreasing myosin minifilament and FA density, the actomyosin network in the middle of a cell changes from thick bundles/ meshwork, to no fiber or or fiber network at all.

To understand how the activity of myosin II affects the process of actomyosin network assembly in the middle of HeLa cells, we conducted experiments with myosin-II inhibitor blebbistatin [166] (see Materials and Methods). Fig. 4.2 A shows cells expressing MRLC-GFP cultured with the same procedure as the control cells in Fig. 4.1 but treated with 100 μ M blebbistatin for 60 min before fixing and staining for vinculin. We observed a lower fraction of Type I cells and increased Type II and III as compared to control cells, reflecting the disassembly of myosin fibers. This indicates that myosin motor activity is important in the maintenance of long fibers. Fig. 4.2 B shows results with cells treated with 100 μ M blebbistatin for 60 min and then washed out by regular DMEM medium for 60 minutes before fixing and staining. The fraction of Type I cells increased to a value near that in control cells (Fig. 4.1), which indicates that MRLC-GFP fibers are restored after restoring myosin motor activity.

The number of focal adhesions found in the middle of Type II cells also decreases in the presence of blebbistatin (see Fig. 4.2 C), indicating that focal adhesions are also stabilized by stress. This result is consistent with other studies [20, 160, 167, 168], such as in [164] whose authors found the number of nascent focal adhesions in fibroblasts decreases upon blebbistatin treatment. Thus, blebbistatin perturbs the medial network in Type I and II cells that lose medial adhesions and some Type I cells become Type II or III; upon blebbistatin removal, a medial network of fibers can reform within 60 min but the overall number of medial adhesions does not recover to the control level.

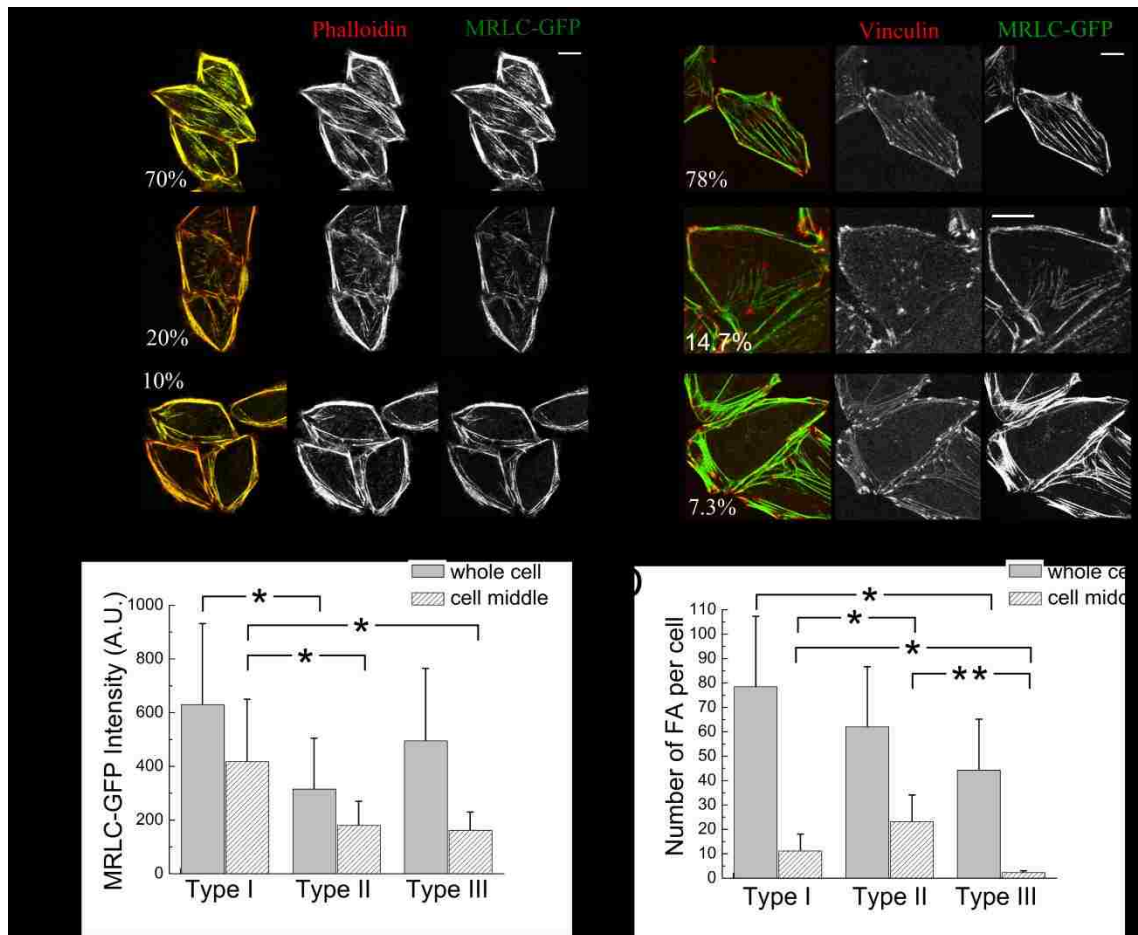


Figure 4.1. Actomyosin fibers and networks in HeLa cells adhered to glass slides. (A) Fluorescence microscopy images (single confocal slice through the bottom part) of control cells showing myosin labeled with MRLC-GFP and actin filaments stained with rhodamine phalloidin. (B) Images of cells expressing MRLC-GFP and focal adhesions stained with vinculin antibody. All cells show peripheral stress fibers but structures in the medial cell part vary among cells on the same glass slide. We classify cells into three types ($n = 70$ cells for A and $n = 41$ in B). In Type I cells, medial myosin and actin form fibers of length comparable to the cell size; these fibers connect focal adhesions located at the boundary and in the middle cellular region. In Type II cells, medial myosin and actin form short fibers and networks anchored by focal adhesions located at the boundary and in the middle cellular region. In Type III cells, there are no detectable medial fibers, networks or focal adhesions. (C) Comparison of ratio between average MRLC-GFP intensity in cell middle and whole cell within a single confocal slice through the bottom part of the cell ($n = 41$). Type I and Type II cells have larger a larger ration compared to Type III. (D) Total number of focal adhesions for three cell types ($n = 41$). Type II cells have the most adhesions in the cell middle while Type III have close to none. *: $p < 0.05$; **: $p < 0.01$. Bars: 10 μm .

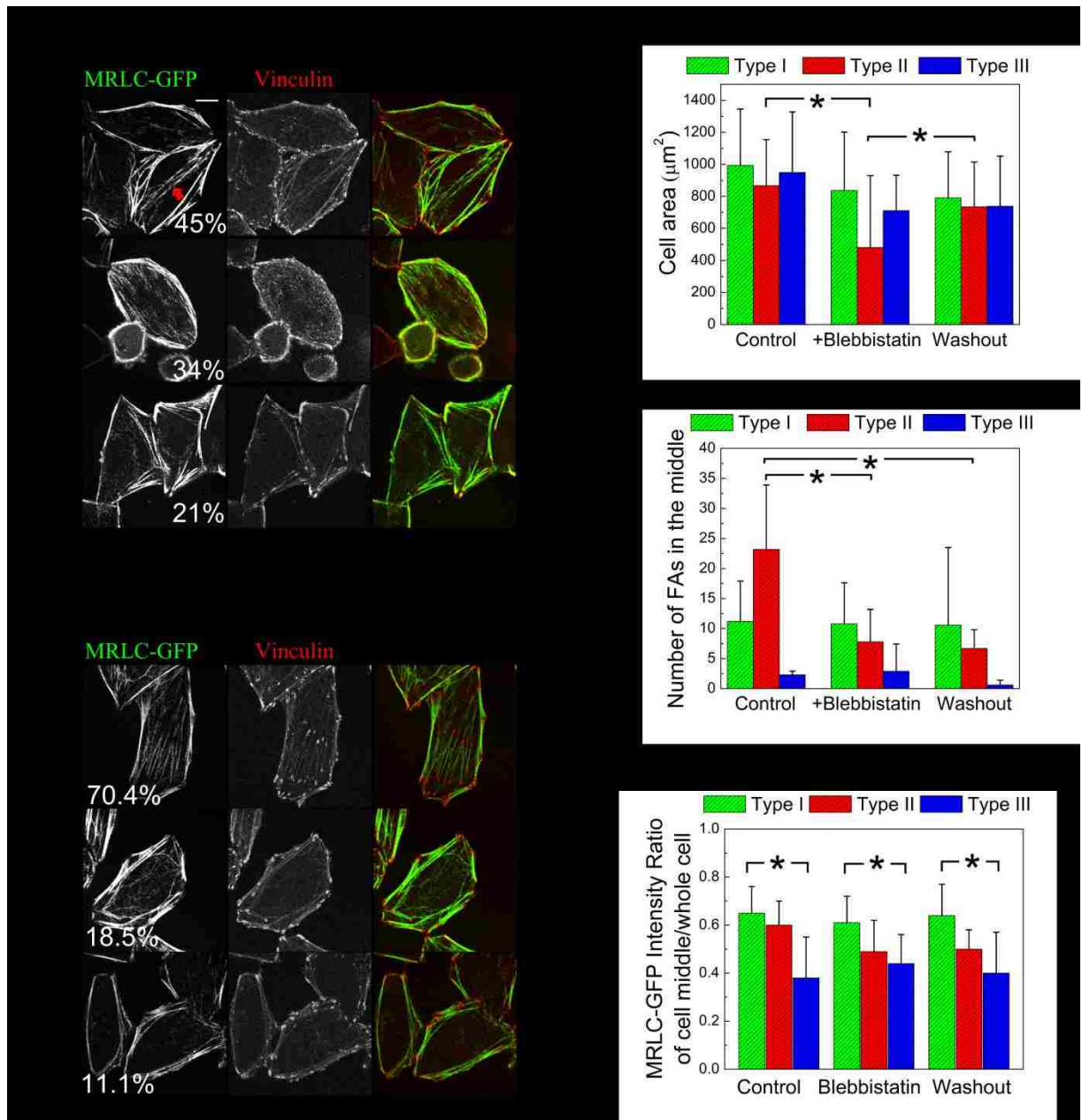


Figure 4.2. Images of HeLa cells expressing MRLC-GFP (green) stained with vinculin (red) after treatment with blebbistatin. (A) Cells treated with 100 μM blebbistatin for 60 min. Red arrow indicates fibers in Type I cells that remain after treatment. (B) Cells treated with 100 μM blebbistatin for 60 minutes followed by washout with regular DMEM medium. Images were taken 60 min after the washout. (C) Cell area for different cell types. Type II cells are cells with smaller area in the presence of blebbistatin. (D) Total number of focal adhesions for different cell types. Type II cells are cells with less adhesions in the presence of blebbistatin and after washout. (E) Ratio of average MRLC-GFP intensity in cell middle over the average intensity over whole cell for different cell types. The ratios for a given cell type are similar in control cells and for cells in blebbistatin and following blebbistatin washout. Cells analyzed: control $n = 41$; blebbistatin $n = 62$; washout $n = 54$. * $p < 0.05$. Bar: 10 μm .

We did not detect a statistically-significant change in the ratio of MRLC-GFP intensity in the cell middle over the whole cell by blebbistatin (see Fig. 4.2 E). Interestingly, the absolute average MRLC-GFP intensity in the medial cortex in Type II and III cells is unchanged by blebbistatin (see Fig.4.3 B and C). This means that differences in medial myosin organization after blebbistatin treatment are due to changes in the contractile properties of a network that contains the same amount of myosin. The medial MRLC-GFP intensity of Type I cells decreases in blebbistatin (see Fig. 4.3 A), likely due to the disassembly of some stress-stabilized medial fibers in these cells.

We also noticed that total cell adhesion area decreases slightly when adding blebbistatin and increases again after blebbistatin washout (see Fig. 4.4). This trend is also seen in analysis of fixed cells in Fig. 4.2 C and most notably for Type II cells that have smaller area (some cells, not included in Fig. 4.2 C, lost adherence to the substrate and become round, see middle row of Fig. 4.2 A). Loss and recovery of adherence in the medial cortex as well as in the peripheral stress fibers and protrusions likely accounts for this trend.

As a summary, we found that the activity of myosin II and existence of FAs are important to the assembly of actomyosin network. Both the morphology and dynamical process of the actomyosin network assembly in the middle of cells were correlated to the myosin II concentration and activity in the cells as well as the number of FAs, which help to anchor and stabilize the bundles and maintain the stiffness of the cytoskeletal network of the cells. In the next sections, we will use image correlation spectroscopy (ICS) to study how the activity of myosin II affect the dynamical process of actomyosin network assembly/disassembly in the medial cortex of HeLa cells.

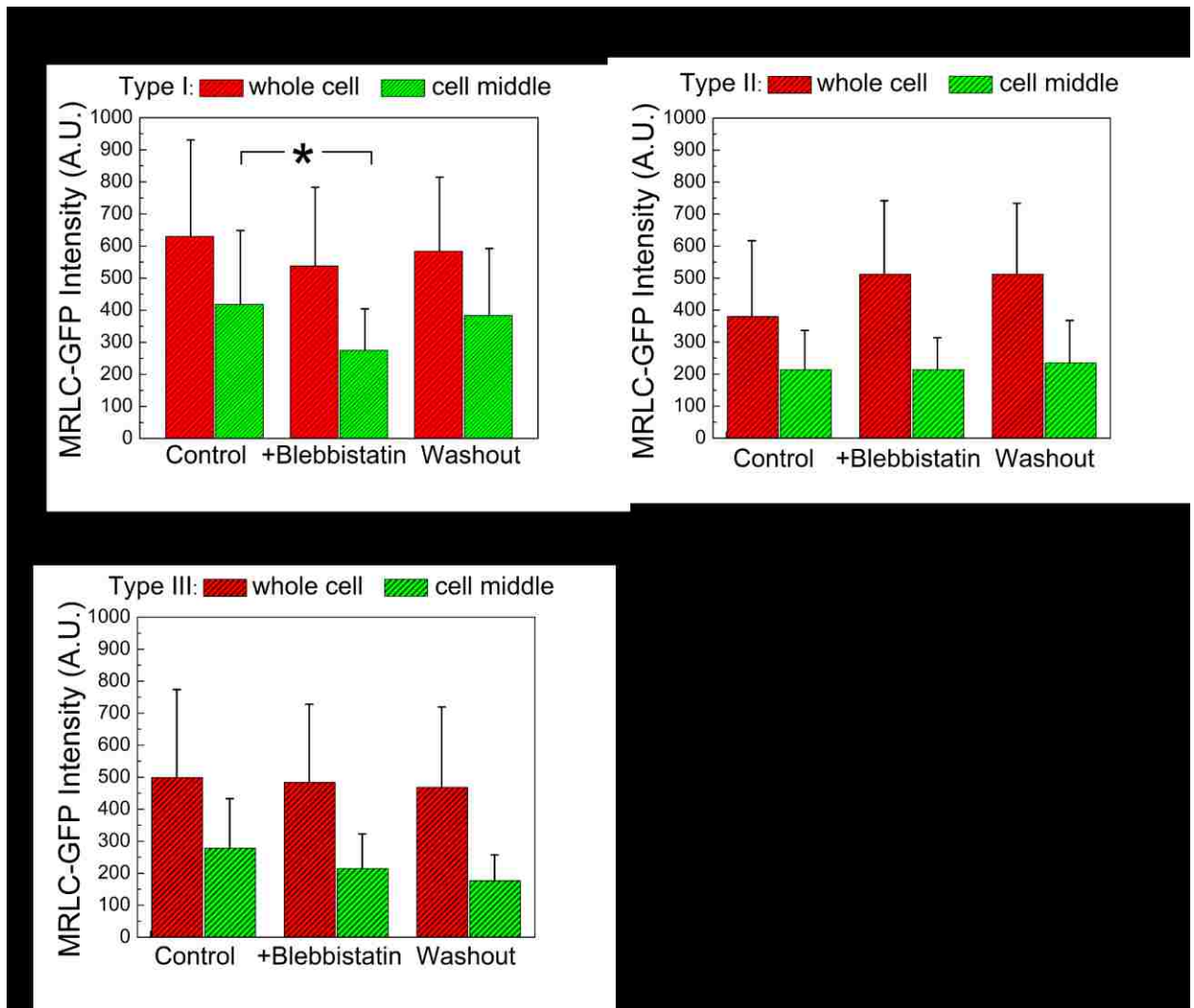


Figure 4.3. The MRLC-GFP intensity of adhered part of cortex in Type I (A), II (B) and III (C) HeLa cells. Red indicates the mean MRLC-GFP intensity of whole cells including the peripheral fibers. Green indicates the mean MRLC-GFP intensity in the medial. MRLC-GFP intensity were measured by ImageJ (NIH) on untreated cells (41 cells), blebbistatin-treated cells (62 cells), and cells that recovered from blebbistatin (54 cells), see Materials and Methods. Panel A shows that blebbistatin treatment results in a decrease of the intensity of MRLC-GFP in the medial cortex of Type I cells, which is largely due to the disassembly of the permanent fibers in Type I cells. There is no significant change of MRLC-GFP intensity before and after blebbistatin treatment in Type II and III cells (B,C). * $p < 0.05$.

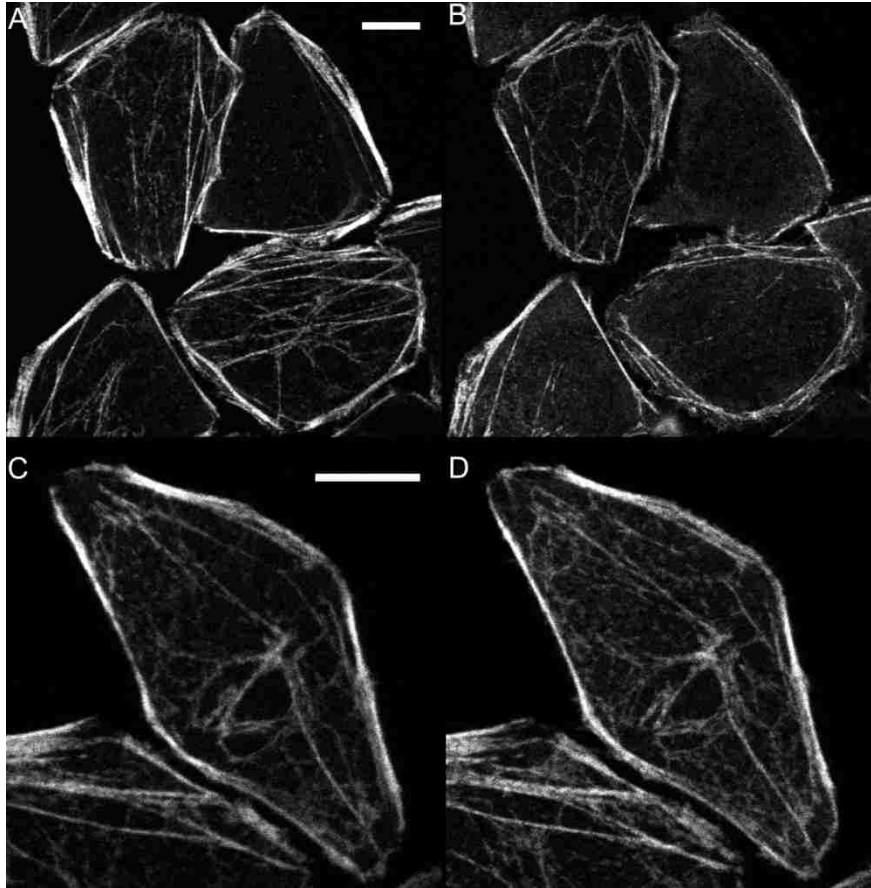


Figure 4.4. Images of same cells before and after blebbistatin treatment (A,B) or before/after blebbistatin washout (C,D). On average, the adhesion area of HeLa cells decreases after addition of blebbistatin, and recovers when washing out blebbistatin with DMEM medium (Fig. 4D). Panels A and B show images of HeLa cell expressing MRLC-GFP before and after 60 min in 100 μ M blebbistatin. Images show disassembly of medial fibers and a decrease in the adhesion area by 10% (from 646 μ m² to 575 μ m²) for the cell at the top left. The bottom right cell transformed from Type I into Type III (lack of medial fibers). Panels C and D show changes after 60 min in blebbistatin (C) and 60 min after blebbistatin washout (D). Medial network and fibers were recovered; the adhesion area for this cell decreased from 679 to 662 μ m² but for other cells (mostly Type II) the area was found to increase (see also Fig. 4.2C). Bar: 10 μ m.

4.3 Dynamics of medial cortical myosin in adhered HeLa cells.

By imaging a single confocal slice focused at the adherent part of the cell, we observed that peripheral stress fibers labeled by MRLC-GFP maintain their position and shape over 30 min. The medial part of the cell cortex however is very dynamic over the same timescale, as shown in Fig. 4.5.

Fig. 4.5A shows a Type I cell in which MRLC-GFP foci appear and disappear near more stable peripheral and medial fibers. During this turnover process, the foci align to form transient fibers over $\sim 5 \mu\text{m}$ (see panel at 6:00 min in Fig. 4.5 A). The foci turnover process is more evident in the volume kymograph in the first panel of Fig. 4.5D, which is constructed from cell region of the panels in Fig. 4.5 A. In this kymograph the transient MRLC-GFP foci appear as bright spots.

Fig. 4.5 B shows a Type II cell where MRLC-GFP foci turnover and transient alignment is evident in the panels showing an enlarged region of cell cortex. This turnover is also seen in the transient spots in the volume kymograph in the middle panel of Fig. 4.5 D. The kymograph highlights another process: directed foci motion. Foci motion is evidently a result of contraction and the likely origin of transient clumping (see panel at 1:40 in Fig. 4.5B). Similar dynamics to the Type II cell of Fig. 4.5 B are observed in the cells of Fig. 4.5 C, which we would classify as Type III, and the corresponding volume kymograph in the last panel in Fig. 4.5 D.

Taken together, Fig. 4.1 and 4.5 indicate that the process of medial cortical fiber formation results from myosin foci assembly and disassembly at the cell cortex (likely in the form of mini-filaments minifilaments on cell cortex [160, 169]), alignment (likely through pulling on actin filaments nucleated near the cell cortex) and stabilization of linear elements. Since similar dynamics are observed in all three cell types, the different cortical morphologies observed seems correlated with the ability of cells to form fibers anchored at focal adhesions in the medial part of the cell cortex. These results also highlight a pathway to actomyosin fiber formation different to that of more motile cells. In many motile cells peripheral arcs and fibers form through myosin-mediated collapse of peripheral lamellipodial protrusions [64, 151, 170, 171]. By contrast, the fiber pattern of HeLa cells on glass slides is dependent on the steady state properties of non-protruding medial cell cortex. In some cells such as Fig. 4.5B, an outward rather than inward flow can be observed.

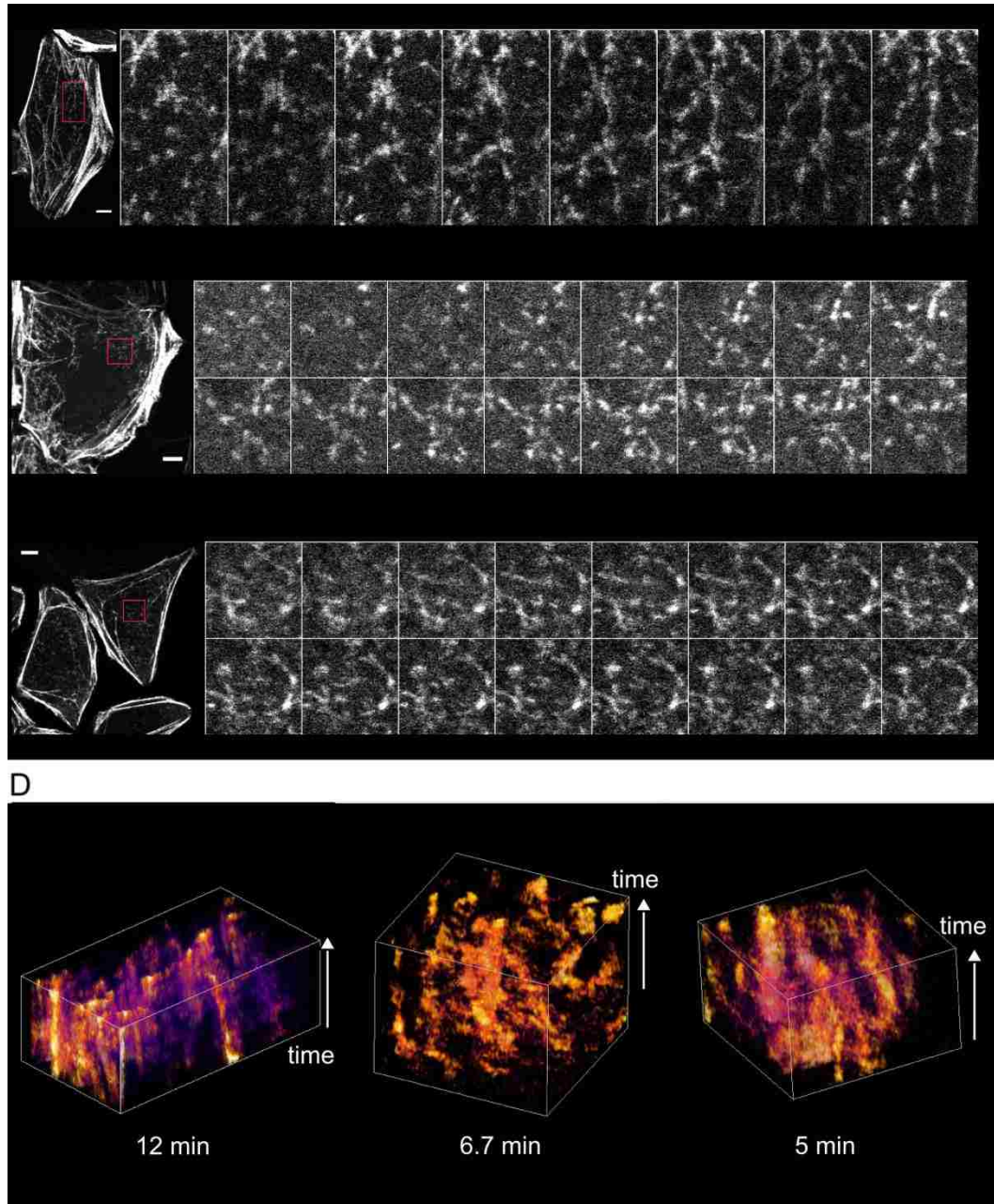


Figure 4.5. Time-lapse fluorescence microscopy images of HeLa cells expressing MRLC-GFP reveal a dynamic cortical network in which MRLC-GFP foci appear, disappear, clump and contract. Single confocal slices through cell bottom. Montage panels to the right of A, B, C correspond to red box of left panel. (A) MRLC-GFP foci in a Type I cell assemble into linear structures and subsequently disassemble within 3 min. (B) MRLC-GFP foci appearance/disappearance and contraction in a Type II cell. In this cell the intensity of the medial MRLC-GFP network increases towards the periphery. MRLC-GFP foci in the medial region flow, on average, towards the cell periphery. (C) MRLC-GFP foci appearance/disappearance and contraction in Type III cells. The top right cell can also be classified as Type II. (D) 3D kymographs of montages of panels A, B and C. Foci appearance and disappearance are evident as bright spots. Total time is indicated in each panel. Contraction corresponds to diagonal features in second and third kymograph. Bars: 5 μ m.

4.4 Spatial-temporal image correlation spectroscopy (STICS) analysis of cortical MRLC-GFP in adhered HeLa cells

To quantify medial MRLC-GFP dynamics, we used spatio-temporal image correlation spectroscopy (STICS) [172]. We used this method since the density and complexity of foci motions precluded methods such as single-particle tracking even with manual editing [173]. STICS allows measurement of average correlations of intensity over space and time, which provides information on the diffusive, transport, and turnover kinetics of the fluorescently-labeled molecules [172, 174-176]. It is a useful tool in images such as those of Fig. 4.5 in which intensity correlations persist from frame to frame but the motion of individual myosin foci cannot be tracked with good accuracy. The STICS function of relative distances ξ and η (along the x and y directions) and relative time τ is:

$$r(\xi, \eta, \tau) = \frac{\langle \delta I(x, y, t) \delta I(x + \xi, y + \eta, t + \tau) \rangle}{\bar{I}(t) \bar{I}(t + \tau)} \quad (4.1)$$

where $I(x, y, t)$ is intensity at pixels x, y of an $N \times N$ pixels image at frame corresponding to time t , $\bar{I}(t)$ is the average intensity at time t and $\delta I(x, y, t) = I(x, y, t) - \bar{I}(t)$. The averages in Eq. (1) are averages over x, y and t .

We calculated $r(\xi, \eta, \tau)$ by selecting regions of 100x100 pixels (6.2 x 6.2 μm) in movies of cells expressing MRLC-GFP imaged every 10 sec at a single confocal slice focused on the adhered part of the cell cortex, see Fig. 3A. The total number of frames was 16, which was sufficiently long to observe the decay in correlations over time. Since the focus of this analysis was to quantify the dynamic parts of the cell cortex, we used the following criteria to select regions for STICS: (1) The average intensity does not change by more than 2%, since we did not want to measure correlations due to net accumulation or disassembly, see Fig. 4.6 B; (2) The region does not contain permanent fibers or other intense spots that dominate the correlations; (3) The region does not exhibit net cortical flow, since we are interested in the dynamics at the rest frame of the 6.2 x 6.2 μm cortical patch; (4) we did not include regions that lack MRLC-GFP foci. Panels in Fig. 4.5B, 4.5C and 4.6A are examples of regions used in the analysis. Because

of the presence of medial fibers in Type I cells, all regions that fulfilled the above criteria were in cell Types II and III. We grouped data from Types II and III together in the following analysis.

The panels selected for STICS analysis (such as in 4.5B, 4.5C and 4.6A) are large enough to contain MRLC-GFP foci aligned in different directions so that, on average, there is no preferred orientation. In addition, since there is no net flow, function $r(\xi, \eta, \tau)$ is peaked at the origin for all τ . To simplify the analysis we thus performed an average over the polar angle to obtain a STICS function that depends on the distance to the origin $\rho = \sqrt{\xi^2 + \eta^2}$:

$$r(\rho, \tau) = \frac{1}{2\pi\rho} \oint_{\rho} r(\xi, \eta, \tau) dl. \quad (4.2)$$

Fig. 4.6C shows $r(\rho, \tau)$ for the region in Fig. 4.6A, after removing the sharp peak at $r(0,0)$ due to white noise correlations [174] (see Materials and Methods). We observe that spatial correlations extend to distances longer than the microscope's resolution (about 0.2 μm) and persist at long times: the FWHM, defined here as twice the distance ρ at which $r(\rho/2, \tau) = r(0, \tau)/2$, is 0.65 μm at $\tau = 0$. This is consistent with the organization of myosin-II into bipolar minifilaments of size 0.8-1 μm [169, 177-180] and the alignment of these filaments along short fibers.

The function $r(\rho, \tau)$ decreases with increasing τ for a given ρ , which reflects loss of correlation due to myosin assembly and disassembly at the cortex as well as movement due to local contractions. Fig. 4.6D shows that the decay of $r(0, \tau)$ can be fitted by a single exponential with decay time $\tau_{control}$ (Note: in the fit we exclude $r(0,0)$ which is determined by extrapolation, see Materials and Methods. Since $r(0,0)$ is less accurate compared to $r(0, \tau)$ for $\tau > 0$, it leads to noisy curves when used as the initial condition to normalize and compare different decay curves). We find that the average decay time is $\tau_{control} = 130 \pm 50$ sec ($n=21$), see Fig. 4.6E. This decay time reflects both the contraction of MRLC-GFP foci and their turnover. Both processes

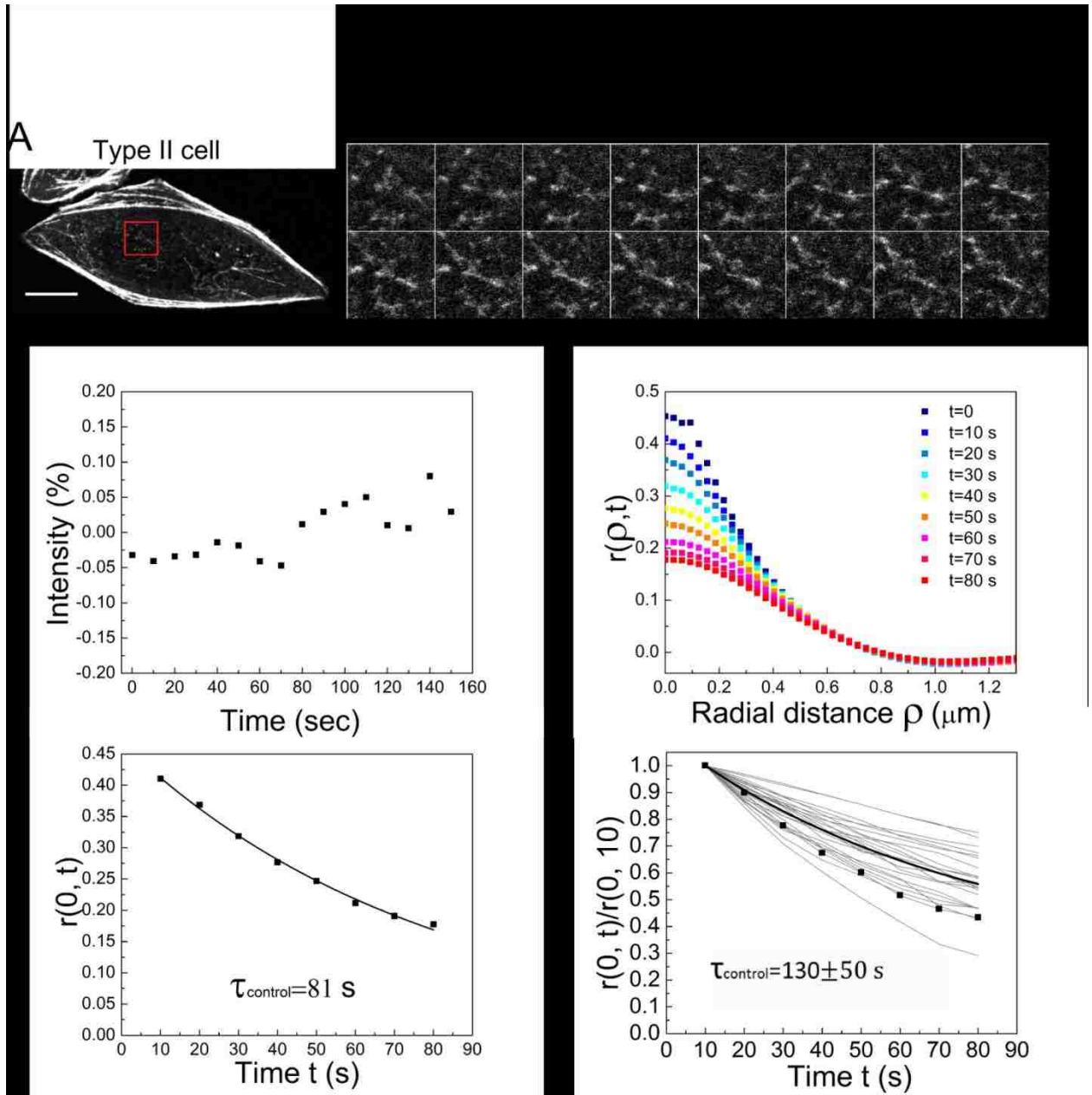


Figure 4.6. STICS analysis of MRLC-GFP dynamics in control cells at a single confocal slice at cell bottom. (A) Montage picture (right) of selected region in the middle of a Type II HeLa cell (left). Bars: $10 \mu\text{m}$ (left) and $5 \mu\text{m}$ (right). For analysis of steady state dynamics we selected regions of size 100×100 pixels ($1 \text{ pixel} = 0.6 \mu\text{m}$) that lack stable fibers over 160 sec and do not change in average intensity by more than 2%. (B) Percent change of intensity of selected region over time shows fluctuations within 0.05% of the average intensity. (C) Radially-averaged spatial-temporal image correlation function of selected region as function of radial distance ρ and delay time. (D) Single exponential fit of the correlation function of panel C at $\rho = 0$ gives a characteristic decay time $\tau = 81$ sec. (E) Normalized decay curves (at $\rho = 0$) in different control cells. The average decay time of individual exponential fits gives $\tau_{\text{control}} = 130 \pm 50$ (Mean \pm StDev, $n = 25$).

contribute to comparable amounts since the time for foci movement over a distance of order their size is comparable to their lifetime, see Fig. 4.5D.

To further probe how and contraction, turnover contribute to cortical actomyosin organization we repeated the same analysis for cells treated with blebbistatin.

4.5 STICS analysis of cortical MRLC-GFP in adhered HeLa cells in blebbistatin

We quantified the dynamics and distribution of medial MRLC-GFP in cells treated with 100 μ M blebbistatin for 60 min, using the same method as in Fig. 4.6 by applying STICS to 6.2x6.2 μ m regions imaged every 10 sec for 160 sec, see Fig. 4.7A. The criteria for selecting regions were also unchanged. The 3D kymograph of Fig. 4.7B shows much less directed motions compared to untreated cells (Fig. 4.5D), consistent with the anticipated reduction in contractility. However individual MRLC-GFP foci continued to appear and disappear (note: in Fig. 4.7B we imaged for a shorter total interval compared to Fig. 4.4D to avoid laser-induced deactivation of blebbistatin [181, 182]. The radially-averaged STICS function $r(\rho, \tau)$ has similar shape and width to untreated cells, however the decay of correlations with time are slower, see Fig.4.7 C. An exponential fit to $r(0, \tau)$ gives a relaxation time $\tau_{bleb} = 240 \pm 90$ sec longer than that of untreated cells (see Fig. 4.7 D, E).

Similar analysis to Fig. 4.7 was performed for experiments after blebbistatin washout (cells were treated with 100 μ M blebbistatin for 60 minutes that was then washed out with regular DMEM medium for 60 minutes before imaging). An example of a cell is shown in Fig. 4.8A. Unlike cells in the presence of blebbistatin, contractile motions were now evident, see Fig. 4.8B. As a result of these motions, the decay of $r(\rho, \tau)$ in the cell of Fig. 6A occurs with decay time $\tau_{washout} = 123$ sec, which is close to the decay time of untreated cells (see Fig. 4.8D). Even after the washout however, many cells are unable to recover and the resulting average decay time is only slightly smaller when compared to Fig. 4.7: $\tau_{washout} = 220 \pm 160$ sec. The standard deviation of the decay time is larger compared to Figs. 4.6 and 4.7, reflecting a variability among cells that recovered and cells that were irreversibly damaged with blebbistatin. We observed a similar variability when inactivating blebbistatin by continuous imaging [181, 182] in the presence of

blebbistatin: in some cells we observed the reformation of a contractile network (see Fig. 4.10) but other cells had little response.

To further compare the different conditions in Figs. 4.6, 4.7 and 4.8 (control, blebbistatin, recovery from blebbistatin), we searched for correlations in STICS analysis data. We did not find significant correlation between average region intensity and decay time (Fig. 4.9A), between FWHM of $r(\rho,0)$ and decay time (Fig. 4.9B), and between $r(0,0)$ and decay time (Fig. 4.9C). The value of $r(0,0)$ is the magnitude of relative intensity fluctuations at a given frame (see Eq. (4.1)). We find that $r(0,0)$ is a bit larger in the presence of blebbistatin (Fig. 4.9C), indicating a more inhomogeneous distribution in the selected regions. We did not detect a dependence of $r(0,0)$ on average intensity (Fig. 4.9D).

In conclusion, we have demonstrated that STICS analysis on the time-lapse MRLC-GFP images provides a tool to determine the activity of myosin II in live cells. The correlation decay time increases in blebbistatin, consistent with the visual observation of reduction in contractile myosin movements.

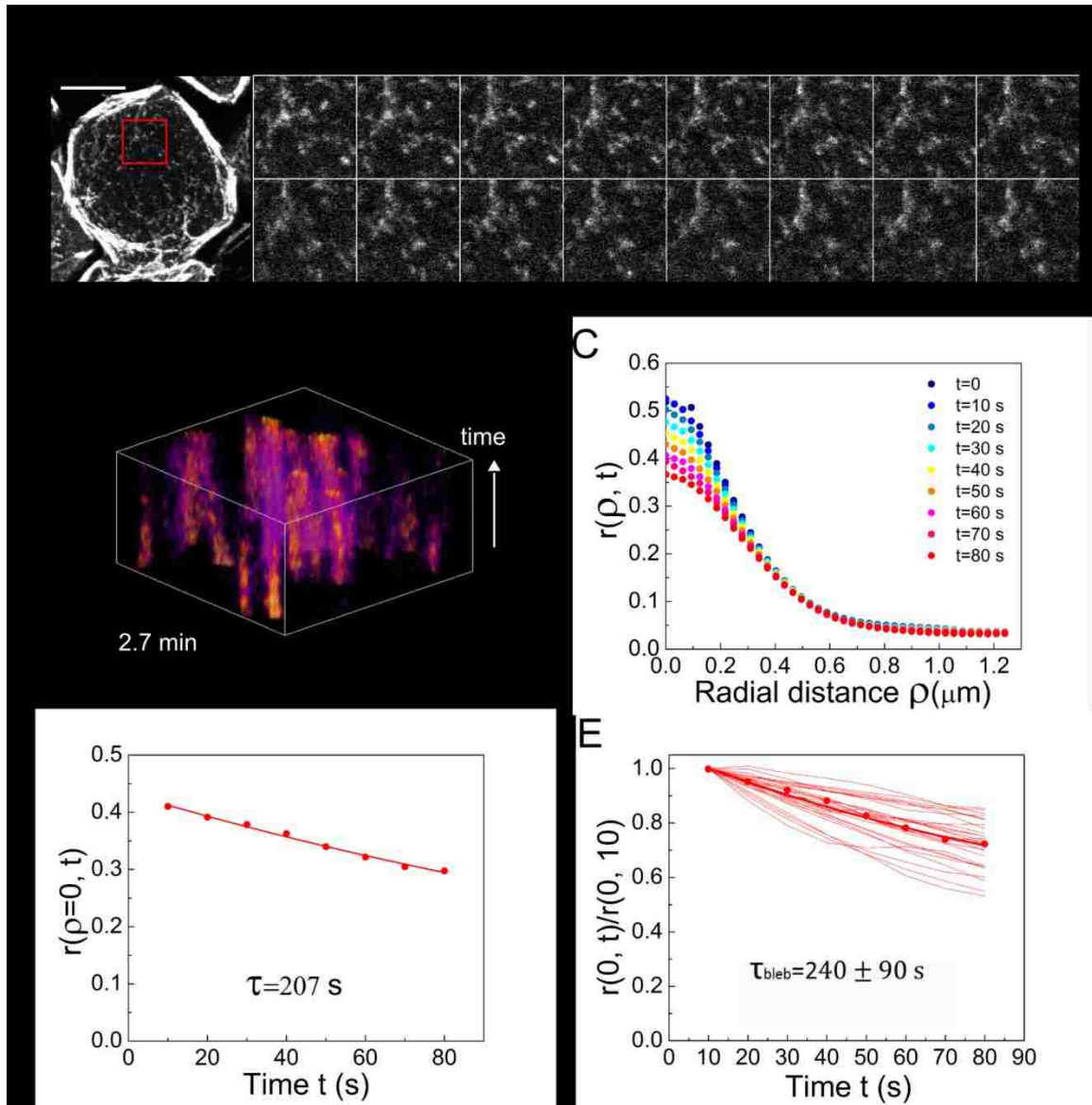


Figure 4.7 . STICS analysis of MRLC-GFP dynamics of cells treated with 100 μM blebbistatin for 60 minutes at a single confocal slice at cell bottom. (A) Montage picture (right) of selected region in the middle of a Type III HeLa cell (left). Bars: 10 μm (left) and 5 μm (right). For analysis of steady state dynamics we selected regions of size 100x100 pixels (1 pixel = 0.6 μm) that lack stable fibers over 160 sec and do not change in average intensity by more than 2%. (B) 3D kymograph of montage of panels A. Foci appearance and disappearance is observed but the near absence of diagonal features indicates less contraction compared to control cells. (C) Radially-averaged spatial-temporal image correlation function of selected region as function of radial distance ρ and delay time. (D) Single exponential fit of the correlation function of panel C at $\rho = 0$ gives a characteristic decay time $\tau = 189$ sec. (E) Normalized decay curves (at $\rho = 0$) in different blebbistatin-treated cells. The average decay time of individual exponential fits gives $\tau_{bleb} = 240 \pm 90$ sec (Mean \pm StDev, $n = 24$).

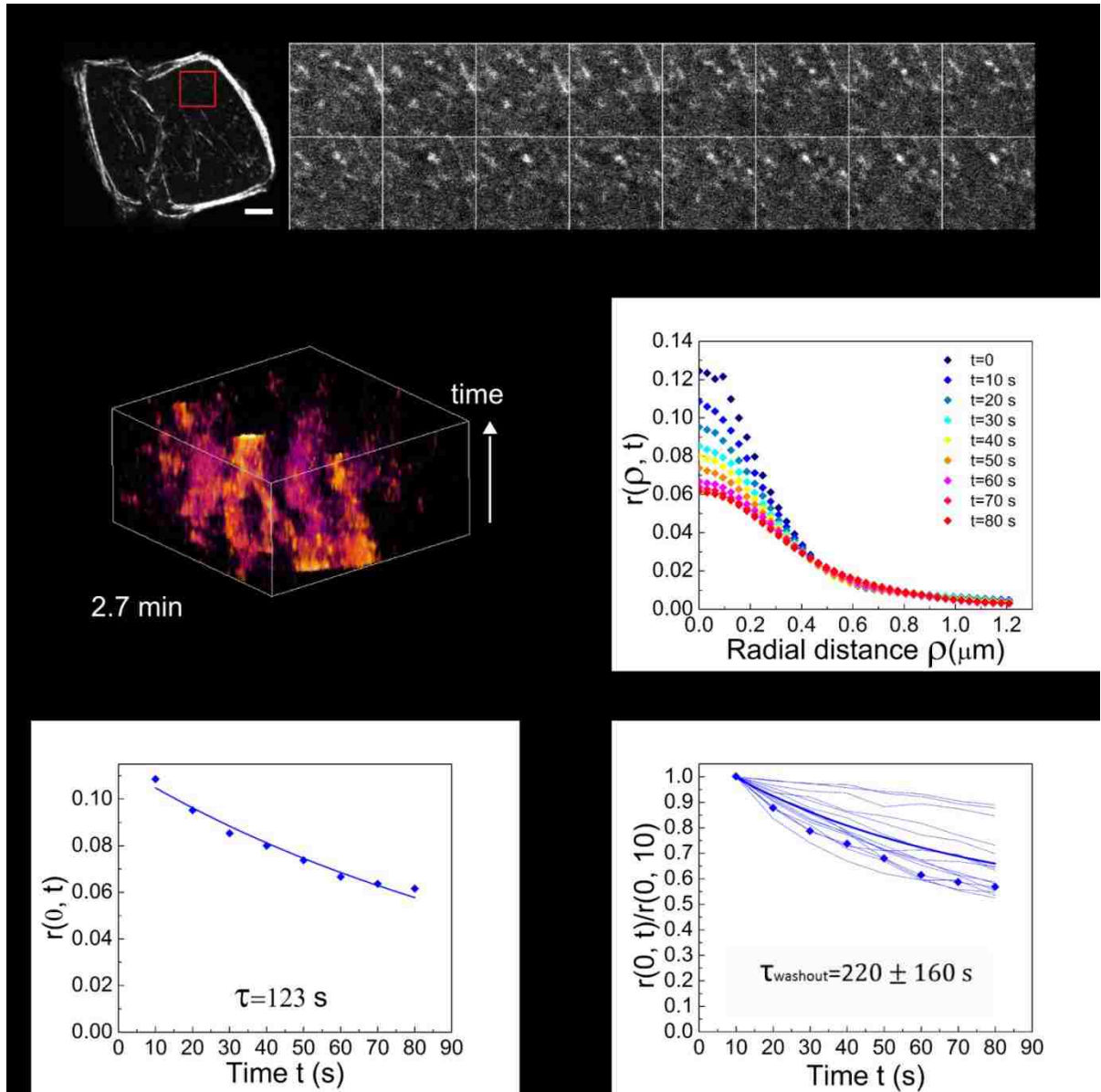


Figure 4.8 STICS analysis of MRLC-GFP dynamics of cells recovering from blebbistatin at a single confocal slice at cell bottom. Cells were treated with 100 μM blebbistatin for 60 minutes and images were taken 60 min after washout with regular DMEM medium. (A) Montage picture (right) of selected region in the middle of a Type II HeLa cell (left). Bars: 10 μm (left) and 5 μm (right). For analysis of steady state dynamics we selected regions of size 100x100 pixels (1 pixel = 0.6 μm) that lack stable fibers over 160 sec and do not change in average intensity by more than 2%. (B) 3D kymograph of montage of panel A. Foci appearance and disappearance as well as diagonal features indicating contraction are observed. (C) Radially-averaged spatial-temporal image correlation function of selected region as function of radial distance ρ and delay time. (D) Single exponential fit of the correlation function of panel C at $\rho = 0$ gives a characteristic decay time $\tau = 110$ sec. (E) Normalized decay curves (at $\rho = 0$) in different blebbistatin-treated cells. The average decay time of individual exponential fits gives $\tau_{\text{washout}} = 220 \pm 160$ (Mean \pm StDev, $n = 23$).

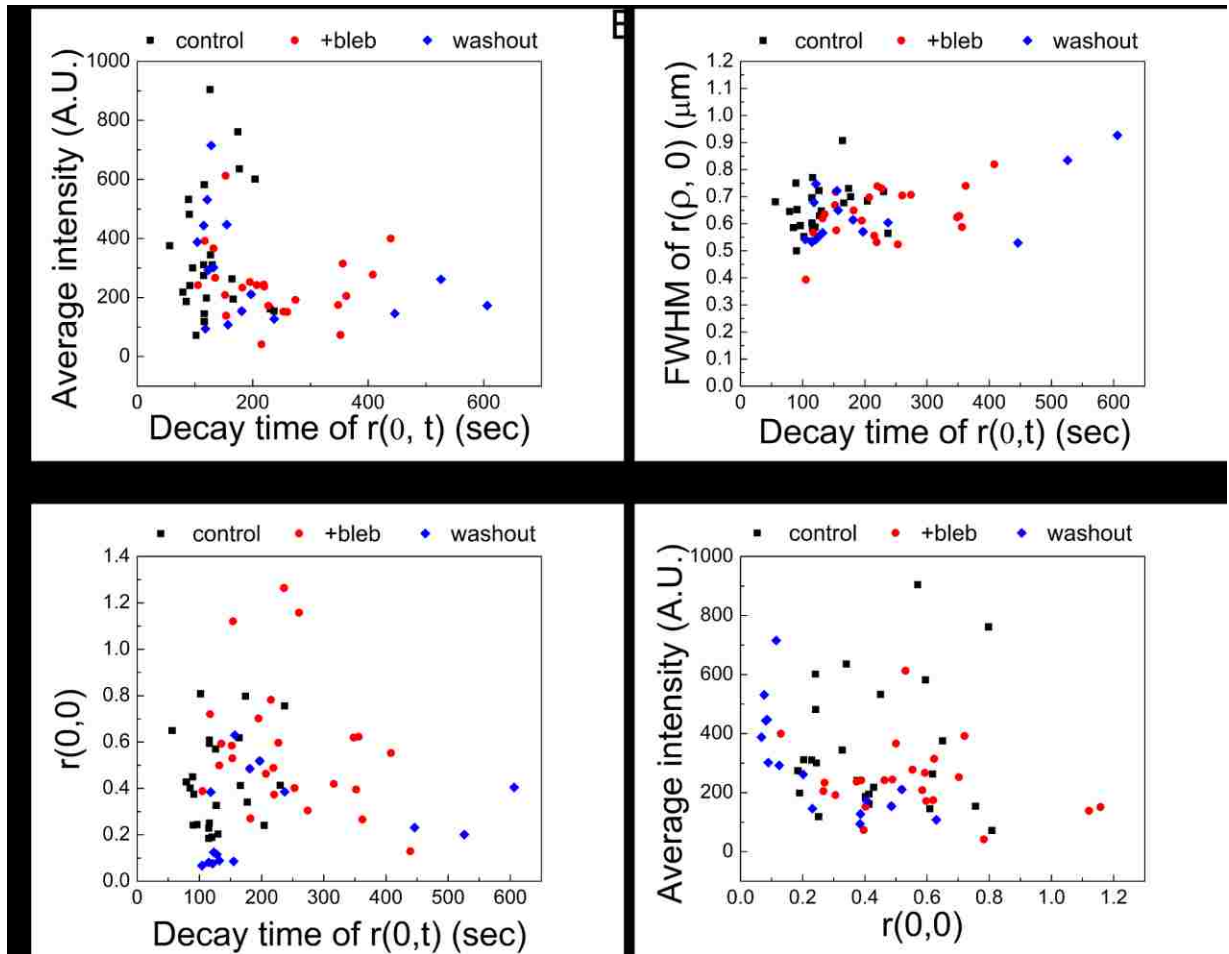


Figure 4.9 Comparison of analysis of cell images of control, blebbistatin-treated cells, and cells recovering from blebbistatin in regions of 100 by 100 pixels as in Fig. 4.6, 4.7 and 4.8. (A) Plot showing relationship between average intensity after out-of-cell background subtraction and decay time τ . The two quantities are not strongly correlated. While the correlation time increases in blebbistatin, the average intensity does not change noticeably. (B) Plot showing relationship between the FWHM of $r(\rho,0)$ (a measure of the size of the correlated region) and decay time τ . While the decay time increases in blebbistatin, the average value of FWHM does not change noticeably. (C) Plot showing relationship between the value of $r(0,0)$ (a measure of relative intensity fluctuations) and decay time τ . Cells in blebbistatin have both larger decay time τ and a more inhomogeneous intensity distribution. (D) Plot showing relationship between the value of $r(0,0)$ and average intensity shows that relative fluctuations increase as the average intensity decreases.

4.6 Summary and discussion

We quantified the dynamics and distribution of medial MRLC-GFP in HeLa cells under control state, with blebbistatin treatment for 60 min, and recovery from blebbistatin treatment in DMEM medium for 60 min. We observed the medial cortical fiber formation from myosin foci assembly and disassembly, alignment, and stabilization of linear elements (likely in the form of minifilaments) at the cortex. The 3D kymograph of Fig. 4.7D shows much less directed motions of myosin foci in cells with blebbistatin treatment compared to untreated cells (Fig. 4.5D), which is consistent with the reduction of contractility due to inhibiting the activity of myosin II by blebbistatin. However individual MRLC-GFP foci continued to appear and disappear, see Fig. 4.7D and Fig. 4.8B. The relaxation time of STICS function $r(0, \tau)$ in blebbistatin treated cells is much longer than in untreated cells ($\tau_{control} = 130 \pm 50 \text{ sec}$, $\tau_{bleb} = 240 \pm 90 \text{ sec}$), which suggests that the relaxation time of $r(0, \tau)$ is determined by directed motion of myosin foci and their turnover of appearance and disappearance at the cortex. The FWHM of $r(0, \tau)$ remains unchanged ($0.65 \mu\text{m}$) before and after blebbistatin treatment. The STICS analysis of cells recovery from blebbistatin treatment shows slightly reduction of the relaxation time of $r(0, \tau)$ ($\tau_{washout} = 220 \pm 160 \text{ sec}$) compared to cells in blebbistatin, however, the standard deviation is large. Fig 4.8B shows in some cells the directed motions of myosin foci were recovered after washing out blebbistatin.

In conclusion, time-lapse MRLC-GFP images reveal the process of myosin foci contraction, alignment and stabilization during the formation of medial fibers at the cortex, as well as their appearance and disappearance turnover. We have demonstrated that STICS analysis on the time-lapse MRLC-GFP images to be a tool to determine the activity of myosin II at the medial cortex of live cells. The relaxation time of STICS function $r(0, \tau)$ increases in blebbistatin due to the reduction of contractile movement of myosin foci. We will use the same method in the next chapter to quantify simulations of fiber assembly and disassembly.

Chapter 5

Model of cortical myosin II dynamics and fiber formation

5.1 2D mechanical model: introduction

The results of the previous chapter suggest that the medial actomyosin cortex exists in a homeostatic state of assembly, reorganization and disassembly. We observed myosin foci appear and disappear over time, in a process that likely depends on myosin minifilament formation by nucleation and growth [155] and myosin binding to actin filaments and proteins on the cell membrane. The cortical foci contract towards one another and align. This process is likely to occur by myosin pulling on actin filaments located at the cell cortex, which tend to form bundles with myosin minifilaments and actin cross-linking proteins [183]. Formation of stable linear fibers depends on myosin motor activity and is positively correlated to presence of contraction, implying that the stability of myosin minifilaments in the cortex increases with tension, as also suggested by prior experiments [155, 160, 164]. When coupled to adhesion formation, long fibers can thus develop along the cortex by maintaining tension through anchors at focal adhesions.

We developed a coarse-grained computational model to test the extent to which the above mechanisms can explain our experimental observations. In this model the basic units are bipolar myosin minifilaments that can move and change orientation on a 2D plane representing the cell cortex (see Fig. 5.1). They interact via the following four types of forces and torques they exert on one another.

5.2 Model of myosin minifilament turnover and alignment

5.2.1. Contractile force

As Fig. 5.1A shows, the contractile force between minifilaments is mediated by actin filaments in the vicinity of the minifilaments (actin filaments are not explicitly included). The direction of this attractive force between minifilaments i and j is along the axis joining their centers and has magnitude

$$F_c^{ij} = k_c (L_{\min} - s) \exp(-|\theta_{ij}| / \theta_c^0), \quad (L_{\min} < s < L_{\max}) \quad (5.1)$$

when the distance between the minifilament centers s is between L_{\min} and L_{\max} and zero otherwise. Here k_c , L_{\min} , L_{\max} and θ_c^0 are model parameters and $\theta_{ij} = \theta_1 + \theta_2$, where θ_1 and θ_2 are the angles between axis of each minifilament and the line joining their centers, as shown in Fig. 5.1A. The exponential dependence in Eq. (5.1) simulates an increase in contractile force when filaments align, representing the cooperative nature of myosin-actin alignment. After scanning values of θ_c^0 in the simulations, we chose $\theta_c^0 = 0.3 (17.2^\circ)$, which resulted in realistic myosin alignment.

Parameters L_{\min} and L_{\max} are determined based on the length scale of myosin minifilament and actin filaments. In human endothelial, epithelial, and fibroblast cells, the length of myosin II minifilaments is $0.6 - 2 \mu\text{m}$ and the length of actin thin filaments is $1 - 5 \mu\text{m}$ [20, 160, 169, 177, 184]. So we chose $L_{\max} = 1.6 \mu\text{m}$ as the longest scale over which contraction occurs. When minifilaments approach one another they cannot overlap and accumulation of α -actinin in between them may limit how close they can approach one another. So we set $L_{\min} = 0.8 \mu\text{m}$ and apply a repulsive force for minifilament separation distances shorter than L_{\min} (see below). The linear functional dependence on s in Eq. (3) ensures the contractile force vanishes continuously at $s = L_{\min}$.

Parameter k_c determines the magnitude of the contractile force. For non-muscle cells, there are about 20 myosin II motors polymerized into bipolar minifilaments in stress fibers [77, 148]. Since each myosin motor produces 2-6 pN pulling force on actin filaments, a single minifilament could produce a pulling force ~ 40 pN, after considering the disordered nature of the actin network and the small duty ratio of myosin II heads [185]. Thus we estimate $k_c = 50 \text{ pN}/\mu\text{m}$.

As minifilaments start to aggregate in the simulations, they can exert larger forces as they interact with more neighbors. To represent an upper physical limit to the magnitude of contractile forces, we introduced an upper limit of 50 pN per minifilament. For all minifilaments for which the total contractile force exceeds the upper limit, we reduce the force corresponding to every pair by the factor that reduces the

total force to the maximal value. After performing this operation for all minifilaments, we then re-calculate the average force between pair i and j to be $(F_c^{ij} + F_c^{ji}) / 2$.

5.2.2. Aligning force and torque

Aligning force and torque (Fig. 5.1B) are responsible for minifilament alignment and rotation. Since this effect likely occurs via actin filaments in between minifilaments, we apply these forces and torques when $s \leq L_{\max}$. Following [186], aligning forces act on the centers of minifilaments, perpendicular to the line that joins their centers, see minifilaments i and j . The force on i that acts along the direction that decreases the magnitude of angle θ_1 defined in Fig. 5.1B. The unit vector along this direction is \mathbf{e}_\perp^1 , and similarly for j that has angle θ_2 . To satisfy force balance, we assume a force of equal magnitude but of opposite direction acting on the neighbor. We used the following expression for the force on minifilament i due to minifilament j :

$$\mathbf{F}_{al}^{ij} = F_{al} \left[\frac{\sin(\theta_1)}{C_{\max}} e^{-|\theta_1|/\theta_{al}^0} \right] \mathbf{e}_\perp^1 - F_{al} \left[\frac{\sin(\theta_2)}{C_{\max}} e^{-|\theta_2|/\theta_{al}^0} \right] \mathbf{e}_\perp^2 \quad (s < L_{\max}) \quad (5.2)$$

Parameter F_{al} determines the magnitude of the aligning force. Here $C_{\max} = 0.0731$ is a normalization constant equal to the maximum value of the function $\sin(\theta)e^{-|\theta|/\theta_{al}^0}$ [186]. The cutoff angle $\theta_{al}^0 = 0.2$ (11.5°), represents that the magnitude of the aligning force and torque is reduced by a factor less than unity for angles larger than θ_{al}^0 . A maximum aligning force of 30 pN was implemented as for the upper limit in the contractile force.

A torque was introduced to rotate neighboring minifilaments along a common direction. The torque on minifilament i due to minifilament j :

$$\tau_{rot}^{ij} = \tau_0 \left[\frac{\sin(\theta_1)}{C_{\max}} e^{-|\theta_1|/\theta_{al}^0} \right] - \frac{\tau_0}{C_{\max}} \left[\frac{\sin(\theta_2)}{C_{\max}} e^{-|\theta_2|/\theta_{al}^0} \right] \quad (s < L_{\max}) \quad (5.3)$$

where τ_0 is a constant representing the amplitude of the torque. Eq. (5.3) satisfies torque balance,

$$\tau_{rot}^{ij} = -\tau_{rot}^{ji}.$$

5.2.3. Short range repulsion

Short range repulsion between minifilaments (see Fig. 5.1C) prevents minifilaments from fully overlapping with one another:

$$F_{repel}^{ij} = k_r (L_{\min} - s) \quad (s < L_{\min}) \quad (5.4)$$

We used $k_r = 50 \text{ pN} / \mu\text{m}$, which is large enough to counteract contractile forces. These forces are oriented along the line joining the centers of the minifilaments.

5.2.4 Stress-dependent minifilament dissociation

To simulate the dissociation of foci, we assumed that the life time of each minifilament is reduced by contractile forces:

$$k_d = k_{d0} \exp\left(-|F_c^i| / F_d^0\right) \quad (5.5)$$

where k_{d0} is the dissociation rate of non-interacting minifilaments, $|F_c^i|$ is the magnitude of the total contractile force experienced by the minifilament, and $F_d^0 = 15 \text{ pN}$ defines a force scale over above which stress-stabilization occurs. When a minifilament dissociates from its current position, we place it at another random position and random orientation in the simulated cortical region, thus keeping the total concentration constant. A value $k_{d0} = 0.001 \text{ s}^{-1}$ gave agreement with experimental results, see below.

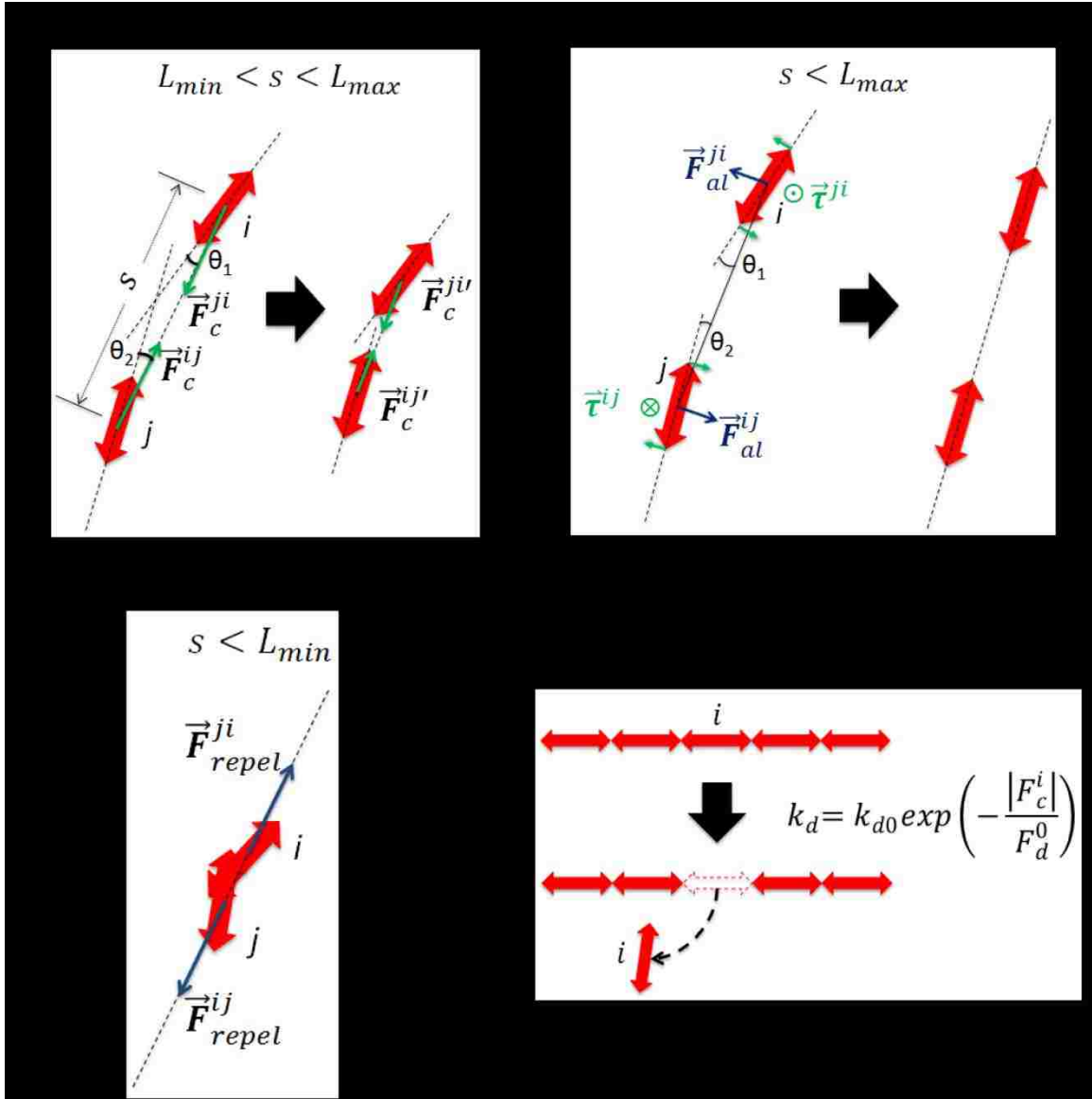


Figure 5.1 Cartoon of coarse-grained model of myosin minifilament interaction. (A) The contractile force $\vec{F}_c^{ij} = -\vec{F}_c^{ji}$ between two minifilaments i and j is determined by angles θ_1, θ_2 , and d , and is applied when $L_{\min} < d < L_{\max}$. The contractile force increases with decreasing $|\theta_1|, |\theta_2|$ and decreasing d . The contractile force is assumed to be mediated by actin filaments that are not explicitly included in the model. (B) Minifilaments experience torques $\vec{\tau}^{ij} = -\vec{\tau}^{ji}$ that rotate them to point toward each other when $d < L_{\max}$. Aligning forces $\vec{F}_{al}^{ij} = -\vec{F}_{al}^{ji}$ act on the center of each minifilament, perpendicularly to the line joining their centers. These torques and forces are also assumed to be mediated by actin filaments as in panel A. (C) Excluded-volume short-range repelling forces $\vec{F}_{repel}^{ij} = -\vec{F}_{repel}^{ji}$ are applied when $d < L_{\max}$. (D) The disassociation rate for each minifilament decreases exponentially with increasing total contractile force acted on the minifilament. This results in stabilization of linear structures that bear tension. Dissociated minifilaments are placed at a random position on the plane simulating the cell cortex to maintain constant overall minifilament concentration.

Table 5.1. Parameter values used in simulations. For justification see main text unless otherwise indicated.

Parameters	Unit	Control	+blebbistatin
Length in x(y)	[μm]	8	8
dt	[s]	0.01	0.01
k_r	[pN/ μm]	50	50
k_c	[pN/ μm]	50	5
F_{al}	pN	6 ^a	0.6
F_d^0	pN	15	15
L_{\max}	[μm]	1.6	1.6
L_{\min}	[μm]	0.8	0.8
θ_c^0	[rad]	0.3	0.3
θ_{al}^0	[rad]	0.2	0.2
k_{d0}	[1/s]	0.001	0.001
ζ	[pN·s/ μm]	400 ^b	400 ^b
τ_0 / ζ_{rot}	[pN·s/ μm]	400 ^c	400 ^c

a: Estimated to be comparable to contraction force.

b: Value that gives minifilament speeds similar to those in experiments

c: Estimated to give a minifilament rotational speed similar to translational speed.

At each time step ($dt = 0.01$ sec) of our Monte Carlo simulation we calculate the total force \mathbf{F}_{tot}^i for each minifilament i , and update the positions \mathbf{x}_i according to $\mathbf{x}_i(t + dt) = \mathbf{x}_i(t) + (\mathbf{F}_{tot}^i / \zeta) dt$. The value of the drag coefficient of the cortex is $\zeta = 400$ pN s/ μm that gives velocities that match those in experiments. The orientation ϕ_i of each minifilament is updated according to $\phi_i(t + dt) = \phi_i(t) + (\tau_{rot}^i / \zeta_{rot}) dt$, where τ_{rot}^i is the total torque experienced by minifilament i and ζ_{rot} is the total rotational drag coefficient. The single independent parameter describing the rate of orientation change is τ_0 / ζ_{rot} . The parameters used in the simulations are summarized in Table 5.1.

5.3 Simulation results

To check if the model of the previous section reproduces basic features of the dynamics in the medial cortex, we run simulations in an $8 \times 8 \mu\text{m}^2$ region containing two focal adhesions (green spots in Fig. 5.2 A and B) at the two corners. (The simulated density of focal adhesions is roughly the density in Type I and II control cells, 1.4 ± 1.1 , 3.9 ± 2.4 per $100 \mu\text{m}^2$, respectively). The focal adhesions were simulated as 20 static minifilaments oriented in the same direction, representing the myosin minifilaments that would form at a fiber around the adhesion. While focal adhesions are also dynamic and their growth depends on tension [20, 160, 167, 168] (Fig. 4.2), here we are interested in myosin dynamics and thus assumed the adhesions were fixed. In the simulations the interaction between cortical minifilaments and those in focal adhesions is the same as the interaction between minifilaments, except that that the latter do not move during each simulating steps.

To calculate the number of minifilaments to include, we measured the intensity of MRLC-GFP foci in experimental images and the mean intensity at medial regions of the cell cortex to estimate $N = 40 \pm 20$ in an $8 \times 8 \mu\text{m}^2$ region for control Type I cells. Fig. 5.2E shows a simulation starting with $N = 42$ randomly placed minifilaments. At the beginning of the simulation the minifilaments locally align and contract and build a tension-stabilized fiber at ~ 3000 s in between the focal adhesions, similar to what was observed in control cells with actomyosin bundles (Fig. 4.5A). This bundle is stable for ~ 1000 s when it

breaks and starts to contract and disassembles in 300 sec, similar to experiments (see Movie S1 where fibers can be seen to form and disassemble within ~500 s).

Type II cells have slightly less MRLC-GFP intensity and higher concentration of focal adhesions in the medial regions (Figs. 4.3). If we just decrease the number of myosin minifilaments in the simulations to $N=37$ (see Fig. 5.3A) we no longer obtain stable fibers in between the focal adhesions placed at the two corners. Thus a stable fiber network would require a higher density of focal adhesions, as observed in Type II cells. The third simulation in Fig. 5.4A shows that the model reproduces a transient network structure observed in Type III cells that have very few medial focal adhesions

The simulations of Fig. 5.2-5.4 also reproduce the correlation pattern quantified by STICS analysis in experiments. We checked this by performing radially-averaged STICS analysis on simulated images in which the shape of the minifilaments was a rectangle with dimensions $0.8 \times 0.2 \mu\text{m}$. Panel C in Fig. 5.2-5.4 show STICS analysis in simulations of cells that are of Type I, II, and III, respectively. Similar to the analysis of the experiments in Fig. 4.6, we selected regions of size $5.6 \times 5.6 \mu\text{m}^2$ that excluded permanent fibers (see red boxes in Fig. 5.2B-5.4B). We found that the STICS curves in the simulations of panel C in Fig. 5.2-5.4 have similar shape to those of Fig. 4.6C. The average decay time of $r(\rho, 0)$ is of order 100 sec in all three cases, similar to Fig. 4.6E. Both contractile motions and minifilaments turnover contribute to establishing this relaxation time.

Finally, we checked to see if our proposed mechanism is consistent with the behavior of cells in blebbistatin. In Fig. 5.5 we simulated the effect of blebbistatin as a reduction in the contractile and aligning forces. The number of minifilaments included in these simulations was $N = 40$, similar to Fig. 5.2-5.4, since blebbistatin does not significantly change the MRLC-GFP intensity in regions of the medial cell cortex that do not contain permanent fibers (Fig. 4.3).

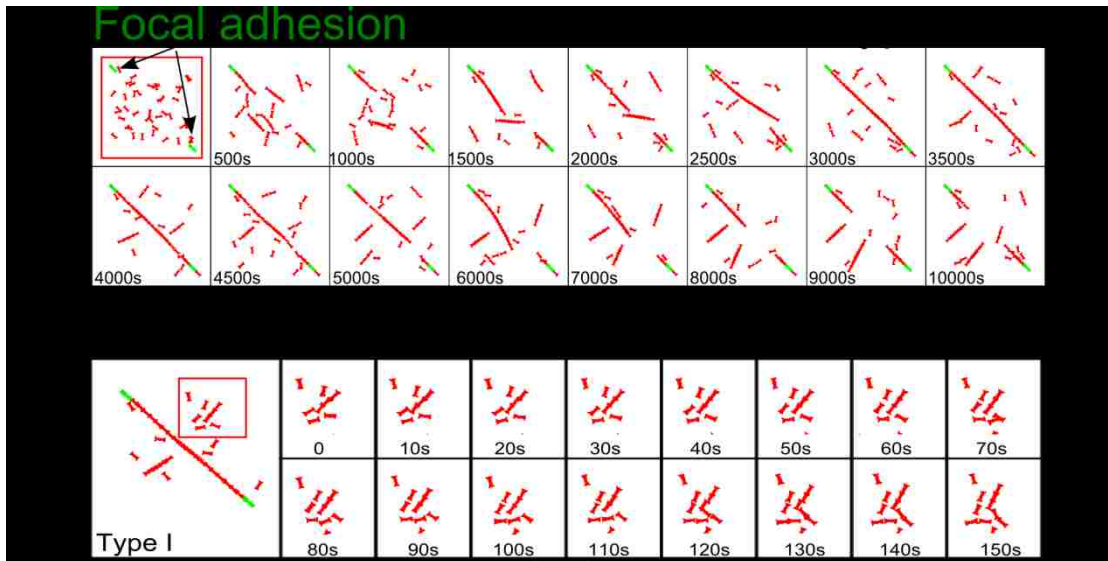


Figure 5.2 Simulation of type I cells with STICS analysis of the simulation results. (A) A snapshot of a simulation of type I cell with $n_{FA} = 2$ focal adhesions (green) and $n_{myo} = 42$ minifilaments (red) in a $8 \times 8 \mu\text{m}^2$ region indicated by red frame ($k_c = 50 \text{ pN}/\mu\text{m}$, $f_{at} = 6 \text{ pN}$). (B) A snapshot of ROI starts from 4200 sec in simulation time. The ROI is 100×100 , indicated by a red box. (C) Plot of STICS functions obtained in (B) with time lag $dt = 10 - 150 \text{ sec}$. (D) Plots of normalized function of $r(0, \tau)$ vs. τ with mean \pm StDev., fitted by exponential function $y = y_0 e^{-\frac{t}{\tau_0}}$, $\tau_0 = 105 \pm 23 \text{ sec}$, which is within the range of experimental data of $\tau_0 = 130 \pm 50 \text{ sec}$ ($n=10$).

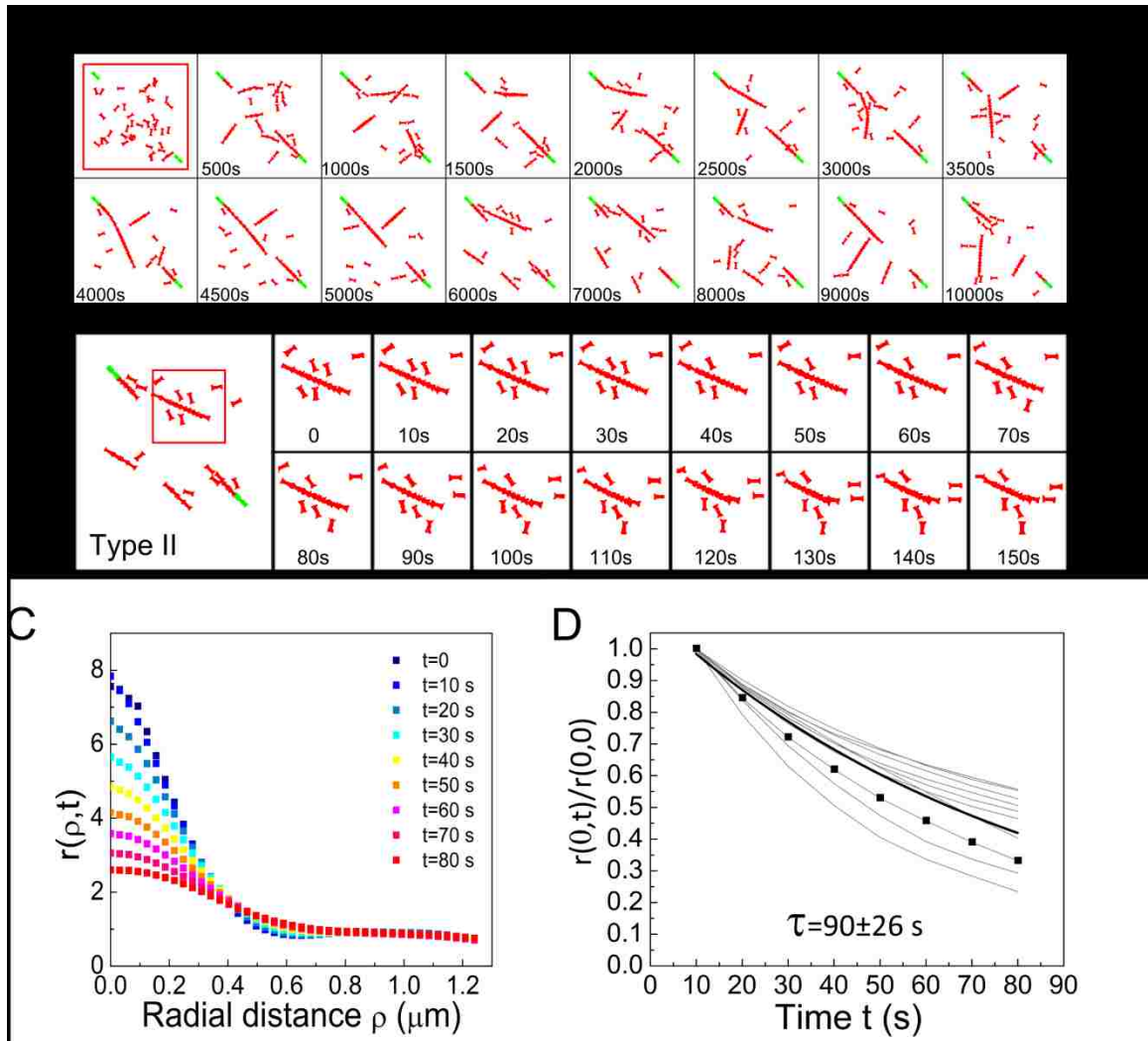


Figure 5.3 Simulation of Type II cells with STICS analysis of the simulation results. (A) A snapshot of a simulation of Type II cell with $n_{FA} = 2$ focal adhesions (green) and $n_{myo} = 37$ minifilaments (red) in a $8 \times 8 \mu\text{m}^2$ region indicated by red frame ($k_c = 50$ pN/ μm , $f_{al} = 6$ pN). (B) A snapshot of ROI starts from 4200 sec in simulation time. The ROI is 100×100 pixels. (C) Plot of STICS functions obtained in (B) with time lag $dt = 10 - 150$ sec. (D) Plots of normalized function of $r(0, \tau)$ vs. τ with mean \pm StDev., fitted by an exponential function, $\tau_0 = 90 \pm 26$ sec. ($n=10$)

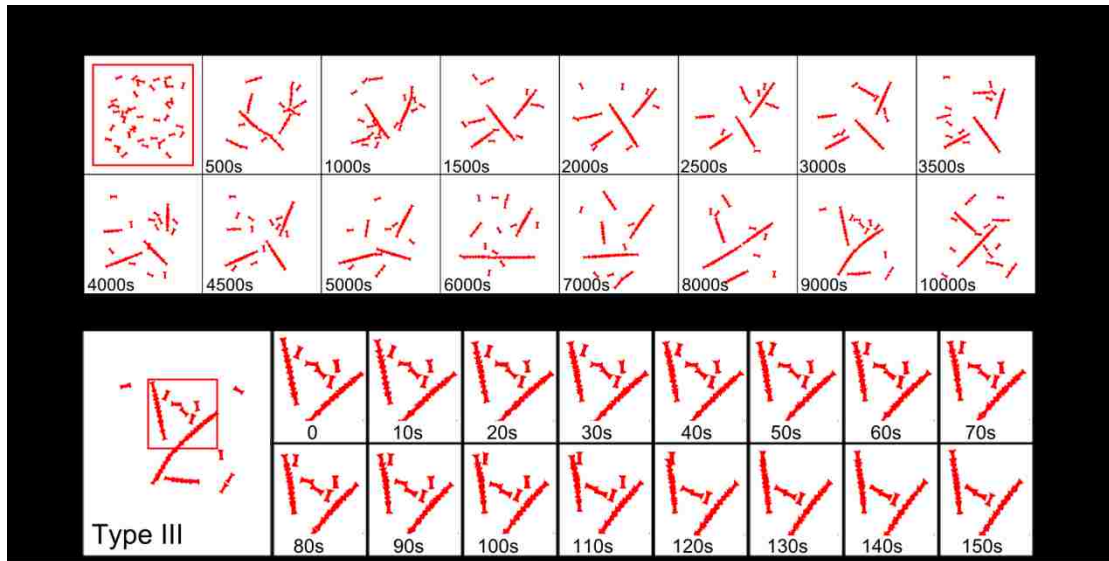


Figure 5.4 Simulation of Type III cells with STICS analysis of the simulation results. (A) A snapshot of a simulation of Type III cell without focal adhesions (green) and $n_{myo} = 42$ minifilaments (red) in a $8 \times 8 \mu\text{m}^2$ region indicated by red frame ($k_c = 50 \text{ pN}/\mu\text{m}$, $f_{al} = 6 \text{ pN}$). (B) A snapshot of ROI starts from 4200 sec in simulation time. The ROI is 100×100 pixels. (C) Plot of STICS functions obtained in (B) with time lag $dt = 10 - 150 \text{ sec}$. (D) Plots of normalized function of $r(0, \tau)$ vs. dt with mean \pm StDev., fitted by an exponential function, $\tau_0 = 92 \pm 25 \text{ sec}$ ($n=10$).

By reducing the contractile force by a factor of ten (reducing k_c to 5.0 pN/ μm and F_{al} to 0.6 pN) we find that minifilaments cannot assemble into long fibers. This happens with or without including focal adhesions in the simulations (Fig. 5.5 A, C). Short fibers were still observed in the middle of simulated cortex; however, these fibers had a short lifetime and disassembled before they could elongate to bridge focal adhesions, maintain tension and stabilize. The reduction of the magnitude of contractile and aligning forces results in a reduction of the motion of the minifilaments. The decay time of the STICS $r(\rho,0)$ in Fig. 5.5B, D is now 210-230 sec, which is about twice longer compared to Fig. 5.2-5.4 because it is mostly determined by the turnover kinetics that occurs over a time $k_{d0}^{-1} = 10^3$ sec rather than contraction and alignment. This increase in the decay time is consistent with the results of Fig. 4.7.

In the simulations of the effect of blebbistatin in Fig. 5.5 we kept the parameters of minifilament turnover kinetics k_{d0} and F_d^0 in Eq. (7) unchanged compared to Fig. 7. While minifilament turnover still occurs in the presence of blebbistatin (Fig. 4.7B), it is difficult to accurately estimate the influence of blebbistatin on the minifilament turnover kinetics as a function of contractile force. For simplicity, we kept the turnover kinetics unchanged to show that the simulated reduction in contraction in Fig. 5.5 is enough to reproduce the experimental trend in the presence of blebbistatin. Finally, we note that the FWHM of $r(\rho,0)$ in Figs. 5.2-5.5 is somewhat smaller than in the experiments of Fig. 4.6, 4.7 and 4.8 because the simulated minifilaments were drawn as $0.8 \times 0.2 \mu\text{m}^2$ rectangles, which did not include the effect of the microscope's PSF broadening.

Table 5.2. Comparison of the simulation results.

	Cell type/condition	Decay time of $r(\rho,0)$ (sec)	FWHM of $r(\rho,0)$ (μm)
Experiment	Control	130 ± 50	0.66 ± 0.09
	+Blebbistatin	240 ± 90	0.63 ± 0.09
	Washout	220 ± 160	0.64 ± 0.12
Simulation	Type I (control)	105 ± 23	0.49 ± 0.05
	Type II (control)	89 ± 26	0.49 ± 0.04
	Type III (control)	92 ± 25	0.50 ± 0.03
	Type II (+blebbistatin)	210 ± 40	0.49
	Type III (+blebbistatin)	230 ± 50	0.49

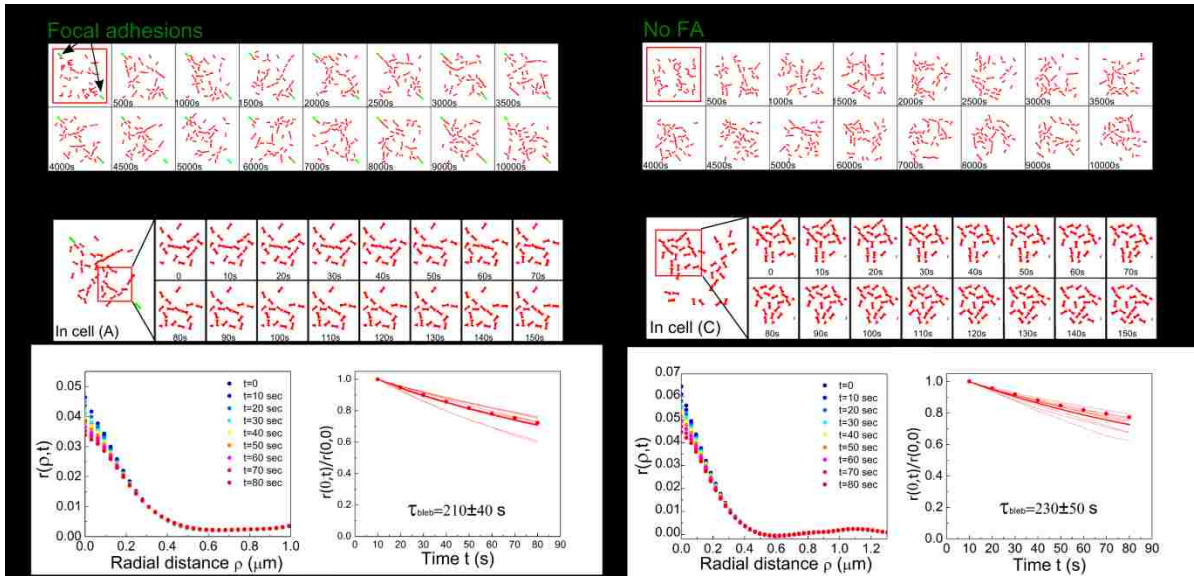


Figure 5.5. 2D simulation of actomyosin network in type II and type III cells (A: with focal adhesions. B: without focal adhesion.) treated with blebbistatin by decreasing the contractile force and aligning force by 90% ($k_c=5.0$ pN/ μm , $f_{al}=0.6$ pN) of control cells. In both (A) and (B), there was no bundle formed and no contractile activity between minifilaments. (C,D) STICS analysis on the simulated type II and III cells treated with blebbistatin demonstrates that STICS decay time increases ($\tau = 210 \pm 40$ sec in type II cell and $\tau = 230 \pm 50$ sec in type III cell) in blebbistatin treated cells due to the inhibition of myosin II, which is close to the STICS analysis results in experimental data (see Fig.4.7). The data was shown as the format of mean \pm StDev. ($n=10$).

5.4 Discussion and further work

Based on previous study and our experimental results (Chapter 4), we used a 2D mechanical model to simulate the interactions between myosin minifilaments and appearance/disappearance from the cortical plane. The simulations replicate the processes of myosin II minifilament contraction, break and disassembly, appearance and disappearance on the cortex of HeLa cells. By adjusting the number density of myosin minifilaments and focal adhesions, one can obtain Type I, II and III cells. The parameters for the simulation of Type I control cells are listed in table 5.1. The simulation of type II cells were obtained by reducing the number of myosin minifilament by 10%. Compared to Type I cells, the transient fibers are unstable and subject to disassembly in a short time because there are less minifilaments that can be assembled into fibers to keep the tension. For Type III cells without focal adhesions, short fibers were assembled for a short period of time in simulations. However, the fibers were unstable because there was no anchor for them to maintain high tension. Longer fibers were assembled occasionally, but they were more unstable compared to Type II cells (see Fig. 5.3 & 5.4). To simulate cells treated with blebbistatin, we reduced the contractile and aligning force between minifilaments by 90% from the control cells. In the simulations of Type II and III cells there was rarely contraction and alignment between minifilaments while appearance and disappearance persists. This resembles the time-lapse MRLC-GFP images of blebbistatin treated cells in Chapter 4.

STICS analysis of the simulated cell suggests that the activity of myosin minifilaments (appearance and disappearance; contraction and alignment) determines the decay time of $r(0, \tau)$, which is $105 \pm 23 \text{ sec}$, $89 \pm 26 \text{ sec}$, and $92 \pm 25 \text{ sec}$ for Type I, II and III cells, respectively. The decay time of $r(0, \tau)$ is close to, but somewhat smaller than the value from experimental data of control cells ($\tau_{control} = 130 \pm 50 \text{ sec}$). This difference could be improved by adjusting the magnitude of effective elastic spring constant k_c , the magnitude of aligning force F_{al} , and the disappearing rate k_{d0} in simulations. The decay time of $r(0, \tau)$ for simulated cells in blebbistatin is $210 \pm 40 \text{ sec}$ and $230 \pm 50 \text{ sec}$ for Type II and Type III cells, respectively, which is close to the time obtained from the

experimental data of blebbistatin treated cells ($\tau_{bleb} = 240 \pm 90 \text{ sec}$). Time-lapse images of both control cells and blebbistatin treated cells show the appearing and disappearing process in the ROI for STICS analysis. The only difference is that the fiber reorganization in control cells is faster than in the blebbistatin treated cells due to the interaction between myosin minifilaments. This suggests that the decay time of $r(0, \tau)$ can be used to determine the activity of myosin II in cells.

The simulations also demonstrate that the FWHM of function $r(\rho, 0)$ is related to the length of minifilaments. In simulations, minifilaments are represented by short thin rods with the length of $0.8 \mu\text{m}$ and the width of $0.2 \mu\text{m}$, which results in a FWHM of $r(\rho, 0)$ equal to $0.49 \mu\text{m}$ for control cells and cells in blebbistatin. In the microscopic MRLC-GFP images, the myosin foci are not precisely rod-shaped, and some foci might contain multiple minifilaments, which results in large value of FWHM as $0.64 \mu\text{m}$.

The parameters θ_{al}^0 and θ_c^0 are important in determining the assembly of fibers and network in simulations. It is difficult to precisely determine θ_{al}^0 and θ_c^0 through experiments. More systematically study θ_{al}^0 and θ_c^0 in simulation is necessary to better understand the mechanism of the cortical cytoskeletal network assembly.

Our model and simulation can be used to study a variety of cortical actomyosin network assembly process. A direct application of our model is to understand why some cells have both peripheral and central stress fibers (Type I), while some have peripheral stress fibers only (Type II & III). It is well known that myosin II plays an important role in cytoskeletal network assembly and regulating the elasticity of cytoskeletal network. HeLa cells cultured on soft and stiff polyacrylamide substrates (400 Pa and 60 kPa) are very different in morphology, focal adhesions (size and number) [155], and cytoskeletal network (Type I, II and III cells) (see Fig. 4.2). Interestingly, the stem cell differentiation on soft and stiffer substrates is also regulated by the activity of myosin II [79, 187].

The mechanical properties and dynamics of stress fibers in cells adherent on elastic substrates are regulated by the activity of myosin II. Our model will shed light on understanding mechanisms of the

cellular mechanosensing and mechanotransduction, and how it is related to cortical cytoskeletal network reorganization.

Chapter 6

Conclusions and discussion

6.1 Summary and conclusions

The dynamics of cytoskeletal network is very important to cell activity such as cell migration during wound healing and cell division. In this dissertation, I demonstrated that the concentration and activity of myosin II in non-muscle cells is crucial to the actomyosin network reorganization and medial fiber assembly through confocal fluorescence microscopy and STICS analysis. The time-lapse MRLC-GFP images show that the medial actomyosin cortex exists in a homeostatic state of assembly, reorganization and disassembly. Myosin foci appear and disappear on the cortex over time, as well as contract towards one another and align. These dynamics reflect the process of myosin pulling on actin filaments located at the cell cortex, which tend to form bundles with myosin minifilaments and actin cross-linking proteins. Formation of stable linear fibers depends on myosin motor activity and is positively correlated to presence of contraction, implying that the stability of myosin minifilaments in the cortex increases with tension, as also suggested by prior experiments [97, 164, 188-190]. When coupled to adhesion formation, long fibers can thus develop along the cortex by maintaining tension through anchors at focal adhesions. Thus the stability of long medial fibers is determined by the number density of minifilament and focal adhesions. Compared to Type I cells, Type II cells have slightly less medial MRLC-GFP foci on the cortex and more focal adhesions, resulting in a medial network of short fibers as opposed to long bundles. Type III cells have even less medial MRLC-GFP foci with no focal adhesions in the middle, resulting in the absence of a network or fibers in the cell middle. The STICS analysis of the medial regions in Type I, II and III cells reveals the decay time of $r(0, \tau)$ is determined by both contraction and alignment of the foci and the turnover process of the foci (see Fig.3.3). In the cells with 100 μ M blebbistatin treatment, the motion of foci due to the contraction and alignment is suppressed. However, the turnover kinetics of foci remain (see Fig. 3.5B). The STICS analysis shows that the decay time of $r(0, \tau)$ for blebbistatin-treated cells is almost twice longer than the decay time in untreated cells because of the inhibition of myosin II.

We developed a 2D coarse grained model to simulate the medial stress fiber assembly driven by the contraction, alignment, and the turnover kinetics of myosin minifilaments in Type I, II and III cells. By tuning the number of minifilaments and focal adhesions, the simulations reproduce the dynamics of medial fibers in Type I and II cell. In Type I cells, a long medial fiber was assembled and anchored on focal adhesions and stabilized under tension. In Type II cells, long medial fibers are less likely to assemble and stabilize because of lower number of minifilaments. In Type III cells, no long fiber could be assembled because there was no anchor for the fiber to be stabilized. The behavior of cells treated with blebbistatin was simulated by decreasing the contractile and aligning force of the minifilaments. The simulations captured the dynamics of myosin foci in blebbistatin treated cells, which show little contraction and alignment, but the turnover kinetics seems to be less affected. STICS analysis was applied on the simulation results in the same way as it was applied to the time-lapse MRLC-GFP images. The decay time of $r(0, \tau)$ for simulations of untreated cells and cells in blebbistatin is close to the value obtained using experimental data (Fig. 3.4, 3.5, 3.6, 4.2, 4.3.). Our model suggests that the kinetic processes of myosin minifilament assembly and disassembly; aligning and contraction; medial fiber anchoring on focal adhesions; stabilization upon increasing contractile tension; interaction with extracellular matrix through focal adhesions, contribute to the remodeling of medial cortical fibers.

Filamentous proteins, such as collagen fibers, microtubules and actomyosin bundles in muscle tissue can generate SHG excited by high intensity of IR pulse laser, which provides the information on the microstructures of cells and tissues. It is possible that the SHG signal from myosin minifilaments might vary quantifiably during the cortical fiber assembly and the reorganization of network because their conformation changes under tension and contraction. Thus SHG spectroscopy could be useful in the study of the mechanical and dynamical features of the cortical actomyosin network reorganization process. To explore this idea, we set up a SHG microscopic system on an Olympus IX81 confocal microscope, using a tunable wavelength pulse laser to produce SHG from samples. The SHG images of KNbO_3 crystals and starch granules obtained on this SHG microscope (see Chapter 2) demonstrate that our SHG microscopic system is successful. The calculations suggest that our low repetition rate pulse laser (CLARK laser) provides great advantages by generating much higher peak intensity (10^4 time larger) compared to the

Ti:Sapphire laser that is often used in SHG microscopy. However, we found that the photodamage to the cells was severe due to the absorption of high intensity IR laser. Another issue is that the CLARK pulse laser is not synchronized with the scanning system of Olympus microscope, which reduces the efficiency of SHG imaging. These issues will be studied and solved in future work.

6.2 Discussion and future work

Future work could further examine in more detail the process of minifilament assembly and disassembly on the cell cortex. Myosin minifilaments can be assembled from dimers at a rate nearly identical to the accumulation rate of minifilaments at the cortex [191]. Myosin minifilaments can bind to the cortex and accumulate under tension at the time scale of ~ 200 s [191, 192]. The unbinding rate of myosin II heads from actin filaments without tension is ~ 300 s⁻¹ [191]. A simple estimate of the rate of disassociation for a minifilament composed by 40 myosin II motors is $300 e^{-40E_S^j/k_B T} \approx 1.8 \times 10^{-3}$ s⁻¹ ($E_S^j = 0.3k_B T$ [191]), which is close to the value of $k_{d0} = 0.001$ s⁻¹ in simulations. The time lapse MRLC-GFP images show the myosin foci turnover in blebbistatin treated cells, however, it is difficult to distinguish the kinetics of myosin foci turnover in cells with blebbistatin treatment from the untreated cells. A prior study [192] suggested that the assembly of myosin bipolar filaments is accelerated by the tension.

Future work could explore in more detail how signaling pathways in the cells contribute to the assembly and disassembly of myosin filaments and fiber stabilization [193]. Phosphorylation regulates myosin minifilament assembly and treatment with drugs can interfere with this process. In this work we used blebbistatin. Our experiments demonstrate that the treatment of blebbistatin, which inhibits myosin II association with F-actin, directly disrupts the stress fibers along with the loss of focal adhesions both in number and size. The MRLC of myosin II in blebbistatin-treated cells has been shown to be mostly in the phosphorylated state and assembled in bipolar filaments [191, 192].

Rho-kinase activity is important for maintaining focal adhesions that associate with the medial fibers. The growth of focal adhesions is also correlated to the increase of tension along the stress fibers that anchor on the focal adhesions [171, 194]. When cells (fibroblasts and endothelial cells) were treated with

Y-27632, which inhibits myosin light chain phosphorylation by decreasing ROCK activity, the medial stress fibers were disrupted and focal adhesions disassembled, while most of the peripheral stress fibers were unaffected [195, 196]. When cells are treated with ML-7, the MLCK inhibitor, the peripheral stress fibers were observed to be weakened but the medial stress fibers remain stable [192, 196]. It is still not clear why the peripheral and medial stress fibers respond to the ROCK inhibitor and MLCK inhibitor differently, although both stress fibers contain ROCK and MLCK. Further investigation of time lapse MRMC-GFP images of cells with ROCK or MLCK inhibitor treatment is required to get better understand the network reorganization dynamics.

Although our 2D model is very simple, it could be used to study many experiments related to cytoskeletal network and stress fibers. For example, fibroblasts and epithelial cells cultivated on elastic substrates coated by collagen I develop cytoskeletal networks with different morphology and mechanical properties (e.g. viscoelasticity, Young's modulus and shear modulus, etc.) [60, 155, 197, 198]. Within one cell, the ventral, dorsal and transverse arc stress fibers are assembled by different mechanisms [199]. Our model could be used as a framework to investigate how the cytoskeletal network reorganizes in response to the external perturbation or mechanical incentive, such as cyclic stretching the elastic substrates [200, 201], laser incision of specific stress fibers inside a cell [202], and shear flow around the adherent cells [203]. It is promising to use this model to simulate the actomyosin network reorganization for the whole cell scale by integrating the mechanosensing through focal adhesion dynamics and configurations. It might also provide a tool for the guidance of polymer self-assembly or self-organization in the material synthesis engineering.

Reference

1. Alberts, B., A. Johnson, J. Lewis, M. Raff, K. Roberts, and P. Walter, *Molecular biology of the cell*. 4th ed. 2002, New York: Garland Science.
2. Pollard, T.D. and J.A. Cooper, *Actin, a central player in cell shape and movement*. Science, 2009. **326**(5957): p. 1208--1212.
3. Korn, E.D., M.-F. Carrier, and D. Pantaloni, *Actin polymerization and ATP hydrolysis*. Science, 1987. **238**(4827): p. 638-644.
4. Bernstein, B.W. and J.R. Bamburg, *ADF/cofilin: a functional node in cell biology*. Trends in cell biology, 2010. **20**(4): p. 187-95.
5. Lauffenburger, D.A. and A.F. Horwitz, *Cell migration: a physically integrated molecular process*. Cell, 1996. **84**(3): p. 359-369.
6. Pollard, T.D. and J.A. Cooper, *Actin, a central player in cell shape and movement*. Science, 2009. **326**(5957): p. 1208-1212.
7. Schroeder, T.E., *Actin in dividing cells: contractile ring filaments bind heavy meromyosin*. Proceedings of the National Academy of Sciences, 1973. **70**(6): p. 1688-1692.
8. Wu, J.-Q., J.R. Kuhn, D.R. Kovar, and T.D. Pollard, *Spatial and temporal pathway for assembly and constriction of the contractile ring in fission yeast cytokinesis*. Developmental cell, 2003. **5**(5): p. 723-734.
9. Rohatgi, R., L. Ma, H. Miki, M. Lopez, T. Kirchhausen, T. Takenawa, and M.W. Kirschner, *The interaction between N-WASP and the Arp2/3 complex links Cdc42-dependent signals to actin assembly*. Cell, 1999. **97**(2): p. 221-231.
10. Higgs, H.N. and T.D. Pollard, *Activation by Cdc42 and PIP2 of Wiskott-Aldrich syndrome protein (WASP) stimulates actin nucleation by Arp2/3 complex*. The Journal of cell biology, 2000. **150**(6): p. 1311-1320.
11. Kuhn, J.R. and T.D. Pollard, *Single molecule kinetic analysis of actin filament capping. Polyphosphoinositides do not dissociate capping proteins*. The Journal of biological chemistry, 2007. **282**(38): p. 28014-24.
12. Schafer, D.A., P.B. Jennings, and J.A. Cooper, *Dynamics of capping protein and actin assembly in vitro: uncapping barbed ends by polyphosphoinositides*. The Journal of cell biology, 1996. **135**(1): p. 169-179.
13. Andrianantoandro, E. and T.D. Pollard, *Mechanism of actin filament turnover by severing and nucleation at different concentrations of ADF/cofilin*. Mol. Cell, 2006. **24**: p. 13--23.
14. Carrier, M.-F., V. Laurent, J. Santolini, R. Melki, D. Didry, G.-X. Xia, Y. Hong, N.-H. Chua, and D. Pantaloni, *Actin depolymerizing factor (ADF/cofilin) enhances the rate of filament turnover: implication in actin-based motility*. The Journal of cell biology, 1997. **136**(6): p. 1307-1322.
15. McLaughlin, P., J. Gooch, H.-G. Mannherz, and A. Weeds, *Structure of gelsolin segment 1-actin complex and the mechanism of filament severing*. 1993.
16. Ono, S., *Mechanism of depolymerization and severing of actin filaments and its significance in cytoskeletal dynamics*. International review of cytology, 2007. **258**: p. 1-82.
17. van der Flier, A. and A. Sonnenberg, *Structural and functional aspects of filamins*. Biochimica et Biophysica Acta (BBA)-Molecular Cell Research, 2001. **1538**(2): p. 99-117.
18. Lazarides, E., *Actin, alpha-actinin, and tropomyosin interaction in the structural organization of actin filaments in nonmuscle cells*. The Journal of cell biology, 1976. **68**(2): p. 202-219.
19. Köhler, S. and A.R. Bausch, *Contraction mechanisms in composite active actin networks*. PloS one, 2012. **7**(7): p. e39869.
20. Thoresen, T., M. Lenz, and M.L. Gardel, *Reconstitution of contractile actomyosin bundles*. Biophys J, 2011. **100**(11): p. 2698-705.
21. Karsenti, E., F. Nédélec, and T. Surrey, *Modelling microtubule patterns*. Nat. Cell Biol., 2006. **8**(11): p. 1204--1211.
22. Kirschner, M. and T. Mitchison, *Beyond self-assembly: from microtubules to morphogenesis*. Cell, 1986. **45**(3): p. 329-342.

23. Odde, D.J., L. Cassimeris, and H.M. Buettner, *Kinetics of microtubule catastrophe assessed by probabilistic analysis*. Biophysical journal, 1995. **69**(3): p. 796-802.
24. Desai, A. and T.J. Mitchison, *Microtubule polymerization dynamics*. Annual review of cell and developmental biology, 1997. **13**(1): p. 83-117.
25. Mitchison, T. and M. Kirschner, *Dynamic instability of microtubule growth*. Nature, 1984. **312**(5991): p. 237-242.
26. Maccioni, R.B. and V. Cambiazo, *Role of microtubule-associated proteins in the control of microtubule assembly*. Physiological Reviews, 1995. **75**(4): p. 835-864.
27. Cassimeris, L. and C. Spittle, *Regulation of microtubule-associated proteins*. International review of cytology, 2001. **210**: p. 163-226.
28. Vallee, R.B., *A taxol-dependent procedure for the isolation of microtubules and microtubule-associated proteins (MAPs)*. The Journal of cell biology, 1982. **92**(2): p. 435-442.
29. Jordan, M.A., D. Thrower, and L. Wilson, *Effects of vinblastine, podophyllotoxin and nocodazole on mitotic spindles. Implications for the role of microtubule dynamics in mitosis*. Journal of cell science, 1992. **102**(3): p. 401-416.
30. Janmey, P.A., U. Euteneuer, P. Traub, and M. Schliwa, *Viscoelastic properties of vimentin compared with other filamentous biopolymer networks*. The Journal of cell biology, 1991. **113**(1): p. 155-160.
31. Wang, N. and D. Stamenović, *Contribution of intermediate filaments to cell stiffness, stiffening, and growth*. American Journal of Physiology-Cell Physiology, 2000. **279**(1): p. C188-C194.
32. Bruel, A., S. Paschke, S. Jainta, Y. Zhang, J. Vassy, J.P. Rigaut, and M. Beil, *Remodeling of vimentin cytoskeleton correlates with enhanced motility of promyelocytic leukemia cells during differentiation induced by retinoic acid*. Anticancer research, 2000. **21**(6A): p. 3973-3980.
33. Morris, N.R., *Nuclear migration from fungi to the mammalian brain*. The Journal of cell biology, 2000. **148**(6): p. 1097-1102.
34. Kural, C., H. Kim, S. Syed, G. Goshima, V.I. Gelfand, and P.R. Selvin, *Kinesin and dynein move a peroxisome in vivo: a tug-of-war or coordinated movement?* Science, 2005. **308**(5727): p. 1469-1472.
35. Randall, D., W. Burggren, and K. French, *Eckert animal physiology*. 2002: Macmillan.
36. Street, C.A. and B.A. Bryan, *Rho kinase proteins—pleiotropic modulators of cell survival and apoptosis*. Anticancer research, 2011. **31**(11): p. 3645-3657.
37. Uhlen M, O.P., Fagerberg L, Lundberg E, Jonasson K, Forsberg M, Zwahlen M, Kampf C, Wester K, Hober S, Wernerus H, Björling L, Ponten F., *Towards a knowledge-based Human Protein Atlas*. Nat Biotechnol., 2010. **28**(12): p. 1248-1250.
38. Conde, C. and A. Cáceres, *Microtubule assembly, organization and dynamics in axons and dendrites*. Nature Reviews Neuroscience, 2009. **10**(5): p. 319-332.
39. Mahr, J. *The cytoskeleton*. 2013; Available from: cnx.org/content/m47861/latest/#fig-ch04-05-03.
40. Parsons, J.T., A.R. Horwitz, and M.A. Schwartz, *Cell adhesion: integrating cytoskeletal dynamics and cellular tension*. Nat. Rev. Mol. Cell Biol., 2010. **11**(9): p. 633-643.
41. Cary, L.A., J.F. Chang, and J.-L. Guan, *Stimulation of cell migration by overexpression of focal adhesion kinase and its association with Src and Fyn*. Journal of cell science, 1996. **109**(7): p. 1787-1794.
42. Totsukawa, G., Y. Wu, Y. Sasaki, D.J. Hartshorne, Y. Yamakita, S. Yamashiro, and F. Matsumura, *Distinct roles of MLCK and ROCK in the regulation of membrane protrusions and focal adhesion dynamics during cell migration of fibroblasts*. The Journal of cell biology, 2004. **164**(3): p. 427-439.
43. Gupton, S.L. and C.M. Waterman-Storer, *Spatiotemporal feedback between actomyosin and focal adhesion systems optimizes rapid cell migration*. Cell, 2006. **125**(7): p. 1361-1374.
44. Pellegrin, S. and H. Mellor, *Actin stress fibres*. Journal of cell science, 2007. **120**(20): p. 3491-3499.
45. Mason, T., K. Ganesan, J. Van Zanten, D. Wirtz, and S. Kuo, *Particle tracking microrheology of complex fluids*. Physical review letters, 1997. **79**(17): p. 3282.
46. Yamada, S., D. Wirtz, and S.C. Kuo, *Mechanics of living cells measured by laser tracking microrheology*. Biophysical Journal, 2000. **78**(4): p. 1736-1747.

47. Kuznetsova, T.G., M.N. Starodubtseva, N.I. Yegorenkov, S.A. Chizhik, and R.I. Zhdanov, *Atomic force microscopy probing of cell elasticity*. *Micron*, 2007. **38**(8): p. 824-833.
48. Mizuno, D., C. Tardin, C. Schmidt, and F. MacKintosh, *Nonequilibrium mechanics of active cytoskeletal networks*. *Science*, 2007. **315**(5810): p. 370-373.
49. Lee, H., J.M. Ferrer, F. Nakamura, M.J. Lang, and R.D. Kamm, *Passive and active microrheology for cross-linked F-actin networks < i> in vitro</i>*. *Acta biomaterialia*, 2010. **6**(4): p. 1207-1218.
50. Li, Q., G. Lee, C. Ong, and C. Lim, *AFM indentation study of breast cancer cells*. *Biochemical and biophysical research communications*, 2008. **374**(4): p. 609-613.
51. Pelling, A.E., Y. Li, W. Shi, and J.K. Gimzewski, *Nanoscale visualization and characterization of Myxococcus xanthus cells with atomic force microscopy*. *Proceedings of the National Academy of Sciences of the United States of America*, 2005. **102**(18): p. 6484-6489.
52. Hochmuth, R.M., *Micropipette aspiration of living cells*. *Journal of biomechanics*, 2000. **33**(1): p. 15-22.
53. Sagvolden, G., I. Giaever, E. Pettersen, and J. Feder, *Cell adhesion force microscopy*. *Proceedings of the National Academy of Sciences*, 1999. **96**(2): p. 471-476.
54. Galbraith, C.G., K.M. Yamada, and M.P. Sheetz, *The relationship between force and focal complex development*. *The Journal of cell biology*, 2002. **159**(4): p. 695-705.
55. Sabass, B., M.L. Gardel, C.M. Waterman, and U.S. Schwarz, *High resolution traction force microscopy based on experimental and computational advances*. *Biophysical journal*, 2008. **94**(1): p. 207-220.
56. Shah, N., A. Sattar, M. Benanti, S. Hollander, and L. Cheuck, *Magnetic resonance spectroscopy as an imaging tool for cancer: a review of the literature*. *JAOA: Journal of the American Osteopathic Association*, 2006. **106**(1): p. 23-27.
57. Heim, R. and R.Y. Tsien, *Engineering green fluorescent protein for improved brightness, longer wavelengths and fluorescence resonance energy transfer*. *Current Biology*, 1996. **6**(2): p. 178-182.
58. McMullan, D., *Scanning electron microscopy 1928–1965*. *Scanning*, 1995. **17**(3): p. 175-185.
59. Jones, S.A., S.-H. Shim, J. He, and X. Zhuang, *Fast, three-dimensional super-resolution imaging of live cells*. *Nature methods*, 2011. **8**(6): p. 499-505.
60. Discher, D.E., P. Janmey, and Y.-I. Wang, *Tissue cells feel and respond to the stiffness of their substrate*. *Science*, 2005. **310**(5751): p. 1139-1143.
61. Mogilner, A., R. Wollman, and W.F. Marshall, *Quantitative modeling in cell biology: what is it good for?* *Developmental cell*, 2006. **11**(3): p. 279-287.
62. Huber, F., J. Schnauss, S. Rönicke, P. Rauch, K. Müller, C. Fütterer, and J. Käs, *Emergent complexity of the cytoskeleton: from single filaments to tissue*. *Advances in Physics*, 2013. **62**(1): p. 1-112.
63. Stachowiak, M.R., P.M. McCall, T. Thoresen, H.E. Balcioğlu, L. Kasiewicz, M.L. Gardel, and B. O'Shaughnessy, *Self-organization of myosin II in reconstituted actomyosin bundles*. *Biophysical journal*, 2012. **103**(6): p. 1265-1274.
64. Stachowiak, M.R. and B. O'Shaughnessy, *Kinetics of stress fibers*. *New Journal of Physics*, 2008. **10**(2): p. 025002.
65. Yoshinaga, N., J.-F. Joanny, J. Prost, and P. Marcq, *Polarity patterns of stress fibers*. *Physical review letters*, 2010. **105**(23): p. 238103.
66. Walcott, S. and S.X. Sun, *A mechanical model of actin stress fiber formation and substrate elasticity sensing in adherent cells*. *Proceedings of the National Academy of Sciences*, 2010. **107**(17): p. 7757-7762.
67. Dasanayake, N.L., P.J. Michalski, and A.E. Carlsson, *General mechanism of actomyosin contractility*. *Physical review letters*, 2011. **107**(11): p. 118101.
68. Bathe, M., C. Heussinger, M.M. Claessens, A.R. Bausch, and E. Frey, *Cytoskeletal bundle mechanics*. *Biophysical journal*, 2008. **94**(8): p. 2955-2964.
69. Storm, C., J.J. Pastore, F.C. MacKintosh, T.C. Lubensky, and P.A. Janmey, *Nonlinear elasticity in biological gels*. *Nature*, 2005. **435**(7039): p. 191-194.
70. Liverpool, T.B. and M.C. Marchetti, *Instabilities of isotropic solutions of active polar filaments*. *Physical review letters*, 2003. **90**(13): p. 138102.
71. Kruse, K., J. Joanny, F. Jülicher, J. Prost, and K. Sekimoto, *Asters, vortices, and rotating spirals in active gels of polar filaments*. *Physical review letters*, 2004. **92**(7): p. 078101.

72. Ziebert, F., I.S. Aranson, and L.S. Tsimring, *Effects of cross-linkers on motor-mediated filament organization*. New Journal of Physics, 2007. **9**: p. 421.
73. Chelakkot, R., R. Lipowsky, and T. Gruhn, *Self-assembling network and bundle structures in systems of rods and crosslinkers - A Monte Carlo study*. Soft Matter, 2009. **5**: p. 1504-1513.
74. Vavylonis, D., J.Q. Wu, S. Hao, B. O'Shaughnessy, and T.D. Pollard, *Assembly mechanism of the contractile ring for cytokinesis by fission yeast*. Science, 2008. **319**: p. 97-100.
75. Nédélec, F.J., T. Surrey, A.C. Maggs, and S. Leibler, *Self-organization of microtubules and motors*. Nature, 1997. **389**: p. 305-308.
76. Mogilner, A., R. Wollman, G. Civelekoglu-Scholey, and J. Scholey, *Modeling mitosis*. Trends Cell Biol., 2006. **16**(2): p. 88-96.
77. Koenderink, G.H., Z. Dogic, F. Nakamura, P.M. Bendix, F.C. MacKintosh, J.H. Hartwig, T.P. Stossel, and D.A. Weitz, *An active biopolymer network controlled by molecular motors*. Proc Natl Acad Sci U S A, 2009. **106**(36): p. 15192-7.
78. Kohler, S., V. Schaller, and A.R. Bausch, *Structure formation in active networks*. Nature materials, 2011. **10**(6): p. 462-8.
79. Engler, A.J., S. Sen, H.L. Sweeney, and D.E. Discher, *Matrix elasticity directs stem cell lineage specification*. Cell, 2006. **126**(4): p. 677-689.
80. Stricker, J., Y. Beckham, M.W. Davidson, and M.L. Gardel, *Myosin II-Mediated Focal Adhesion Maturation Is Tension Insensitive*. PloS one, 2013. **8**(7): p. e70652.
81. JIANG, X., J. ZHONG, Y. LIU, H. YU, S. ZHUO, and J. CHEN, *Two-Photon Fluorescence and Second-Harmonic Generation Imaging of Collagen in Human Tissue Based on Multiphoton Microscopy*. Scanning, 2011. **33**.
82. Perry, S.W., R.M. Burke, and E.B. Brown, *Two-Photon and Second Harmonic Microscopy in Clinical and Translational Cancer Research*. Annals of Biomedical Engineering, 2012. **40**(2): p. 277-291.
83. Yang, X., Y. Pu, C.L. Hsieh, C.A. Ong, D. Psaltis, and K.M. Stankovic, *Two-photon microscopy of the mouse cochlea in situ for cellular diagnosis*. Journal of Biomedical Optics, 2013. **18**(3).
84. Reshak, A.H. and C.R. Sheue, *Second harmonic generation imaging of the deep shade plant Selaginella erythropus using multifunctional two-photon laser scanning microscopy*. Journal of Microscopy, 2012. **248**(3): p. 234-244.
85. Wu, X.F., G. Chen, J.P. Lu, W.F. Zhu, J.T. Qiu, J.X. Chen, S.S. Xie, S.M. Zhuo, and J. Yan, *Label-Free Detection of Breast Masses Using Multiphoton Microscopy*. Plos One, 2013. **8**(6).
86. Jiang, X.S., J.Z. Zhong, Y.C. Liu, H.B. Yu, S.M. Zhuo, and J.X. Chen, *Two-Photon Fluorescence and Second-Harmonic Generation Imaging of Collagen in Human Tissue Based on Multiphoton Microscopy*. Scanning, 2011. **33**(1): p. 53-56.
87. Campagnola, P., *Second Harmonic Generation Imaging Microscopy: Applications to Diseases Diagnostics*. Analytical Chemistry, 2011. **83**(9): p. 3224-3231.
88. Campagnola, P.J. and C.Y. Dong, *Second harmonic generation microscopy: principles and applications to disease diagnosis*. Laser & Photonics Reviews, 2011. **5**(1): p. 13-26.
89. Brown, C.P., M.A. Houle, M. Chen, A.J. Price, F. Legare, and H.S. Gill, *Damage initiation and progression in the cartilage surface probed by nonlinear optical microscopy*. Journal of the Mechanical Behavior of Biomedical Materials, 2012. **5**(1): p. 62-70.
90. Mansfield, J.C. and C.P. Winlove, *A multi-modal multiphoton investigation of microstructure in the deep zone and calcified cartilage*. Journal of Anatomy, 2012. **220**(4): p. 405-416.
91. Zhu, X., Y. Tang, J. Chen, S. Xiong, S. Zhuo, and J. Chen, *Monitoring wound healing of elastic cartilage using multiphoton microscopy*. Osteoarthritis and Cartilage, 2013. **21**(11): p. 1799-1806.
92. Bueno, J.M., E.J. Gualda, and P. Artal, *Analysis of Corneal Stroma Organization With Wavefront Optimized Nonlinear Microscopy*. Cornea, 2011. **30**(6): p. 692-701.
93. Hana, M., G. Giesec, and J.F. Billeb, *Second harmonic generation imaging of collagen fibrils in cornea and sclera*. Optics Express, 2005. **13**(15).
94. Johnson, A.W., D.A. Ammar, and M.Y. Kahook, *Two-Photon Imaging of the Mouse Eye*. Investigative Ophthalmology & Visual Science, 2011. **52**(7): p. 4098-4105.
95. Latour, G., I. Gusachenko, L. Kowalczyk, I. Lamarre, and M.C. Schanne-Klein, *In vivo structural imaging of the cornea by polarization-resolved second harmonic microscopy*. Biomedical Optics Express, 2012. **3**(1): p. 1-15.

96. Latour, G., L. Kowalczyk, M. Savoldelli, J.L. Bourges, K. Plamann, F. Behar-Cohen, and M.C. Schanne-Klein, *Hyperglycemia-Induced Abnormalities in Rat and Human Corneas: The Potential of Second Harmonic Generation Microscopy*. Plos One, 2012. **7**(11).
97. Caorsi, V., C. Toepfer, M.B. Sikkell, A.R. Lyon, K. MacLeod, and M.A. Ferenczi, *Non-Linear Optical Microscopy Sheds Light on Cardiovascular Disease*. Plos One, 2013. **8**(2).
98. Liu, H.H., Y.H. Shao, W. Qin, R.B. Runyan, M.F. Xu, Z. Ma, T.K. Borg, R. Markwald, and B.Z. Gao, *Myosin filament assembly onto myofibrils in live neonatal cardiomyocytes observed by TPEF-SHG microscopy*. Cardiovascular Research, 2013. **97**(2): p. 262-270.
99. Martin, T.P., G. Norris, G. McConnell, and S. Currie, *A novel approach for assessing cardiac fibrosis using label-free second harmonic generation*. International Journal of Cardiovascular Imaging, 2013. **29**(8): p. 1733-1740.
100. Culic-Viskota, J., W.P. Dempsey, S.E. Fraser, and P. Pantazis, *Surface functionalization of barium titanate SHG nanoprobe for in vivo imaging in zebrafish*. Nature Protocols, 2012. **7**(9): p. 1618-1633.
101. Mahou, P., N. Olivier, G. Labroille, L. Duloquin, J.M. Sintès, N. Peyrieras, R. Legouis, D. Debarre, and E. Beaurepaire, *Combined third-harmonic generation and four-wave mixing microscopy of tissues and embryos*. Biomedical Optics Express, 2011. **2**(10): p. 2837-2849.
102. Olivier, N., M.A. Luengo-Oroz, L. Duloquin, E. Faure, T. Savy, I. Veilleux, X. Solinas, D. Débarre, P. Bourguine, A. Santos, N. Peyriéras, and E. Beaurepaire, *Cell Lineage Reconstruction of Early Zebrafish Embryos Using Label-Free Nonlinear Microscopy*. Science, 2010. **329**.
103. Thayil, A., T. Watanabe, A. Jesacher, T. Wilson, S. Srinivas, and M. Booth, *Long-term imaging of mouse embryos using adaptive harmonic generation microscopy*. Journal of Biomedical Optics, 2011. **16**(4).
104. Franken, P.A., A.E. Hill, C.W. Peters, and G. Weinreich, *Generation of Optical Harmonics*. Physical Review Letters, 1961. **7**.
105. Armstrong, J., N. Bloembergen, J. Ducuing, and P. Pershan, *Interactions between Light Waves in a Nonlinear Dielectric*. Physical review, 1962. **127**(6): p. 1918-1939.
106. Bloembergen, N. and P.S. Pershan, *Light Waves at Boundary of Nonlinear Media*. Physical review, 1962. **128**(2).
107. Oudar, J.L. and J. Zyss, *Structural dependence of nonlinear-optical properties of methyl(2,4-dinitrophenyl)-aminopropanoate crystals*. Physical Review A, 1982. **26**(4).
108. Rivard, M., C.A. Couture, A.K. Miri, M. Laliberte, A. Bertrand-Grenier, L. Mongeau, and F. Legare, *Imaging the bipolarity of myosin filaments with Interferometric Second Harmonic Generation microscopy*. Biomedical Optics Express, 2013. **4**(10): p. 2078-2086.
109. Chu, S.-W., S.-Y. Chen, G.-W. Chern, T.-H. Tsai, Y.-C. Chen, B.-L. Lin, and C.-K. Sun, *Studies of $\chi(2)/\chi(3)$ Tensors in Submicron-Scaled Bio-Tissues by Polarization Harmonics Optical Microscopy*. Biophysical Journal, 2004. **86**(6): p. 3914-3922.
110. Chu, S.-W., S.-P. Tai, T.-M. Liu, C.-K. Sun, and C.-H. Lin, *Selective imaging in second-harmonic-generation microscopy with anisotropic radiation*. Journal of Biomedical Optics, 2009. **14**(1).
111. Recher, G., D. Rouède, E. Schaub, and F. Tiaho, *Skeletal muscle sarcomeric SHG patterns photo-conversion by femtosecond infrared laser*. Biomedical Optics Express, 2011. **2**(2): p. 374-384.
112. Recher, G., D. Rouède, C. Tascon, L.A. D'Amico, and F. Tiaho, *Double-band sarcomeric SHG pattern induced by adult skeletal muscles alteration during myofibrils preparation*. Journal of Microscopy, 2011. **241**(2): p. 207-211.
113. Rouède, D., J.J. Bellanger, E. Schaub, G. Recher, and F. Tiaho, *Theoretical and Experimental SHG Angular Intensity Patterns from Healthy and Proteolysed Muscles*. Biophysical Journal, 2013. **104**(9): p. 1959-1968.
114. Rouède, D., G. Recher, J.J. Bellanger, M.T. Lavault, E. Schaub, and F. Tiaho, *Modeling of Supramolecular Centrosymmetry Effect on Sarcomeric SHG Intensity Pattern of Skeletal Muscles*. Biophysical Journal, 2011. **101**(2): p. 494-503.
115. Yamashiro, S., H. Mizuno, M.B. Smith, G.L. Ryan, T. Kiuchi, D. Vavylonis, and N. Watanabe, *New single-molecule speckle microscopy reveals modification of the retrograde actin flow by focal adhesions at nanometer scales*. Mol Biol Cell, 2014.

116. Xu, T., D. Vavylonis, and X. Huang, *3D actin network centerline extraction with multiple active contours*. Medical image analysis, 2014. **18**(2): p. 272-84.
117. Ryan, G.L., H.M. Petroccia, N. Watanabe, and D. Vavylonis, *Excitable actin dynamics in lamellipodial protrusion and retraction*. Biophys J, 2012. **102**(7): p. 1493-502.
118. Huff, T.B., Y. Shi, Y. Fu, H. Wang, and J.-X. Cheng, *Multimodal Nonlinear Optical Microscopy and Applications to Central Nervous System Imaging*. IEEE Journal of Selected Topics in Quantum Electronics, 2008. **14**(1): p. 4-9.
119. Chu, S.-W., T.-M. Liu, and C.-K. Sun, *Real-time second-harmonic-generation microscopy based on a 2-GHz repetition rate Ti:sapphire laser*. Optics Express, 2003. **11**(8): p. 933-938.
120. Dmitriev, V.G., M.V. Osipov, V.N. Puzyrev, A.T. Sahakyan, A.N. Starodub, and B.L. Vasin, *Nonlinear optical conversion of Nd:glass laser multimode radiation into the second harmonic in KDP crystal*. Journal of Physics B-Atomic Molecular and Optical Physics, 2012. **45**(16).
121. Tiaho, F., G. Recher, and D. Rouède, *Estimation of helical angles of myosin and collagen by second harmonic generation imaging microscopy*. Optics Express, 2007. **15**(19).
122. Nucciotti, V., C. Stringari, L. Sacconi, F. Vanzi, L. Fusi, M. Linari, G. Piazzesi, V. Lombardi, and F.S. Pavone, *Probing myosin structural conformation in vivo by second-harmonic generation microscopy*. Proceedings of the National Academy of Sciences, 2010. **107**(17): p. 7763-7768.
123. Chen, X.Y., O. Nadiarynk, S. Plotnikov, and P.J. Campagnola, *Second harmonic generation microscopy for quantitative analysis of collagen fibrillar structure*. Nature Protocols, 2012. **7**(4): p. 654-669.
124. Plotnikov, S., V. Juneja, A.B. Isaacson, W.A. Mohler, and P.J. Campagnola, *Optical Clearing for Improved Contrast in Second Harmonic Generation Imaging of Skeletal Muscle*. Biophysical Journal, 2006. **90**(1): p. 328-339.
125. Hotulainen, P., *Stress fibers are generated by two distinct actin assembly mechanisms in motile cells*. The Journal of Cell Biology, 2006. **173**(3): p. 383-394.
126. Ojkic, N. and D. Vavylonis, *Kinetics of Myosin Node Aggregation into a Contractile Ring*. Physical Review Letters, 2010. **105**(4).
127. Ojkic, N., J.Q. Wu, and D. Vavylonis, *Model of myosin node aggregation into a contractile ring: the effect of local alignment*. Journal of Physics-Condensed Matter, 2011. **23**(37).
128. Vavylonis, D., J.Q. Wu, S. Hao, B. O'Shaughnessy, and T.D. Pollard, *Assembly mechanism of the contractile ring for cytokinesis by fission yeast*. Science, 2008. **319**(5859): p. 97-100.
129. Débarre, D., W. Supatto, A.-M. Pena, A. Fabre, T. Tordjmann, L. Combettes, M.-C. Schanne-Klein, and E. Beaupaire, *Imageing lipid bodies in cells and tissues using third-harmonic generation microscopy*. Nature Methods, 2006. **3**(1).
130. Dietzel, S., U. Pohl, F. Krombach, and M. Rehberg, *Deep tissue microscopy with second and third harmonic generation: label-free 3D visualization of cellular and tissue structures in intact muscle*. Journal of Vascular Research, 2011. **48**: p. 15-15.
131. Rehberg, M., F. Krombach, U. Pohl, and S. Dietzel, *Label-Free 3D Visualization of Cellular and Tissue Structures in Intact Muscle with Second and Third Harmonic Generation Microscopy*. Plos One, 2011. **6**(11).
132. Schriebl, A.J., A.J. Reinisch, S. Sankaran, D.M. Pierce, and G.A. Holzapfel, *Quantitative assessment of collagen fibre orientations from two-dimensional images of soft biological tissues*. Journal of the Royal Society Interface, 2012. **9**(76): p. 3081-3093.
133. Shen, C.C. and T.Y. Shi, *Third harmonic transmit phasing for SNR improvement in tissue harmonic imaging with Golay-encoded excitation*. Ultrasonics, 2011. **51**(5): p. 554-560.
134. Tsai, M.R., S.Y. Chen, D.B. Shieh, P.J. Lou, and C.K. Sun, *In vivo optical virtual biopsy of human oral mucosa with harmonic generation microscopy*. Biomedical Optics Express, 2011. **2**(8): p. 2317-2328.
135. Adur, J., V.B. Pelegati, L.F.L. Costa, L. Pietro, A.A. de Thomaz, D.B. Almeida, F. Bottcher-Luiz, L.A.L.A. Andrade, and C.L. Cesar, *Recognition of serous ovarian tumors in human samples by multimodal nonlinear optical microscopy*. Journal of Biomedical Optics, 2011. **16**(9).
136. Adur, J., V.B. Pelegati, A.A. de Thomaz, M.O. Baratti, D.B. Almeida, L.A.L.A. Andrade, F. Bottcher-Luiz, H.F. Carvalho, and C.L. Cesar, *Optical Biomarkers of Serous and Mucinous Human Ovarian Tumor Assessed with Nonlinear Optics Microscopies*. Plos One, 2012. **7**(10).

137. Psilodimitrakopoulos, S., I. Amat-Roldan, P. Loza-Alvarez, and D. Artigas, *Estimating the helical pitch angle of amylopectin in starch using polarization second harmonic generation microscopy*. Journal of Optics, 2010. **12**(8): p. 084007.
138. Zhuo, Z.-Y., C.-S. Liao, C.-H. Huang, J.-Y. Yu, Y.-Y. Tzeng, W. Lo, C.-Y. Dong, H.-C. Chui, Y.-C. Huang, H.-M. Lai, and S.-W. Chu, *Second harmonic generation imaging – A new method for unraveling molecular information of starch*. Journal of Structural Biology, 2010. **171**.
139. Mazumder, N., J.J. Qiu, M.R. Foreman, C.M. Romero, P. Torok, and F.J. Kao, *Stokes vector based polarization resolved second harmonic microscopy of starch granules*. Biomedical Optics Express, 2013. **4**(4): p. 538-547.
140. Warren, S.G. and R.E. Brandt, *Optical constants of ice from the ultraviolet to the microwave: A revised compilation*. Journal of Geophysical Research, 2008. **113**(D14).
141. Pope, R.M. and E.S. Fry, *Absorption spectrum ~380–700 nm of pure water. II. Integrating cavity measurements*. APPLIED OPTICS, 1997. **36**(33).
142. Sogandares, F.M. and E.S. Fry, *Absorption spectrum ~340–640 nm of pure water. I. Photothermal measurements*. APPLIED OPTICS, 1997. **36**(33): p. 8699.
143. Simanovski, D., M. Sarkar, A. Irani, C. O'Connell-Rodwell, C. Contag, H.A. Schwettman, and D. Palanker. *Cellular tolerance to pulsed heating*. in *Biomedical Optics 2005*. 2005: International Society for Optics and Photonics.
144. Stuart, B.C., M.D. Feit, S. Herman, A.M. Rubenchik, B.W. Shore, and M.D. Perry, *Optical ablation by high-power short-pulse lasers*. J. Opt. Soc. Am. B, 1995. **13**(2): p. 459.
145. König, K., T.W. Becker, P. Fischer, I. Riemann, and K.-J. Halbhauer, *Pulse-length dependence of cellular response to intense near-infrared laser pulses in multiphoton microscopes*. Optics Letters, 1999. **24**(2).
146. Segelstein, D.J., *The complex refractive index of water*. 2011, University of Missouri--Kansas City.
147. Hale, G.M. and M.R. Querry, *Optical constants of water in the 200-nm to 200- μ m wavelength region*. APPLIED OPTICS, 1973. **12**(3): p. 555-563.
148. Kamijo, K., N. Ohara, M. Abe, T. Uchimura, H. Hosoya, J.S. Lee, and T. Miki, *Dissecting the role of Rho-mediated signaling in contractile ring formation*. Mol. Biol. Cell, 2006. **17**: p. 43--55.
149. Kruse, K. and F. Jülicher, *Actively contracting bundles of polar filaments*. Physical Review Letters, 2000. **85**(8): p. 1778.
150. Kruse, K., J.F. Joanny, F. Jülicher, J. Prost, and K. Sekimoto, *Asters, Vortices, and Rotating Spirals in Active Gels of Polar Filaments*. Phys. Rev. Lett., 2004. **92**(7): p. 078101--.
151. Kang, J., R.L. Steward, Y. Kim, R.S. Schwartz, P.R. LeDuc, and K.M. Puskar, *Response of an actin filament network model under cyclic stretching through a coarse grained Monte Carlo approach*. Journal of theoretical biology, 2011. **274**(1): p. 109-119.
152. Smith, M.B., H. Li, T. Shen, X. Huang, E. Yusuf, and D. Vavylonis, *Segmentation and tracking of cytoskeletal filaments using open active contours*. Cytoskeleton, 2010. **67**: p. 693--705.
153. Huang, S., Z. Sun, Z. Li, L.A. MARTINEZ-LEMUS, and G.A. Meininger, *Modulation of Microvascular Smooth Muscle Adhesion and Mechanotransduction by Integrin-Linked Kinase*. Microcirculation, 2010. **17**(2): p. 113-127.
154. Curley, C.T., K. Fanale, and S.S. Jedlicka. *Characterizing the effect of substrate stiffness on neural stem cell differentiation*. in *MRS Proceedings*. 2013: Cambridge Univ Press.
155. Yeung, T., P.C. Georges, L.A. Flanagan, B. Marg, M. Ortiz, M. Funaki, N. Zahir, W. Ming, V. Weaver, and P.A. Janmey, *Effects of substrate stiffness on cell morphology, cytoskeletal structure, and adhesion*. Cell motility and the cytoskeleton, 2005. **60**(1): p. 24-34.
156. Brochu, H. and P. Vermette, *Young's moduli of surface-bound liposomes by atomic force microscopy force measurements*. Langmuir, 2008. **24**(5): p. 2009-2014.
157. Zumdieck, A., M.C. Lagomarsino, C. Tanase, K. Kruse, B. Mulder, M. Dogterom, and F. Jülicher, *Continuum description of the cytoskeleton: ring formation in the cell cortex*. Physical Review Letters, 2005. **95**(25): p. 258103.
158. Vavylonis, D., J.-Q. Wu, S. Hao, B. O'Shaughnessy, and T.D. Pollard, *Assembly mechanism of the contractile ring for cytokinesis by fission yeast*. Science, 2008. **319**(5859): p. 97-100.
159. Shlomovitz, R. and N. Gov, *Membrane-mediated interactions drive the condensation and coalescence of FtsZ rings*. Physical biology, 2009. **6**(4): p. 046017.

160. Sinard, J.H., W.F. Stafford, and T.D. Pollard, *The mechanism of assembly of Acanthamoeba myosin-II minifilaments: minifilaments assemble by three successive dimerization steps*. The Journal of cell biology, 1989. **109**(4): p. 1537-1547.
161. Walcott, S. and S.X. Sun, *A mechanical model of actin stress fiber formation and substrate elasticity sensing in adherent cells*. Proc Natl Acad Sci U S A, 2010. **107**(17): p. 7757--7762.
162. Mogilner, A., R. Wollman, G. Civelekoglu-Scholey, and J. Scholey, *Modeling mitosis*. Trends in cell biology, 2006. **16**(2): p. 88-96.
163. Luo, W., C.H. Yu, Z.Z. Lieu, J. Allard, A. Mogilner, M.P. Sheetz, and A.D. Bershadsky, *Analysis of the local organization and dynamics of cellular actin networks*. The Journal of cell biology, 2013. **202**(7): p. 1057-73.
164. Shutova, M., C. Yang, J.M. Vasiliev, and T. Svitkina, *Functions of nonmuscle myosin II in assembly of the cellular contractile system*. PloS one, 2012. **7**(7): p. e40814.
165. Kaksonen, M., Y. Sun, and D.G. Drubin, *A pathway for association of receptors, adaptors, and actin during endocytic internalization*. Cell, 2003. **115**: p. 475--487.
166. Llewellyn, M.E., R.P. Barretto, S.L. Delp, and M.J. Schnitzer, *Minimally invasive high-speed imaging of sarcomere contractile dynamics in mice and humans*. Nature, 2008. **454**(7205): p. 784-788.
167. Shin, J.H., M.L. Gardel, L. Mahadevan, P. Matsudaira, and D.A. Weitz, *Relating microstructure to rheology of a bundled and cross-linked F-actin network in vitro*. Proc Natl Acad Sci U S A, 2004. **101**(26): p. 9636-41.
168. Alvarado, J., M. Sheinman, A. Sharma, F.C. MacKintosh, and G.H. Koenderink, *Molecular motors robustly drive active gels to a critically connected state*. Nature Physics, 2013. **9**(9): p. 591-597.
169. Verkhovskiy, A.B., T.M. Svitkina, and G.G. Borisy, *Myosin II filament assemblies in the active lamella of fibroblasts: their morphogenesis and role in the formation of actin filament bundles*. The Journal of cell biology, 1995. **131**(4): p. 989-1002.
170. Burnette, D.T., S. Manley, P. Sengupta, R. Sougrat, M.W. Davidson, B. Kachar, and J. Lippincott-Schwartz, *A role for actin arcs in the leading-edge advance of migrating cells*. Nat. Cell Biol., 2011. **13**(4): p. 371-382.
171. Aratyn-Schaus, Y., P.W. Oakes, and M.L. Gardel, *Dynamic and structural signatures of lamellar actomyosin force generation*. Mol. Biol. Cell, 2011. **22**(8): p. 1330-1339.
172. Kolin, D.L. and P.I.W. Wiseman, *Advances in image correlation spectroscopy: measuring number densities, aggregation states, and dynamics of fluorescently labeled macromolecules in cells*. Cell Biochem. Biophys., 2007. **49**: p. 141--164.
173. Smith, M.B., E. Karatekin, A. Gohlke, H. Mizuno, N. Watanabe, and D. Vavylonis, *Interactive, Computer-Assisted Tracking of Speckle Trajectories in Fluorescence Microscopy: Application to Actin Polymerization and Membrane Fusion*. Biophys. J., 2011. **101**(7): p. 1794-1804.
174. Wiseman, P.W. and N.O. Petersen, *Image Correlation Spectroscopy. II. Optimization for Ultrasensitive Detection of Preexisting Platelet-Derived Growth Factor- β Receptor Oligomers on Intact Cells*. Biophysical Journal, 1999. **76**(2): p. 963-977.
175. Hebert, B., S. Costantino, and P.W. Wiseman, *Spatiotemporal image correlation spectroscopy (STICS) theory, verification, and application to protein velocity mapping in living CHO cells*. Biophysical Journal, 2005. **88**(5): p. 3601-3614.
176. Yam, P.T., C.A. Wilson, L. Ji, B. Hebert, E.L. Barnhart, N.A. Dye, P.W. Wiseman, G. Danuser, and J.A. Theriot, *Actin-myosin network reorganization breaks symmetry at the cell rear to spontaneously initiate polarized cell motility*. J. Cell Biol., 2007. **178**(7): p. 1207-1221.
177. Svitkina, T.M., A.B. Verkhovskiy, K.M. McQuade, and G.G. Borisy, *Analysis of the actin-myosin II system in fish epidermal keratocytes: mechanism of cell body translocation*. J Cell Biol, 1997. **139**(2): p. 397-415.
178. Verkhovskiy, A.B., T.M. Svitkina, and G.G. Borisy, *Self-polarization and directional motility of cytoplasm*. Curr. Biol., 1999. **9**(1): p. 11-20, S1.
179. Boulesteix, T., E. Beaurepaire, M.P. Sauviat, and M.C. Schanne-Klein, *Second-harmonic microscopy of unstained living cardiac myocytes: measurements of sarcomere length with 20-nm accuracy*. Opt. Lett., 2004. **29**: p. 2031--2033.

180. Plotnikov, S.V., A.C. Millard, P.J. Campagnola, and W.A. Mohler, *Characterization of the myosin-based source for second-harmonic generation from muscle sarcomeres*. *Biophys. J.*, 2006. **90**: p. 693--703.
181. Kolega, J., *Phototoxicity and photoinactivation of blebbistatin in UV and visible light*. *Biochemical and biophysical research communications*, 2004. **320**(3): p. 1020-5.
182. Ojkic, N., D. Laporte, J.-Q. Wu, and D. Vavylonis, *Model of Condensation of an Actomyosin Network into a Contractile Ring for Fission Yeast Cell Division: The Effect of Actin Cross-Linkers Alpha-Actinin and Fimbrin*. *Biophysical Journal*, 2012. **102**(3): p. 694a-695a.
183. Bendix, P.M., G.H. Koenderink, D. Cuvelier, Z. Dogic, B.N. Koeleman, W.M. Briehar, C.M. Field, L. Mahadevan, and D.A. Weitz, *A quantitative analysis of contractility in active cytoskeletal protein networks*. *Biophys J*, 2008. **94**(8): p. 3126-3136.
184. Farsiu, S., D. Robinson, M. Elad, and P. Milanfar, *Advances and challenges in super-resolution*. *International Journal of Imaging Systems and Technology*, 2004. **14**(2): p. 47-57.
185. Erdmann, T. and U.S. Schwarz, *Stochastic force generation by small ensembles of myosin II motors*. *Physical review letters*, 2012. **108**(18): p. 188101.
186. Ojkic, N., J.Q. Wu, and D. Vavylonis, *Model of myosin node aggregation into a contractile ring: the effect of local alignment*. *Journal of physics. Condensed matter : an Institute of Physics journal*, 2011. **23**(37): p. 374103.
187. McBeath, R., D.M. Pirone, C.M. Nelson, K. Bhadriraju, and C.S. Chen, *Cell shape, cytoskeletal tension, and RhoA regulate stem cell lineage commitment*. *Developmental cell*, 2004. **6**(4): p. 483-495.
188. Goffin, J.M., P. Pittet, G. Csucs, J.W. Lussi, J.-J. Meister, and B. Hinz, *Focal adhesion size controls tension-dependent recruitment of α -smooth muscle actin to stress fibers*. *The Journal of cell biology*, 2006. **172**(2): p. 259-268.
189. Ren, Y., J.C. Effer, M. Norstrom, T. Luo, R.A. Firtel, P.A. Iglesias, R.S. Rock, and D.N. Robinson, *Mechanosensing through cooperative interactions between myosin II and the actin crosslinker cortexillin I*. *Current biology : CB*, 2009. **19**(17): p. 1421-8.
190. Luo, T., K. Mohan, P.A. Iglesias, and D.N. Robinson, *Molecular mechanisms of cellular mechanosensing*. *Nature materials*, 2013. **12**(11): p. 1064-71.
191. Luo, T., K. Mohan, V. Srivastava, Y. Ren, P.A. Iglesias, and D.N. Robinson, *Understanding the cooperative interaction between myosin II and actin cross-linkers mediated by actin filaments during mechanosensation*. *Biophysical journal*, 2012. **102**(2): p. 238-247.
192. Watanabe, T., H. Hosoya, and S. Yonemura, *Regulation of myosin II dynamics by phosphorylation and dephosphorylation of its light chain in epithelial cells*. *Molecular biology of the cell*, 2007. **18**(2): p. 605-616.
193. Besser, A. and U.S. Schwarz, *Coupling biochemistry and mechanics in cell adhesion: a model for inhomogeneous stress fiber contraction*. *New Journal of Physics*, 2007. **9**(11): p. 425.
194. Seo, C.H., K. Furukawa, K. Montagne, H. Jeong, and T. Ushida, *The effect of substrate microtopography on focal adhesion maturation and actin organization via the RhoA/ROCK pathway*. *Biomaterials*, 2011. **32**(36): p. 9568-9575.
195. Rottner, K., A. Hall, and J. Small, *Interplay between Rac and Rho in the control of substrate contact dynamics*. *Current Biology*, 1999. **9**(12): p. 640-S1.
196. Katoh, K., Y. Kano, M. Amano, K. Kaibuchi, and K. Fujiwara, *Stress fiber organization regulated by MLCK and Rho-kinase in cultured human fibroblasts*. *American Journal of Physiology-Cell Physiology*, 2001. **280**(6): p. C1669-C1679.
197. Chrzanowska-Wodnicka, M. and K. Burridge, *Rho-stimulated contractility drives the formation of stress fibers and focal adhesions*. *The Journal of cell biology*, 1996. **133**(6): p. 1403-1415.
198. Amano, M., K. Chihara, K. Kimura, Y. Fukata, N. Nakamura, Y. Matsuura, and K. Kaibuchi, *Formation of actin stress fibers and focal adhesions enhanced by Rho-kinase*. *Science*, 1997. **275**(5304): p. 1308-1311.
199. Hotulainen, P. and P. Lappalainen, *Stress fibers are generated by two distinct actin assembly mechanisms in motile cells*. *The Journal of cell biology*, 2006. **173**(3): p. 383-394.
200. Hayakawa, K., N. Sato, and T. Obinata, *Dynamic reorientation of cultured cells and stress fibers under mechanical stress from periodic stretching*. *Experimental cell research*, 2001. **268**(1): p. 104-114.

201. Wang, J.H.-C., P. Goldschmidt-Clermont, J. Wille, and F.C.-P. Yin, *Specificity of endothelial cell reorientation in response to cyclic mechanical stretching*. Journal of biomechanics, 2001. **34**(12): p. 1563-1572.
202. Tanner, K., A. Boudreau, M.J. Bissell, and S. Kumar, *Dissecting regional variations in stress fiber mechanics in living cells with laser nanosurgery*. Biophysical journal, 2010. **99**(9): p. 2775-2783.
203. Sakamoto, N., N. Saito, X. Han, T. Ohashi, and M. Sato, *Effect of spatial gradient in fluid shear stress on morphological changes in endothelial cells in response to flow*. Biochemical and biophysical research communications, 2010. **395**(2): p. 264-269.

Curriculum Vitae

Wei Nie

3 DUH Drive. Apt. 136, Bethlehem, PA 18015

(610) 570-2312 | wen208@lehigh.edu

EDUCATION

Lehigh University

Bethlehem, PA

PhD in Physics

Sept 2008-May 2014

- *Dissertation: Dynamics of myosin II organization into contractile networks and fibers at the medial cell cortex*

University of York York, UK

MSc in Physics

Aug 2006 – June 2008

- *Dissertation: High-n Mode Ballooning Instabilities With Low Toroidal Flow Shear*

University of Science & Technology of China

BS in Physics

Hefei, China

Sept 1995 – June 2000

RESEARCH

Dynamics of actomyosin network assembly

Sept 2011 – April 2014

Second/third harmonic generation microscopy

May 2009 – Aug 2011

Nonlinear instabilities of plasma in Tokamak

Aug 2006 – June 2008

PUBLICATIONS

1. Wei Nie, Ming-tzo Wei, H. Daniel Ou-Yang, Sabrina Jedlicka, Dimitrios Vavylonis, "Dynamics of myosin II organization into contractile networks and fibers at the medial cell cortex". Submitted for peer view.
2. Ting Xu, Dimitrios Vavylonis, Feng Tsai, Gijsje Koenderink, Wei Nie, Eddy Yusuf, I-Ju Lee, Jian-Qiu Wu, and Xiaolei Huang, "SOAX: a software for quantification of biopolymer networks". Submitted for peer view.

3. Ming-Tzo Wei, Colleen Curly, Wei Nie, Sabrina Jedlicka, Dimitrios Vavylonis, H. Daniel Ou-Yang, “Intracellular stiffness regulated by dynamic myosin-generated stress”. Submitted for peer view.

CONFERENCE PRESENTATIONS

1. “*Dynamics of non-muscle myosin II organization into stress fibers and contractile networks*” (oral presentation, W. Nie, M.-T. Wei, H. D. Ou-Yang, S. Jedlicka, D. Vavylonis). 2014 American Physical Society March Meeting, Denver CO
2. “*Dynamics of non-muscle myosin II organization into stress fibers and contractile networks*” (poster presentation, W. Nie, M.-T. Wei, H. D. Ou-Yang, S. Jedlicka, D. Vavylonis). 2013 Biophysical Society Pennsylvania Network Meeting, Penn State, University Park PA.
3. “*Dynamics of non-muscle myosin II organization into stress fibers and contractile networks*” (poster presentation, W. Nie, M.-T. Wei, H. D. Ou-Yang, S. Jedlicka, D. Vavylonis). Force Sensing: Mechanobiology from Molecules to Tissues, Pennsylvania Muscle Institute Symposium, Philadelphia PA.
4. “*Dynamics of non-muscle myosin II organization into stress fibers and contractile networks*” (poster presentation, W. Nie, M.-T. Wei, H. D. Ou-Yang, S. Jedlicka, D. Vavylonis). 2013 Biophysical Society Annual Meeting, Philadelphia PA
5. “*Dynamics of non-muscle myosin II organization into stress fibers and contractile networks*” (poster, W. Nie, M.-T. Wei, H. D. Ou-Yang, S. Jedlicka, D. Vavylonis). 2012 American Society for Cell Biology Annual Meeting, San Francisco, CA.
6. “*Dynamics of non-muscle myosin II organization into stress fibers and contractile networks*” (poster presentation, W. Nie, M.-T. Wei, H. D. Ou-Yang, S. Jedlicka, D. Vavylonis). 2012 Biophysical Society Pennsylvania Network Meeting: Physics and Chemistry of Biological Systems. Bethlehem, PA.
7. “*Stress fiber organization and dynamics in cells adhered to substrates of varying stiffness*”, (poster presentation, W. Nie, M.-T. Wei, I. Biaggio, H. D. Ou Yang, S. Jedlicka, D. Vavylonis). 2012 Biophysical Society Annual Meeting, San Diego CA
8. “*Stress fiber organization and dynamics in cells adhered to substrates of varying stiffness*” (poster presentation, W. Nie, M.-T. Wei, D. Ou Yang, S. Jedlicka, D. Vavylonis). 2011 Lehigh University COT Open House, Bethlehem PA.

MISCELLANEOUS

Languages: Mandarin , English

Programing/Computer: Java, C, Fortran, MATLAB